Finding And Exploiting Structure In Complex Systems Via Geometric And Statistical Methods

Piyush Grover

Dissertation submitted to the Faculty of the
Virginia Polytechnic Institute and State University
in partial fulfillment of the requirements for the degree of

Doctor of Philosophy
in
Engineering Mechanics

Shane D. Ross, Chair
Mark A. Stremler
Ronald D. Kriz
Craig A. Woolsey
Harry Dankowicz

June 1st, 2010
Blacksburg, Virginia

Keywords: Set oriented approach, Almost invariant sets, Restricted three body problem, Fluid mixing, Braids

Finding and exploiting structure in complex systems via geometric and statistical methods

Piyush Grover

Abstract

The dynamics of a complex system can be understood by analyzing the phase space structure of that system. We apply geometric and statistical techniques to two Hamiltonian systems to find and exploit structure in the phase space that helps us get qualitative and quantitative results about the phase space transport. While the structure can be revealed by the study of invariant manifolds of fixed points and periodic orbits in the first system, there do not exist any fixed points (and hence invariant manifolds) in the second system. The use of statistical (or measure theoretic) and topological methods reveals the phase space structure even in the absence of fixed points or stable and unstable invariant manifolds.

The first problem we study is the four-body problem in the context of a spacecraft in the presence of a planet and two of its moons, where we exploit the phase space structure of the problem to devise an intelligent control strategy to achieve mission objectives. We use a family of analytically derived controlled Keplerian Maps in the Patched-Three-Body framework to design fuel efficient trajectories with realistic flight times. These maps approximate the dynamics of the Planar Circular Restricted Three Body Problem (PCR3BP) and we patch solutions in two different PCR3BPs to form the desired trajectories in the four body system.

The second problem we study concerns phase space mixing in a two-dimensional time dependent Stokes flow system. Topological analysis of the braiding of periodic points has been recently used to find lower bounds on the complexity of the flow via the Thurston-Nielsen classification theorem (TNCT). We extend this framework by demonstrating that in a perturbed system with no apparent periodic points, the almost-invariant sets computed using a transfer operator approach are the natural objects on which to pin the TNCT.

Dedication

If I have seen a little further it is by standing on the shoulders of Giants : Isaac Newton

This thesis is dedicated to all the researchers in science and engineering whose work has inspired me and enabled me to find the joy of research. For this, I will forever be indebted.

Acknowledgments

I owe my deepest gratitude to my advisor Dr. Shane Ross, who has helped me in various ways to think like a dynamicist. His dedication to research and commitment to excellence has been a constant source of inspiration for me. I would like to thank him for his support during my graduate studies, and the various growth opportunities he has provided to me.

I would like to thank Dr. Mark Stremler for giving me an opportunity to work on the fluid mixing problem, resulting in a fruitful collaboration between the two research groups. His enthusiasm for research has been very motivating for me.

My special thanks go to Dr. Harry Dankowicz for asking the tough questions and as a result making this thesis better. I would also like to thank my committee members Dr. Craig Woolsey and Dr. Ronald Kriz.

I wish to thank all the wonderful teachers who have taught me over the years: during high school (especially Arvind Chauhan), during undergraduate studies at IIT (especially Dr. Naresh Chandiramani, and Dr. Uday Dixit) and graduate studies here at Virginia Tech (especially Dr. James Thomson, Dr. Martin Klaus, Dr. Scott Hendricks, Dr. George Hagedorn and Dr. Martin Day).

I have had many wonderful discussions on dynamics and life, with my colleague and friend Phanindra Tallapragada, for which I would like to thank him. I would also like to thank the ESM graduate students group, especially Carmine Senatore, Giancarlo Bordonaro, Mohsen Gheisarieha, Pankaj Kumar and Giovanni Sansavini for being helpful and fun colleagues. Special thanks are also extended to friends for life from the carefree IIT days, Praveen Sharma, Vishesh Vikas, Rahul Jain and Pranshu Chugh.

My parents Rakesh and Renu Grover, though several thousand miles away, have been an unwavering source of love and support during these five years, along with my loving sister Dimple. My family has been my ultimate support group, and I cannot than them enough.

Finally, my thanks to Lindsey Brunswick for being an important part of my *joie de vivre.*

Contents

List of Figures

List of Tables

Chapter 1

Introduction

The analysis of chaotic nonlinear dynamical systems has attracted the interest of scholars from a wide variety of mathematical fields. From pure mathematicians working in ergodic theory, to physicists analyzing plasma dynamics, to mechanical engineers trying to suppress flutter in vibrating machinery, this field has generated a lot of activity in past several decades. One of the first lessons learned in the study of such systems has been that simply generating long individual trajectories via computer simulations usually results in very limited understanding of the dynamics. As a result, techniques that focus on identifying and exploiting the underlying structure of these dynamical systems (defined by ODEs, PDEs, discrete maps or data-sets) have proved invaluable in this cause. This dissertation describes the application of such techniques to the study of two complex systems and also reports some numerical results that combine the topological and statistical techniques in a novel way.

In this dissertation, we focus on applying geometric and statistical techniques to find and exploit structure in phase space that helps us get qualitative and quantitative results about the transport between different regions of interest in phase space. While the structure can be revealed by the study of invariant manifolds of fixed points or periodic orbits in some systems, there are many complex systems where there do not exist any fixed points (and hence invariant manifolds). The use of statistical (or measure theoretic) and topological

methods can reveal phase space structure even in the absence of fixed points or stable and unstable invariant manifolds.

The first system [2] that we study is the four-body problem in the context of a spacecraft in the presence of a planet and two of its moons, where we exploit the phase space structure of the problem to devise an intelligent control strategy to achieve control objectives. This problem can be broken into 2 three-body problems under suitable assumptions and analyzed in the framework of the Planar Circular Restricted Three Body Problem (PCR3BP). The PCR3BP, which is a special case of the classical three body problem, is treated as a perturbation of the 2-body problem, and we use an averaged analytical approximation of the natural dynamics of the PCR3BP (in the form of a two-dimensional Poincaré map) as a starting point for our analysis. This Poincaré map reveals the structure of the problem, and phase space transport in this system can be analyzed by studying the fixed points, and their invariant manifolds. We modify this map to add control and use the new controlled map to achieve fuel efficient trajectories with realistic times-of-flight.

The second problem [3] we study concerns phase space mixing using the lid-driven wide-cavity Stokes flow system as our testbed. The phase space structure consisting of fixed points and elliptical islands has been recently used to find lower bounds on complexity of the flow of this system. Small perturbations in certain design parameters of this system can lead to loss of fixed points of low period, and an apparent loss of structure. We use the method of almost-invariant sets to demonstrate that the underlying phase space structure is still preserved in some statistical sense, even under appreciable change in parameter values. Using this approach, an analysis of complexity via topological methods that give a lower bound on the topological entropy (via use of the Thurston-Nielsen classification theorem) can still be carried out in an analogous manner.

The dissertation is arranged as follows. Chapter 2 reviews the mathematical techniques used and referred to throughout this document and lists relevant literature sources. Chapter 3 deals with the trajectory design problem in the four-body planet-moon environment. In

Chapter 4, we study phase space mixing and transport by combining statistical and topological approaches. Finally, in chapter 5, we make some concluding remarks.

Chapter 2

Background On Mathematical Techniques

This chapter reviews the mathematical concepts and ideas that will be used and referred to throughout this dissertation. The following sections describe the three varying approaches to analyzing dynamical systems, i.e.,
(i) *Geometric approach*: The study of geometric objects like fixed points, periodic orbits and their stable and unstable manifolds,
(ii) *Statistical approach*: The study of statistical (or measure theoretic) quantities like invariant measures, time and space averages, and almost invariant sets.
(iii) *Topological approach*: The study of topological properties like topological entropy and mixing.

We make connections between these approaches at appropriate places throughout the dissertation.

2.1 Geometric approach

In this section, we review the properties of a class of dynamical systems that we analyze in later chapters. Since both the systems we consider in this dissertation can be (and are) studied by construction of two-dimensional area preserving maps, we will focus our attention on that class of systems.

Poincaré was the first to analyze the global dynamics of a system of differential equations by studying an associated discrete time system (or a map), and he used this technique to study the three body problem. Poincaré maps can arise naturally in a number of ways in dynamical systems; the following two cases are especially relevant to our discussion in later chapters [4].

a) **In the study of orbit structure near a periodic orbit of a system of autonomous ordinary differential equations**

Consider the following continuous-time dynamical system, described by autonomous ordinary differential equations,

$$\dot{x} = f(x),\ x \in \Re^n, \tag{2.1}$$

where $f : U \to \Re^n$ is C^r on some open set $U \in \Re^n$. Let γ be a periodic orbit (with period T) of the flow ϕ_t generated by the above system in $\Re^n$. Let $x_0 \in \Re^n$ be any point on the orbit γ, and $\sum$ be a $n-1$ dimensional cross-section transverse to γ at x_0. Given the smoothness assumptions on f, we can find an open set $V \subset \Sigma$ such that trajectories starting in V return to Σ in a time close to T. The map that takes points in V back to Σ is the associated Poincaré map, denoted by P, i.e.,

$$\begin{aligned} P &: V \to \Sigma \\ x &\to \phi_{\tau(x)}(x), \end{aligned} \tag{2.2}$$

where $\tau(x)$ is the time of flight of the point x to Σ. Note that by definition, $\tau(x_0) = T$, and $P(x_0) = x_0$. This means that x_0 is a fixed point of the map P. Therefore, a fixed point of

the map P corresponds to a periodic orbit of the dynamical system described in equation (2.1). The stability of x_0 for P reflects the stability of γ for the flow ϕ_t, i.e., the periodic orbit γ of the continuous dynamical system is stable if and only if the fixed point x_0 of the discrete dynamical system is stable. This result can be derived by the use of the theory of Floquet multipliers, which states the following:

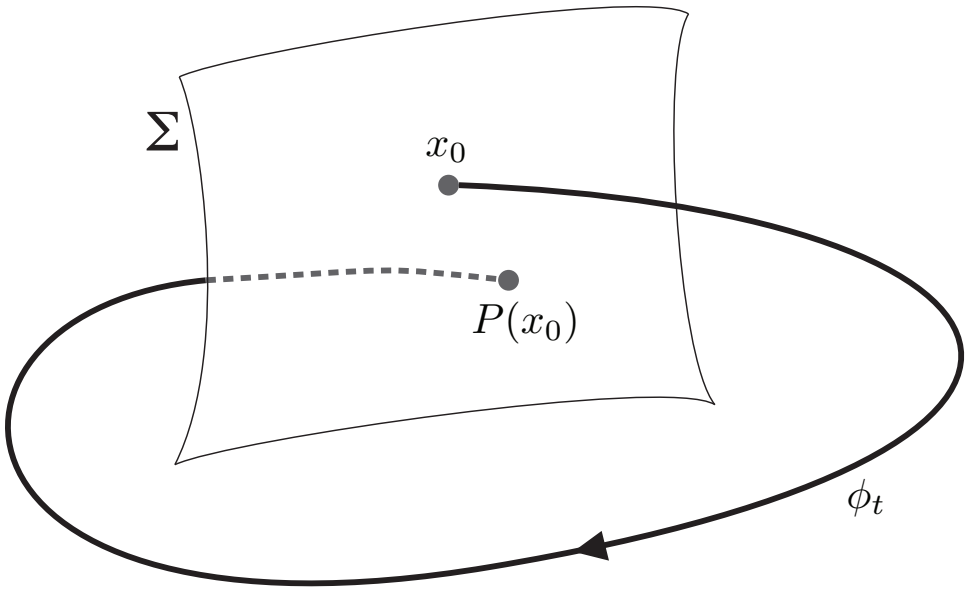

Figure 2.1: This illustration shows a Poincaré surface of section Σ of the flow map ϕ. The point $x_0 \in \Sigma$ is mapped by Poincaré map back to Σ at $P(x_0)$.

Theorem 1. *(Floquet Theorem) Let ξ be a fundamental matrix solution of the periodic system $\dot{x} = A(t)x$, where $A(t)$ a periodic function with period T. Then, for all $t \in \Re$,*
$\xi(t+T) = \xi(t)\xi^{-1}(0)\xi(T)$. In addition, for each matrix B (possibly complex) such that $e^{TB} = \xi^{-1}(0)\xi(T)$, there is a periodic (with period T) function $R(t)$ such that
$\xi(t) = R(t)e^{tB}$ for all t.

This theorem can be applied to our system by linearizing it around the periodic orbit γ, i.e put $A(t) = Df(\gamma(t))$. Then, it follows that the behavior of solutions in the neighborhood of γ is determined by the eigenvalues of the constant matrix e^{BT}. These eigenvalues $\lambda_1, ..., \lambda_n$, (where $\lambda_n = 1$) are called Floquet multipliers. It also turns out that the eigen-

values λ_1 through λ_{n-1} are also the eigenvalues of the Jacobian of the Poincaré map P. The correspondence between stability of fixed points of P and periodic orbits of f follows immediately.

Definition 1. *The local stable manifold W^s_{loc} of a fixed point x_0 of any map P can be defined as,*

$$W^s_{loc}(x_0) = \{x \in U | P^j(x) \in U \ \forall j \in \mathbf{N} \ and \ \lim_{j\to\infty} P^j(x) \to x_0\} \tag{2.3}$$

where U is a neighborhood of the fixed point x_0. Similarly, the local unstable manifold W^u_{loc} is defined as,

$$W^u_{loc}(x_0) = \{x \in U | P^{-j}(x) \in U \ \forall j \in \mathbf{N} \ and \ \lim_{j\to\infty} P^{-j}(x) \to x_0\} \tag{2.4}$$

Consider a vector field f in $\Re^3$, generating a flow given by $\phi_t(x)$, $x \in \Re^3$. Assume as before that γ is a periodic solution with period T, and construct the Poincaré map P as before. Additionally assume that the fixed point x_0 of map P is of saddle type, i.e., it has a one-dimensional stable manifold $W^s(x_0)$ and a one-dimensional unstable manifold $W^u(x_0)$ lying in Σ. These manifolds can be related to the stable and unstable manifolds of the periodic orbit γ by treating them as initial conditions, and doing a numerical continuation as follows:

$$W^s(\gamma) = \cup_{t\le 0}\phi_t(W^s_{loc}(x_0)) \tag{2.5}$$

$$W^u(\gamma) = \cup_{t\ge 0}\phi_t(W^u_{loc}(x_0)) \tag{2.6}$$

Hence, in $\Re^3$, $W^s(\gamma)$ and $W^u(\gamma)$ are two-dimensional surfaces.

b) **In the study of global solutions of a non-autonomous system of ordinary differential equations with periodic time dependence**

Consider the following system,

$$\dot{x} = f(x,t), \qquad (x,t) \in \Re^n \times \Re, \tag{2.7}$$

where $f(\cdot,t) = f(\cdot,t+T)$ is periodic in t with time period $T = 2\pi/\omega$. The above system can be written in an expanded phase space, by defining $\theta = \omega t + \alpha$ as a state variable, where α

is the chosen value of θ at time $t = 0$. Thus the new system becomes,

$$\dot{x} = f(x, \theta), \tag{2.8}$$

$$\dot{\theta} = \omega, \tag{2.9}$$

where $(x, \theta) \in \Re^n \times S^1$, and the flow map is now given by $\phi_t = (x(t), \theta(t) = \omega t + \alpha (\mathrm{mod} 2\pi))$. In this case, a **global** Poincaré section can be defined, since all the solutions of the original system will be transversal to the following section,

$$\Sigma^{\theta_0} = \{(x, \theta) \in \Re^n \times S^1 | \theta = \theta_0 \in (0, 2\pi]\} \tag{2.10}$$

The resulting Poincaré map can be written as:

$$P_{\theta_0} : \Sigma^{\theta_0} \to \Sigma^{\theta_0}, \tag{2.11}$$

$$x\Big(\frac{\theta_0 - \alpha}{\omega}\Big) \to x\Big(\frac{\theta_0 - \alpha + 2\pi}{\omega}\Big) \tag{2.12}$$

2.1.1 Generic properties of two-dimensional symplectic maps

Earlier in this section we discussed how discrete time maps in two-dimensions can be obtained. We briefly discuss some features of a two-dimensional area-preserving map that are generic in nature, i.e., they are expected to be present in all such maps irrespective of the system the map is derived from [5]. We consider the standard map, which has been widely studied in the literature for demonstrating the generic properties of maps derived from Hamiltonian systems. The map $T : S^1 \times S^1 \to S^1 \times S^1$ is given by,

$$T(\theta_n, p_n) = (\theta_n + p_{n+1}, p_n + K \sin(\theta_n)), \tag{2.13}$$

where both θ and p are taken modulo 2π. Here the phase space variable p is called the *action* of the system, and θ is called the *angle*. The rotational invariant curves are the curves that preserve an integral of the motion, wind around the angle coordinate and are homoemorphic to $p = 0$, where as the librational invariant curves, while preserving an integral of the motion, do not completely encircle the angle coordinate.

The phase space of this map varies greatly with variation in the parameter K and this variation is shown in figure 2.2. The map is integrable for $K = 0$, i.e., the phase space is fully foliated by *rotational* invariant curves (which are straight lines in this case) and there is no *irregular* or *chaotic* motion. For a slightly higher value of $K = 0.2$, most of the structure is still preserved, and most of the *rotational* invariant curves are intact. But there are orbits that no longer lie on these invariant curves. A family of curves is observed, the so called *librational* curves which are different in nature than the rotational invariant curves, resulting in chains of alternating saddle and elliptical periodic points, and separated from invariant curves by a separatrix. Such a region is called a resonance region, and is identified by its resonance , generally expressed as a ratio $m : n$. An $(m : n)$ resonance will have n elliptical islands, consisting on n elliptical fixed points and n saddles. Iterating any of those fixed points n times will lead to winding around m times around in the angle coordinate. As we increase the value of K to 0.5, we observe that more such resonances show up, and also observe that there has been a break up of the separatrix observed earlier. This break-up

is a manifestation of transverse intersections of stable and unstable manifolds of the saddle points in the resonance zone, and the presence of such an intersection means the map is chaotic in the neighborhood of such a region. Increasing the value K to 0.95, we see what is termed in the literature a "mixed" phase space i.e., a significant area in the phase space is filled by the chaotic sea, and there are resonances of high periods. For $K = 5$, no rotational invariant curves remain, and most of the phase space is chaotic.

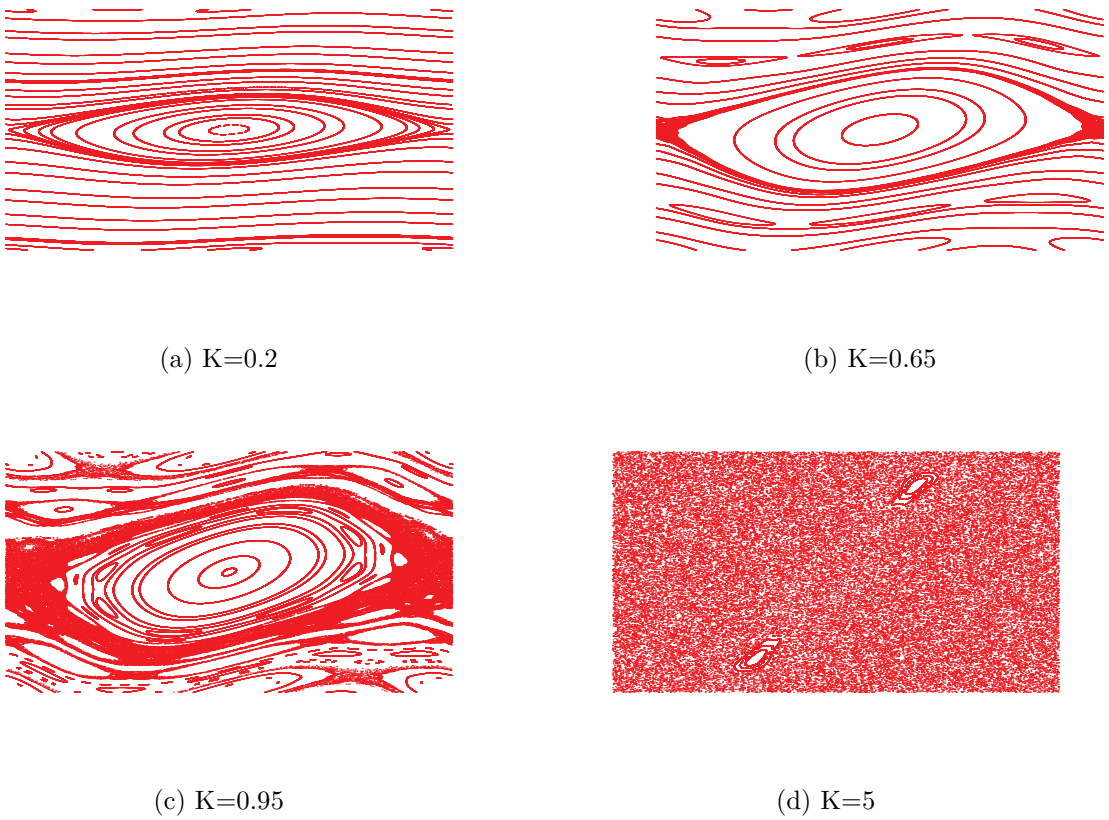

(a) K=0.2

(b) K=0.65

(c) K=0.95

(d) K=5

Figure 2.2: Phase space of the standard map for different K values. Note the gradual break up of invariant circles, and increase in the area of the chaotic zone.

2.1.2 Transport in two-dimensional maps: lobe dynamics

So far, in this section we have seen how to obtain two-dimensional maps from continuous time systems, and have also reviewed some of the generic properties of such maps. We briefly review an important technique [6] that can be used to study transport in such maps. We will restrict our attention to area-preserving diffeomorphisms,

$$f : M \to M, \tag{2.14}$$

where M is a differentiable , orientable two-dimensional manifold. Let $p_i, i = 1, 2, ..., N$ denote a collection of saddle-type hyperbolic periodic points for f. We can assume they are all fixed points by replacing f with a higher iterate of f for which each of them is a fixed point. The one dimensional stable and unstable manifolds of p_i are denoted by $W^s(p_i)$ and $W^u(p_i)$.

Definition 2. *Suppose $q \in W^s(p_i) \cap W^u(p_j)$, and let $S[p_i, q]$ denote the segment of $W^s(p_i)$ with endpoints p_i and q, and $U[p_j, q]$ denote the segment of $W^u(p_j)$ with endpoints p_j and q. The q is called the primary intersection point (or pip) if $S[p_i, q) \cap U[p_j, q] = \{q\}$.*

Definition 3. *Let $q_0, q_1 \in W^u(p_j) \cap W^s(p_i)$ be two adjacent pips, i.e., no other pips exist on $U[q_0, q_1]$ and $S[q_0, q_1]$. Then the region bounded by $U[q_0, q_1] \cap S[q_0, q_1]$ is referred to as a lobe.*

Suppose $W^s(p_i)$ and $W^u(p_j)$ intersect in the pip q. Then the boundary B is defined as $S[p_i, q] \cup U[p_j, q]$, and the transport across this boundary is mediated solely by the lobes. Define the regions R_1 and R_2 as shown in figure 2.4. Define the regions $L_{1,2}(1)$ and $L_{2,1}(1)$ as shown in figure 2.5. Then the following lemma applies:

Lemma 1. *Under one iteration of f, the only points that can move from R_1 to R_2 by crossing B are those in the lobe $L_{1,2}(1)$. Similarly, under one iteration of f, the only points that can move from R_2 to R_1 by crossing B are those in the lobe $L_{2,1}(1)$. Hence the local flux across B can be calculated by studying the dynamics of these lobes.*

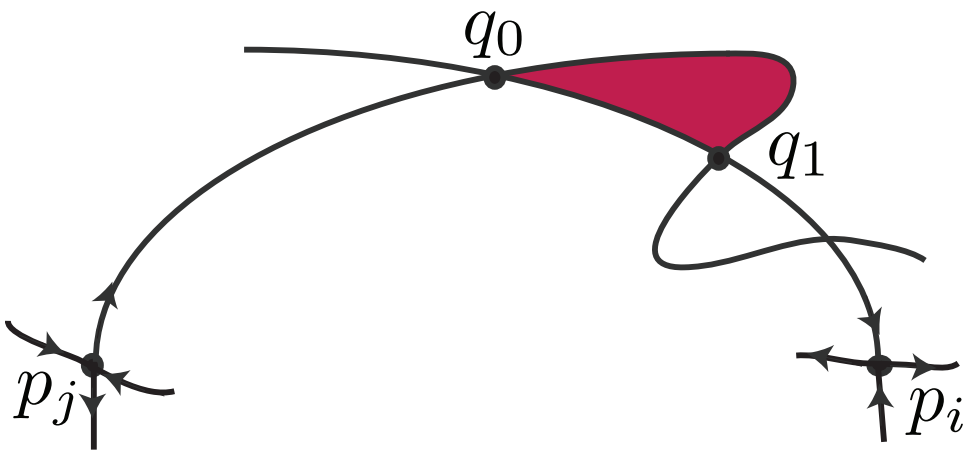

Figure 2.3: This illustration shows two pips, q_0 and q_1, and the colored region is the lobe bounded by $U[q_0, q_1] \cap S[q_0, q_1]$.

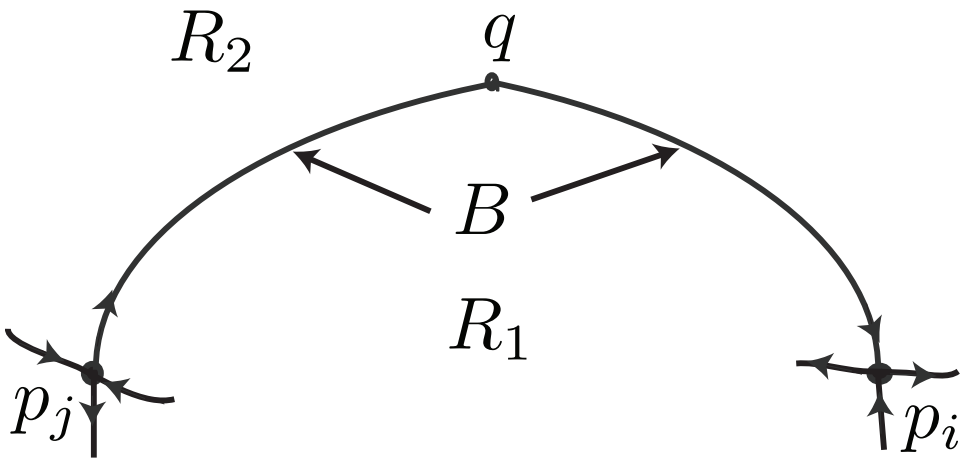

Figure 2.4: This figure illustrates the two regions R_1 and R_2, and the boundary **B** between them. Transport across this boundary is mediated by lobes.

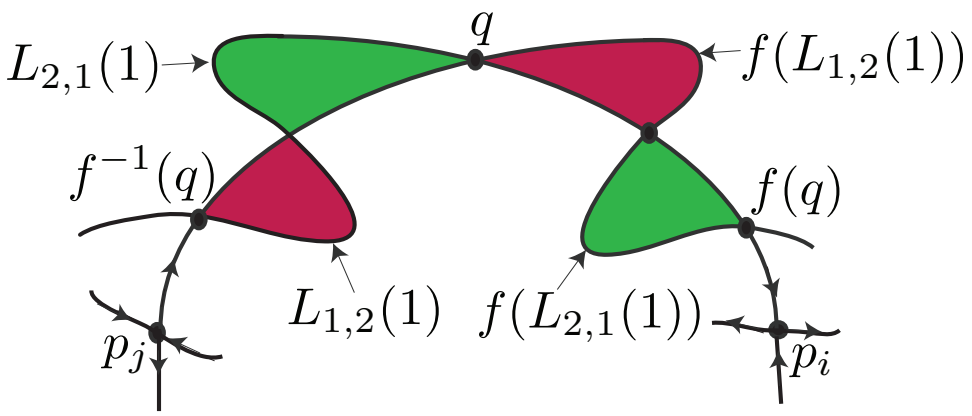

Figure 2.5: This illustration shows the transport across boundary defined earlier. The phase space volume $L_{1,2}(1)$ in maroon will be mapped from inside to outside of boundary to $f(L_{1,2}(1))$ in maroon in one iteration of the map, while the region in green $L_{2,1}(1)$ is mapped from outside to inside in one iteration.

To study the transport mediated by lobes, we divide the region of interest into regions $R_i, i = 1, ..., N_R$. To keep track of how the mixing across various regions is taking place, we assume each region R_i is filled with a species S_i at time $t = 0$. The two quantites of interest are:

1) $a_{i,j}(n)$: The flux of species S_i into region R_j on the nth iterate.

2) $T_{i,j}(n)$: The total amount of species S_i contained in region R_j immediately after the nth iterate.

Denote by $L_{i,j}(m)$ the lobe that leaves R_i and enters R_j on the mth iterate. Also denote by $L^k_{i,j}(m)$ the portion of the lobe $L_{i,j}(m)$ that is occupied by species S_k. Denote by m the Lebesgue measure. Then the following theorems holds:

Theorem 2. $a_{i,j}(n) = T_{i,j}(n) - T_{i,j}(n-1) = \sum_{k=1}^{N_R} [m(L^i_{k,j}(n)) - m(L^i_{j,k}(n))]$

This result expresses the flux of species S_i into region R_j on the nth iterate in terms of parts of lobes of entering and leaving the region R_j on the nth iterate that contain species S_i. This theorem can be derived by noting that since f is area-preserving, $a_{i,j}(n) = T_{i,j}(n) - T_{i,j}(n-1)$. The detailed proof is given in [6].

Theorem 3. $m(L^i_{k,j}(n)) = \sum_{s=1}^{N_R} \sum_{m=1}^{n} m(L_{k,j}(n) \cap L_{s,i}(m)) - \sum_{s=1}^{N_R} \sum_{m=1}^{n-1} m(L_{k,j}(n) \cap L_{s,i}(m))$

This result expresses the amount of species S_i in lobe $L_{k,j}(n)$ in terms of lobe intersections. The detailed proof is given in the appendix of [6].

2.2 Set oriented methods: Statistical approach to dynamical systems

In this section, we give a review of a class of techniques that exploit the statistical properties of discrete-time dynamical systems, and enable us to numerically compute various mathematical objects that quantify transport in a system by delineating statistically important sets in the phase space. At the heart of this analysis lies the fact that under certain conditions, nonlinear dynamical systems can be treated as Markov chains on a (large but finite dimensional) state space. Instead of studying the time evolution of points in the original phase space, we study how various probability measures propagate under the application of the dynamics of the system. The propagator in this case is called the **Perron-Frobenius operator** P [7] (not to be confused with the Poincare map in previous section) of the underlying dynamical system.

The computations are based on an appropriate discretization of the P. The two major ideas that enable such a discretization are : the classical convergence results for finite dimensional approximations of compact operators and the results from ergodic theory, specifically the approximation of physical measures (or SRB measures [8] in some special cases) by invariant measures of stochastically perturbed systems. In contrast to other numerical techniques, these methods do not rely on computation of single long term trajectories but rather use the information from many short term trajectories. An appropriately discretized operator contains all the important information about the dynamical system, and the various eigenvectors and eigenvalues of such a linear operator give an insight into transport in phase space at various levels of detail.

We refer the reader to [9],[10],[7] and [11] for a more detailed treatment of the subject.

2.2.1 Important concepts and definitions

Consider a discrete dynamical system (or a Poincaré map constructed on a continuous dynamical system):

$$x_{j+1} = f(x_j),\ j = 0, 1, 2, ... \tag{2.15}$$

where $f : X \to X$ is a now refers to a diffeomorphism on a compact subset $X \subset \Re^n$. Let $\mathbf{B}$ be the Borel σ-algebra on X, and denote by m the Lebesgue measure on $\mathbf{B}$.

Definition 4. *A subset $A \subset X$ is called invariant if $f(A) \subseteq A$.*

We note the fact that any discretization of the dynamical system over its phase space introduces artificial noise, i.e. coarse-graining of the dynamics occurs in the process. Hence, it is helpful to state some of the concepts in the context of noisy dynamical systems, since the theory was developed in literature in that context [10]. We will give the expressions for important quantities for the deterministic case along the way for the sake of clarity. We assume the noise-less system is given by the mapping f as defined above.

Let $p(x, \cdot)$ denote the stochastic transition function associated with the dynamical system of interest, i.e., $p(x, A)$ is the probability that the first iterate of $x \in X$ lies in the set $A \subset X$. Note that for the deterministic case, $p(x, \cdot) = \delta_{f(x)}$. We assume that for every $x \in X$, the probability measure $p(x, \cdot)$ is absolutely continuous with respect to the Lebesgue measure m. Hence, we can write

$$p(x, A) = \int_A k(x, y) dm(y) \tag{2.16}$$

for all $A \subset \mathbf{B}$, with an appropriate transition density function $k : X \times X \to \mathbf{R}$. Clearly, we see that the following relation holds:

$$\int_X k(x, y) dm(y) = p(x, X) = 1 \tag{2.17}$$

for all $x \in X$.

We describe how we model the small random perturbations and hence, the stochastic transition function p. Let B denote the open unit ball in $\Re^n$ and χ_B the characteristic function of B, i.e.,

$$\chi_B(x) = \begin{cases} 1 \text{ if } ||x|| \leq 1 \\ 0 \text{ otherwise.} \end{cases} \tag{2.18}$$

For $\epsilon > 0, x, y \in X$, we set

$$k_\epsilon(x, y) = \frac{1}{\epsilon^n m(B)} \chi_B \left(\frac{1}{\epsilon}(y - x) \right) \tag{2.19}$$

The above function evaluates to zero if the points x and y are more than distance ϵ apart from each other. Hence our original transition density function can be replaced by $k_\epsilon(f(x), y)$. Also, the stochastic transition p_ϵ can be defined as

$$p_\epsilon(x, A) = \int_A k_\epsilon(f(x), y) dm(y) \tag{2.20}$$

Definition 5. *The Perron-Frobenius operator P on any measure ν is defined as*

$$P\nu(A) = \int p(x, A) d\mu(x) \tag{2.21}$$

In the deterministic case, this reduces to

$$P\nu(A) = \nu(f^{-1}(A)), \tag{2.22}$$

where f describes the deterministic dynamical system defined in equation (2.15).

Definition 6. *A measure μ is said to be invariant under the evolution of system defined by stochastic transition function p if it satisfies*

$$\mu(A) = \int p(x, A) d\nu(x), \tag{2.23}$$

for all $A \in \boldsymbol{B}$.

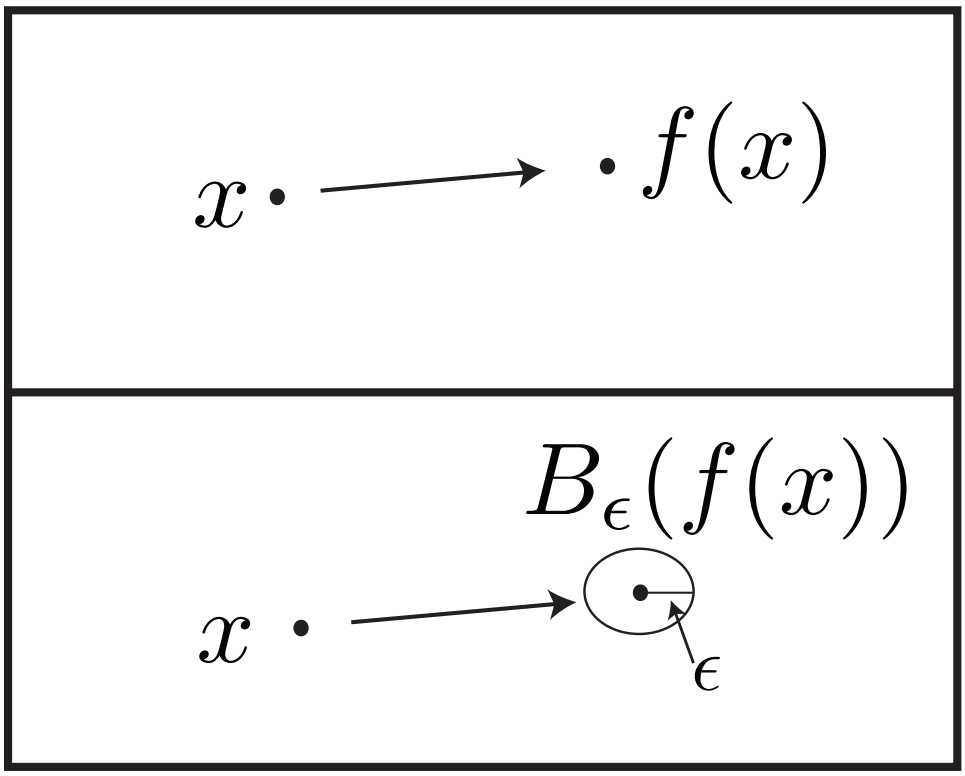

Figure 2.6: Modeling of small random perturbations: The top figure shows the noiseless case, while the bottom figure illustrates how small random perturbations are modeled.

Note that the above two definitions imply that if μ is an invariant measure of the system, then it satisfies the following equation:

$$\mu(A) = \int p(x, A) d\mu(x) = P\mu(A), \tag{2.24}$$

for all $A \in \mathbf{B}$. This implies that any invariant measure of the system will be an eigenfunction of the Perron-Frobenius operator P with eigenvalue 1.

Definition 7. *An invariant measure μ is an SRB measure if there exists a subset $U \subset X$ with $m(U) > 0$ and such that for each continuous function ψ*

$$\lim_{n\to\infty} \frac{1}{n} \sum_{i=0}^{n-1} \psi(f^i(x)) = \int \psi d\mu, \tag{2.25}$$

for all $x \in U$.

The above relation always holds for almost all x which belong to sets having a non-zero μ measure, by the Birkhoff Ergodic Theorem. The crucial difference in case the measure μ is a SRB measure is that temporal average equals the spatial average for a set of initial conditions that have positive Lebesgue measure m, i.e., it holds for some open set in the phase space X, and hence is a more physically relevant measure, since the support of measure μ in X could have Lebesgue measure $m = 0$. For this reason, SRB measures are also called natural measures or physical measures.

2.2.2 Discretization of PF-operator

To numerically compute the PF-operator P, we need to discretize it over the section of phase space of interest [10]. We discretize the domain X by a collection of small boxes, i.e $X \subset (B_1 \cup B_2 \cup ... \cup B_n)$. The covering process can be efficiently implemented by use of multilevel methods [10].

We then discretize the Perron-Frobenius operator by creating a n-state Markov chain, where each box $B \in (B_1, B_2, ..)$ corresponds to a state in the chain. For a deterministic system,

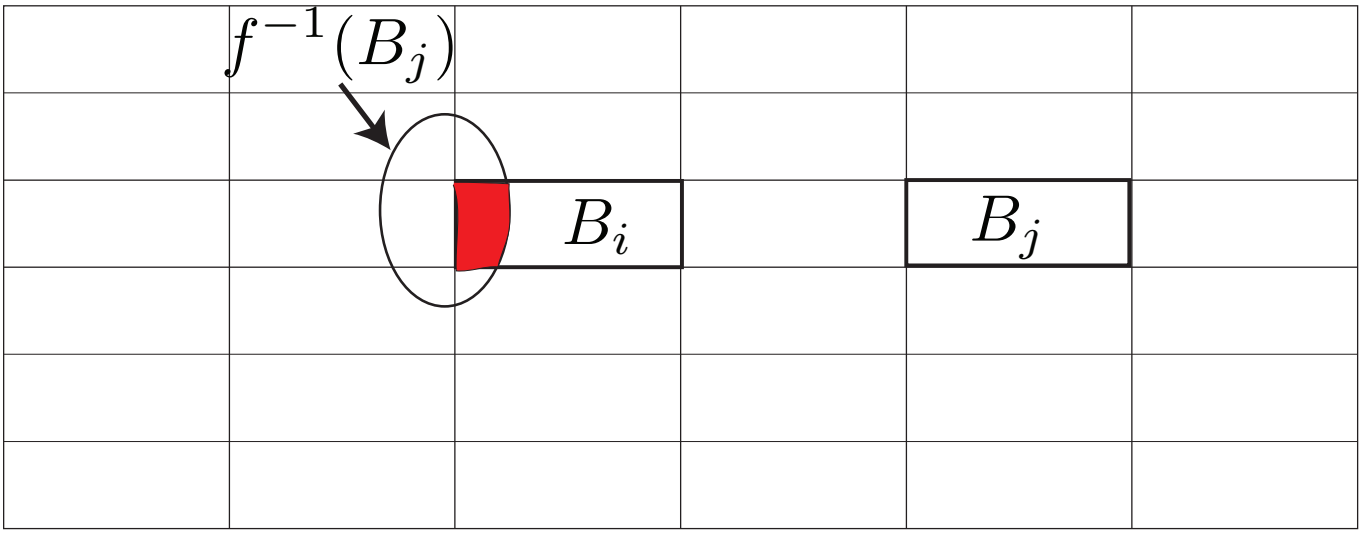

Figure 2.7: Discretization of domain into boxes. This region in red is $B_i \cap f^{-1}(B_j)$

the stochastic matrix $P = (P_{ij})$ of the Markov chain is

$$P_{ij} = \frac{m(B_i \cap f^{-1}(B_j))}{m(B_i)} \tag{2.26}$$

The (i, j)th entry of P is the probability that a randomly chosen point in B_i will be mapped into B_j over one iteration. So the dynamics of Markov chain consist of the dynamics of the map f plus some noise due to discretization. For the computation of the P_{ij}, the Monte-Carlo approach or a uniform grid over the boxes is generally used [11].

The first left eigenvector p of the matrix P provides an estimate of the physical-invariant measure of the system, $\mu(B_i) = p_i$, discretized over the phase space. This measure can be extended over any Borel-set $A \in X$ by

$$\mu(A) = \sum_{i=1}^{n} \frac{m(A \cap B_i)}{m(B_i)} p_i$$

For the rest of the chapter, we use μ to denote the invariant measure of the system under consideration, which will be in general different from the Lebesgue measure m.

2.2.3 Almost-invariant-sets

Let $p(A_1, A_2)$ be defined as the transition probability of mapping from set A_1 into A_2 under the action of stochastic transition function p, as follows

$$p(A_1, A_2) = \frac{1}{\mu(A_1)} \int_{A_1} p(x, A_2) d\mu(x) \tag{2.27}$$

Denote by $\rho_\mu(A)$, the quantity $p(A, A)$. This is the fraction of phase space volume of set A that maps back to the set over one iteration of the map.

Definition 8. *A set $A \subset X$ is said to be almost invariant if*

$$\rho_\mu(A) = \frac{\mu(A \cap f^{-1}(A))}{\mu(A)} \approx 1, \tag{2.28}$$

i.e., the points in the set map back to the same set over one iteration of the map with high probability, with the measure being the invariant measure μ.

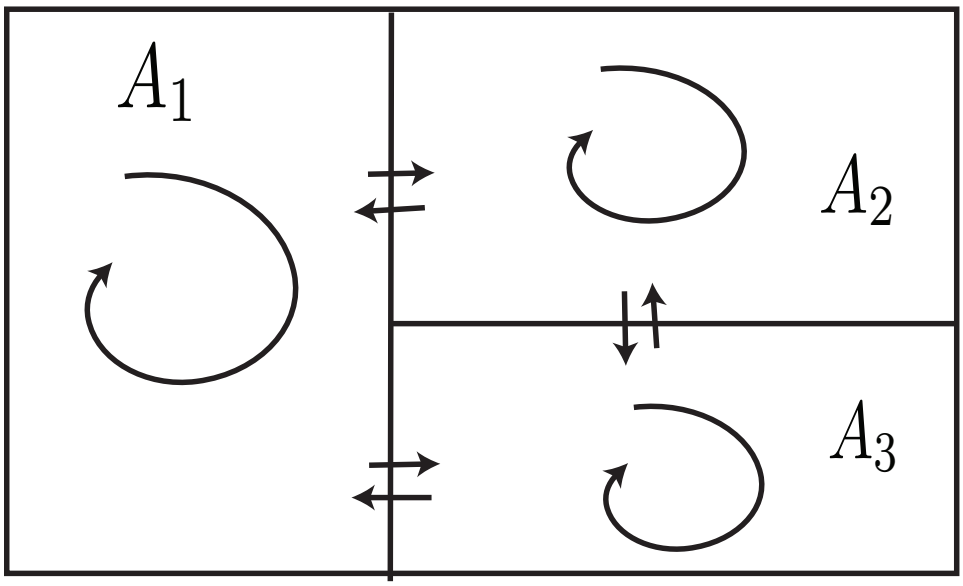

Figure 2.8: Partition into three almost invariant sets. The size of arrows signifies amount of transport. The inter-set transport is minimized while the intra-set transport dominates.

We define the problem of finding structure and macro-scale dynamics of the given system as follows [11].

Problem statement: We want to form a partition of the phase space X into a given number (say k) of sets $(A_1, A_2, ...A_k)$ such that the phase space transport between these sets is very unlikely. We also want these sets to be important statistically with respect to the long term dynamics of the system. This can be formulated mathematically as follows: We want to maximize the quantity $\sum_{i=1}^{k} \rho_\mu(A_i)$, with the constraint that $\mu(A_i)$ is not too small compared to 1. Without loss of generality, we can restrict to only partitions $(A_1, A_2, ...A_k)$ such that each member A_j of such a partition is a union of some sets in $(B_1, B_2, ...)$, i.e each $A_j = \cup_{i \in I} B_i$, for some set of box indices $I \in \{1, 2, ..., n\}$.

We can express the quantity $\rho_\mu(A)$ solely in terms of the entries of the Markov matrix P, and its first left eigenvector p as defined above. Physically, $\rho_\mu(A)$ represents the fraction of phase space volume within set A mapping back to itself, weighted with the invariant measure of the matrix. Since the set $A = \cup_{i \in I} B_i$, it is easily seen that

$$\rho_\mu(A) = \frac{\sum_{i \in I} \sum_{j \in I} \mu(f^{-1}(B_j) \cap B_i)}{\sum_{i \in I} \mu(B_i)} \tag{2.29}$$

Using the expressions for p_i, and P_{ij}, we see that

$$\rho_\mu(A) = \frac{\sum_{i,j \in I} p_i P_{ij}}{\sum_{i \in I} p_i} \tag{2.30}$$

So we want to maximize the quantity $\rho_\mu = \sum_{i=1}^{k} \rho_\mu(A_i)$ while ensuring that each of $\mu(A_i) > s$, where s is the minimum permissible measure of any set in the partition and $0 < s < 1/k$. We make an observation that in general the Markov chain given by operator P is *not* reversible, i.e., in general $p_i P_{ij} \neq p_j P_{ji}$. To use certain theorems from the theory of Markov chains, we need to form a reversible matrix, that will have a real eigen-spectrum. So we form a reversible matrix

$$R = (P + \widehat{P})/2, \tag{2.31}$$

where $\widehat{P}$ is the time-reversed analogue of P with its elements are given by

$$\widehat{P}_{ij} = \frac{p_j P_{ji}}{p_i} \tag{2.32}$$

We note the fact that the first eigenvector of R is still p, and also that the quantity ρ_μ to be maximized remains unchanged if we replace P_{ij} by R_{ij} in the expression. We assume that the eigenvalues are numbered such that $\lambda_1 \geq \lambda_2 \geq \lambda_3$ and so on. Recall that *Rayleigh's principle* [12] states that the jth eigenvalue λ_j for $1 \leq j \leq n$ is given by the variational formula

$$\lambda_j = \max\{\langle Rw, w\rangle | w \in L^2(\mu), \|w\|_2 = 1, w \perp v_1, v_2, ..., v_{j-1}\} \tag{2.33}$$

where orthogonality is implied with respect to the $L^2(\mu)$ inner product, and v_i is the ith eigenvector of R. We note the following theorem about the properties of a self-adjoint operator (like R).

Theorem 4. *Let $R : L^2(\mu) \to L^2(\mu)$ be a self adjoint operator. Then the following equality holds [13]*

$$\lambda_k + \lambda_{k-1} + ... + \lambda_1 = max\left\{\sum_{i=1}^{k} \langle R\phi_i, \phi_i\rangle | (\phi_1, ..., \phi_n) \text{ is an orthonormal system}\right\} \tag{2.34}$$

We apply the above theorem to the discretized operator R as defined in 2.31, operating on the finite-dimensional space. Let $\mathbf{1}_A$ be the characteristic vector of any set A, i.e., it is a n-vector defined over X with ith entry equal to 1 if $B_i \in A$ and equal to 0 otherwise. We can rewrite the expression for $\rho_\mu(A)$ as

$$\frac{< R\mathbf{1}_A, \mathbf{1}_A >}{< \mathbf{1}_A, \mathbf{1}_A >} \tag{2.35}$$

Let X_j be the normalised characteristic vector of set A_j, i.e.,

$$X_j = \frac{\mathbf{1}_{A_j}}{< \mathbf{1}_{A_j}, \mathbf{1}_{A_j} >} \tag{2.36}$$

It is easy to see that the X_j's form an orthonormal system given a partition $\{A_1, A_2, ..., A_k\}$. The following result, which given an upper bound on the quantity ρ_μ is an immediate consequence.

$$\rho_\mu = \rho_\mu(A_1) + \rho_\mu(A_2) + ... + \rho_\mu(A_k) \leq 1 + \lambda_2 + \lambda_3 + ... + \lambda_k \tag{2.37}$$

A lower bound on ρ_μ can also be derived using the above mentioned properties of R, and we get the following expression,

$$\rho_\mu > 1 + r_2\lambda_2 + r_3\lambda_3 + ... + r_k\lambda_k + c, \tag{2.38}$$

where Q is the projection on the subspace spanned by X_js,

$$r_j = \|Qv_j\|^2 = \langle Qv_j, Qv_j\rangle \in [0, 1] \tag{2.39}$$

and

$$c = a(1 - r_2 + 1 - r_3 + ... + 1 - r_k) \tag{2.40}$$

Here $a > -1$ is the infimum of the real-spectrum of the operator R. While the problem of finding an optimal partition is an ill-posed one [14], the above bounds have motivated the development of a number of heuristic methods in recent years. We describe the method followed in this dissertation below.

Two almost invariant sets: We will use the second eigenvector v_2 of R to form a partition $\{A_1, A_2\}$ of the phase space X such that both the objectives mentioned above are satisfied. It is clear that since v_2 is orthogonal to the vector $v_1 = p$ (which is positive everywhere because it is an invariant measure of the system), it has both positive and negative entries. The lower bound of the above theorem suggests that the closer v_2 is to being a constant function on different components of the partition, the closer the lower bound will be to the upper bound, and hence the resulting value of ρ_μ will be higher. Hence a natural partition that one arrives at is to use the zero-contour of v_2 as the boundary between A_1 and A_2. This division also ensures that the two components of the partition have almost equal measure. Hence, it follows that if $I_1 = \{i|(v_2)_i > 0, 1 \leq i \leq n\}$ and $I_2 = \{i|(v_2)_i < 0, 1 \leq i \leq n\}$, then $A_1 = \cup_{i\in I_1} B_i$ and $A_2 = \cup_{i\in I_2} B_i$.

A modified heuristic is to use a value c close to 0 as the boundary between A_1 and A_2. Usually [14], a search through various values of c is done by calculating ρ_μ for different resulting partitions, and the one will the highest value of ρ_μ is selected. That is, if $I_1 =$

$\{i|(v_2)_i > c, 1 \leq i \leq n\}$ and $I_2 = \{i|(v_2)_i < c, 1 \leq i \leq n\}$, then $A_1 = \cup_{i \in I_1} B_i$ and $A_2 = \cup_{i \in I_2} B_i$.

2.3 Topological Methods

2.3.1 Important concepts and definitions

The term advection refers to transport of material by a fluid flow in which the velocity of a material particle equals the velocity of the underlying velocity field, i.e., if the velocity field of the fluid is given by $v(x,t)$, then the particle obeys

$$\dot{x} = v(x,t), \tag{2.41}$$

and this is called the advection equation. When the advection equations are non-integrable, the particle trajectories are also chaotic and this phenomenon is called **chaotic advection** [15]. This concept is a very important tool for analyzing and obtaining mixing enhancements in laminar flows. There are a number of ways to measure the amount of mixing in such fluid flows and topological entropy is one of the most important one.

For any discrete dynamical system, the **topological entropy** h, of a system is a quantitative measure of its orbit complexity [11]. It is a purely topological quantity, and does not depend on any underlying measure of the system, i.e., it treats all orbits of the system as equal. Let $N(n,\epsilon)$ be the number of different orbits of length n of a given discrete dynamical system, if the least measurable distance is ϵ, i.e., two nearby points are considered distinct if they are more than ϵ apart. This quantity is called the maximum cardinality $N(n,\epsilon)$ of a (n,ϵ) separated set. Then, the topological entropy of the map f is formally defined by

$$h(f) = \lim_{\epsilon \to 0} \left(\lim_{n \to \infty} \sup \left(\frac{1}{n} \log N(n,\epsilon) \right) \right) \tag{2.42}$$

Hence, the topological entropy is the *exponential* rate of increase in the number of such orbits in the asymptotic limit $n \to \infty$ and $\epsilon \to 0$.

In case of two-dimensional smooth flows, an appropriate Poincare map is first computed. The line-stretching exponent for this map, which is the maximum stretching over all possible initial material lines is equal to the topological entropy of the flow [16]. For instance, the

actual topological entropy of a two-dimensional bounded flow with stirrers inserted can be determined by computing the stretching rate of topologically nontrivial lines, such as loops that encircle exactly two of the stirring rods or lines that join a stirring rod with the outer boundary [17].

2.3.2 Topological chaos and the Thurston-Nielsen classification theorem

Topological chaos in the context of fluid mechanics refers to the complexity in the system that is "built in" to the flow due to the topology of boundary motions, which cannot be removed by continuous perturbation of the fluid while keeping the boundaries fixed. This implies that unless there is a change in topology of the boundary motions, there is a minimum guaranteed amount of complexity that will always be present in the flow.

Consider a N-punctured fluid domain in two dimensions (i.e., a two-dimensional domain with the regions bounded by N curves homeomorphic to a circle removed from it) and denote it by R_N. Let the punctures undergo a prescribed cyclic motion, and then return to their initial position at end of the cycle. By the continuity and smoothness assumption, the punctures have dragged the fluid along with them. Assume the flow is periodic with period T, and denote by f the time T-map of the fluid flow over R_N. Since f represents a physical, differentiable fluid flow motion, it is by definition an orientation preserving diffeomorphism, and contains all the information about the fluid flow. The Thurston-Nielsen (TN) classification theorem [17] provides a way to obtain important topological properties of f without actually solving for it (either analytically or numerically). Two diffeomorphisms are said to be **isotopic** if they can be continuously deformed into each other. Hence, the **isotopy class** of f is the set of all diffeomorphisms isotopic to f. Hence, each such isotopy class can be represented by just one member belonging to that class, called the representative. This theorem guarantees that there exists a representative f' (called the Thurston-Nielsen representative) in the isoptopy class of f, that belongs to one of the following three categories,

1) *Finite-order*: If f'^n is isotopic to the *identity* for some positive integer n.
2) *Pseudo-Anosov* (pA): f' stretches fluid elements by a factor of $\lambda > 1$, so that repeated applications give exponential stretching of material lines.
3) *Reducible*: f' leaves a family of curves invariant which delineate regions in the domain that are of one of the two types described above (i.e., isotopic to identity or pA).

The theorem also states that the topological entropy of the TN-representative f' is a lower bound on the topological entropy of f, i.e., the dynamics of f will be at least as complicated as those of f'.

2.3.3 Braiding in three-dimensional space-time, and computation of topological entropy of pseudo-Anosov braids

In order to compute the topological entropy of the TN-representative in the pA case, a mathematical representation of f' acting on R_N can be generated. The motion of N-punctures can be represented in space-time by N trajectories $(x_i(t), y_i(t), t)$ for $i = 1$ to N, where $x_i(t), y_i(t)$ represent the position of ith puncture at time t. These N trajectories interchange positions while moving around each other in three-dimensions (two of space and one of time), and define a physical braid on N strands. Each braid consists of several "interchanges" between 2 trajectories (or strands) at a time. For example, 3 different types of interchange motions are shown in figure 2.9.

Artin's braid group [18] provides a mathematical framework to label and identify these interchanges. Each such interchange is a generator for the overall braid. It is labeled as σ_i if the ith and $(i+1)$th strands interchange their positions clockwise and it is labeled σ_i^{-1} or equivalently σ_{-i} if the same interchange happens anti-clockwise. Note that the index i here refers to the current position of a strand obtained by projecting the positions on x-axis and counting from the left, and hence it does not always refer to same strand.

The interchange protocols shown in figure 2.9 R_+, L_+ and L_- are hence labeled as σ_2, σ_1

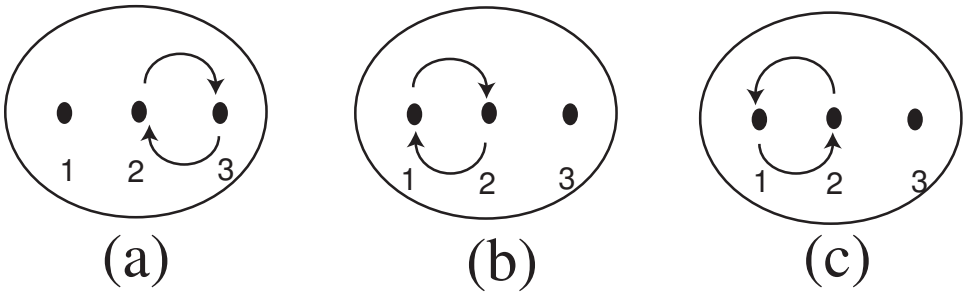

Figure 2.9: Illustration of stirring motions. From left to right: R_+ motion, L_+ motion, L_- motion

and σ_{-1} respectively. The braiding motion corresponding to any pA representative can be written as product of various generators. By convention, a braiding sequence involving R_+ followed by L_- is written as $\sigma_{-1}\sigma_2$. In figure 2.10, we show the formal representation of pseudo Anosov braid given by $\sigma_{-1}\sigma_2$, and a finite order braid by $\sigma_1\sigma_2$.

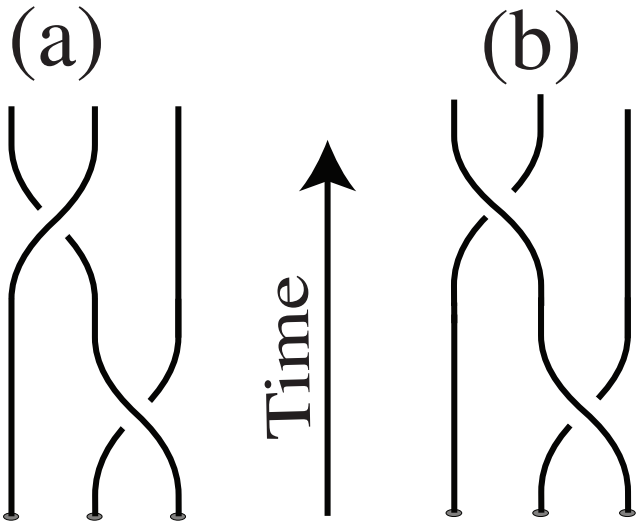

Figure 2.10: (a) A pseudo Anosov braid $\sigma_{-1}\sigma_2$ (b) A finite order braid $\sigma_1\sigma_2$.

The braid group on N strands can be represented in terms of $(N-1)\times(N-1)$ matrices, called the Barau representation [19]. For $N=3$, the topological entropy of the braid is can be obtained by as follows. Each generator in the braiding sequence can be represented by a 2×2 matrix. These matrices can be multiplied to arrive at the matrix representation

M of the braid, which is the irreducible transition matrix for the Markov partition of a two-dimensional pseudo-Anosov map. This pseudo-Anosov map is isotopic to the map f. Hence, f will have at least as much complexity as this pA map, and this complexity can be measured by calculating the eigenvalues of M. For example, in the braid considered above, the two eigenvalues are $\lambda = \frac{1}{2}(3 + \sqrt{5})$ and $\frac{1}{\lambda} = \frac{1}{2}(3 - \sqrt{5})$. This implies that the pA map stretches in the unstable direction (i.e., along the eigenvector corresponding to λ) by λ and contracts in the stable direction (i.e., along the eigenvector corresponding to $1/\lambda$) by factor of $\frac{1}{\lambda}$. This behavior is preserved by isotopy and hence the map f will have motions that produces stretching of at least λ. In case of $N > 3$, the leading eigenvalue does not give the exact value of topological entropy of the braid, and hence a more powerful algorithm is used to obtain accurate values. The most commonly used method in this case, called the Bestvina-Handel algorithm [20] has a freely available software implementation [21] called the train-track code, that is used in this dissertation. The train-tracks algorithm computes the graph of the movement of edges between rods that are undergoing braid operations. The algorithm determines the least amount of stretching that an elastic band connected to rods will undergo during the motion, which is equivalent to the stretching of material lines [22].

More detailed discussion of application of Thurston Nielsen classification theorem in the context of chaotic advection can be found in [17].

Chapter 3

Design Of Fuel Efficient Trajectories In A Planet-Moon Environment

3.1 Introduction

Low energy spacecraft trajectories such as multi-moon orbiters for the Jupiter system can be obtained by harnessing multiple gravity assists by moons in conjunction with ballistic capture to drastically decrease fuel usage [23, 24, 25]. These phenomena have been explained by applying techniques from dynamical systems theory to systems of n bodies considered three at a time [26, 27, 28, 29, 30]. One can design trajectories with a predetermined future and past, in terms of transfer from one Hill's region to another. Using this approach, which has been dubbed the "Multi-Moon Orbiter" (MMO) [23], a scientific spacecraft can orbit several moons for any desired duration, instead of flybys lasting only seconds. This approach should work well with existing techniques, enhancing interplanetary trajectory design capabilities for missions in planet-moon environments. The approach is quite flexible in the sense that the spacecraft can be made to respond to unforeseen events, and can be made to revisit any region using little fuel.

The aim of this chapter is to describe a methodology using the analytically derived Keplerian map [1] to obtain trajectories with a realistic time-of-flight (i.e., measured in months instead of years in case of uncontrolled trajectories), using small control inputs in the form of instantaneous ΔVs.

We describe briefly the PCR3BP in section 3.2, and mention important results from the literature. The Keplerian map, which is the analytical tool used in the process of finding desired trajectories is described in the next section. Next, we derive an exact periapse map via Hamilton-Jacobi theory. We then review the framework of breaking down the multi-moon trajectory design problem into two 3-body problems and describe a method of finding zero-fuel trajectories that go from one moon to the other using the Keplerian map. Using this framework, we then describe the methodology for generating low energy trajectories that can be completed in reasonable time using small control inputs. We also discuss the tradeoff between fuel consumption and time-of-flight for the family of trajectories obtained using this method.

3.2 Planar circular restricted three body problem (PCR3BP)

In this section, we give a very brief overview of the PCR3BP. An excellent reference for this section is [31].

3.2.1 Basic set-up and equations of motion

Consider the motion of a particle P of negligible mass moving under the gravitational influence of two masses m_1 and m_2, referred to as the primaries. We assume that m_1 and m_2 have circular orbits about their common center of mass. The particle P is free to move in the plane defined by the circular orbits of the primaries, but cannot affect their motion. In

the context of this chapter, it is helpful to imagine that m_1 represents the planet and m_2 represents a moon, and we analyze the motion of P, a spacecraft of comparatively negligible mass, such that it does not affect the motion of m_1 and m_2.

We non-dimensionalize the system by taking the units as follows: one unit of mass is equal to $m_1 + m_2$; one unit of length equals the fixed distance between m_1 and m_2 (i.e., the distance between the centers of the planet and moon); one unit of time is chosento make the orbital period of m_1 and m_2 about their center of mass equal to 2π. This choice of units results in universal constant of gravitation becoming unity (i.e., $G = 1$). The only parameter of the system is the mass parameter, $\mu = \dfrac{m_2}{m_1 + m_2}$. This parameter μ is a measure of the amount of perturbation to the 2-body problem consisting of the planet and spacecraft P. Define $\mu_1 = 1 - \mu$ and $\mu_2 = \mu$. Here $r_1 = \sqrt{(x + \mu_2)^2 + y^2}$ and $r_2 = \sqrt{(x - \mu_1)^2 + y^2}$ are the distances to P from m_1 and m_2, respectively.

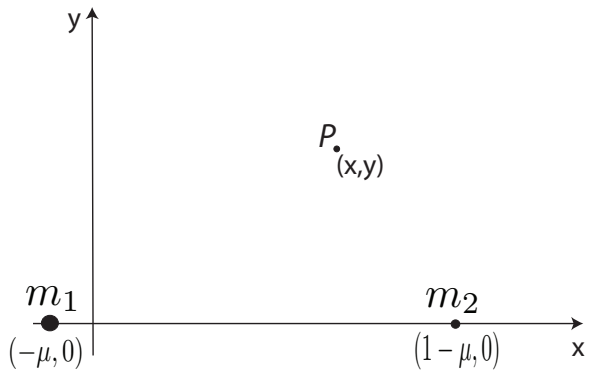

Figure 3.1: Rotating coordinate system and position of the various masses in PCR3BP.

The Langrangian L of the system in the rotating frame (shown in figure 3.1) moving with the planet-moon system is

$$L(x, y, \dot{x}, \dot{y}) = \frac{1}{2}((\dot{x} - y)^2 + (\dot{y} + x)^2) - U(x, y) \tag{3.1}$$

where $U(x, y)$ is the gravitational potential given by

$$U(x, y) = -\frac{\mu_1}{r_1} - \frac{\mu_2}{r_2} - \frac{1}{2}\mu_1\mu_2 \tag{3.2}$$

We define the *augmented* potential $\widetilde{U}(x, y)$ as

$$\widetilde{U}(x, y) = -\frac{1}{2}(x^2 + y^2) + U(x, y) \tag{3.3}$$

where the extra term $-\frac{1}{2}(x^2 + y^2)$ is the centrifugal potential, arising from the fact that the equations are written in the rotating frame. The equations of motion of P in the rotating frame are

$$\ddot{x} - 2\dot{y} = -\widetilde{U}_x,$$
$$\ddot{y} + 2\dot{x} = -\widetilde{U}_y$$

The Hamiltonian form of above equations is more useful for our analysis. The Legendre transformation transforms a system of equations given in Lagrangian formulation into the Hamiltonian formulation. For a general Lagrangian $L(\mathbf{q}, \dot{\mathbf{q}})$, where $\mathbf{q} = (q_1, q_2, ...)$ and $\dot{\mathbf{q}} = (\dot{q_1}, \dot{q_2}, ...)$, we define momenta as $p_i = \dfrac{\partial L}{\partial q_i}$. Each $\dot{q}_i$ can be expressed as $\dot{q}_i(\mathbf{q}, \mathbf{p})$ and then the Hamiltonian of the system can be defined as $H(\mathbf{p}, \mathbf{q}) = \sum_i \dot{q}_i p_i - L(\mathbf{q}, \dot{\mathbf{q}})$.

Using the Legendre transformation for our system, we get the following system of equations

$$\dot{x} = \frac{\partial H}{\partial p_x} = p_x + y$$
$$\dot{y} = \frac{\partial H}{\partial p_y} = p_y - x$$
$$\dot{p}_x = -\frac{\partial H}{\partial x} = p_y - x - \widetilde{U}_x$$
$$\dot{p}_y = -\frac{\partial H}{\partial y} = -p_x - y - \widetilde{U}_y$$

Where the Hamiltonian $H(x, y, p_x, p_y)$ is

$$H(x, y, p_x, p_y) = \frac{1}{2}((p_x + y)^2 + (p_y - x)^2) + \widetilde{U}(x, y) \tag{3.4}$$

And p_x, p_y are the conjugate momenta to x and y, respectively

$$p_x = \dot{x} - y \tag{3.5}$$

$$p_y = \dot{y} + x \tag{3.6}$$

We can also express the energy of the system in terms of $(x, y, \dot{x}, \dot{y})$ as

$$E(x, y, \dot{x}, \dot{y}) = \frac{1}{2}(\dot{x}^2 + \dot{y}^2) + \widetilde{U}(x, y) \tag{3.7}$$

Traditionally, the Jacobi integral $C(x, y, \dot{x}, \dot{y})$ $(=-2H(x, y, p_x, p_y))$ has been used in celestial mechanics community.

Osculating orbital elements and Hamiltonian equations

In celestial mechanics, a set of elements called the 'osculating' orbital elements is often used. These elements represent an instantaneous approximation of the motion of body as a (elliptical) Keplerian orbit in presence of a perturber. r is the distance from m_1 to P, a denotes the semi-major axis of the osculating ellipse, e is the eccentricity, ω is the angle of periapse of the ellipse measured from the inertial X axis, while $\bar{\omega}$ represents the periapse angle measured in the rotating frame. ν is the true anomaly and θ is the angle formed between the rotating x axis and the vector to the particle P from m_1. Figure 3.2 explains the various orbital elements in case of a massive central body m_1 and a perturber m_2. The time-independent Hamiltonian for the PCR3BP in the rotating frame can be expressed in these osculating elements up to first order in μ as follows:

$$H(a, e, \bar{\omega}, \nu) = H_0 + \mu H_p \tag{3.8}$$

where

$$H_0 = -\frac{1}{2a} - G \tag{3.9}$$

$$H_p = \frac{1}{r} + \frac{cos(\theta)}{r^2} - \frac{1}{\sqrt{r^2 + 1 - 2rcos(\theta)}} \tag{3.10}$$

$$r = \frac{a(1 - e^2)}{1 + ecos(v)} \tag{3.11}$$

$$\theta = \bar{\omega} + v = \omega - t + v; \tag{3.12}$$

Here $G = \sqrt{a(1 - e^2)}$ is the angular momentum of the particle P. Denote by r_2 the distance between m_2 and the particle P, then $r_2 = \dfrac{1}{\sqrt{r^2 + 1 - 2rcos(\theta)}}$.

3.2.2 Geometrical structure

Understanding the geometrical structure of the invariant manifolds of various fixed points of PCR3BP in the planet-moon environment gives deep insight into the phase space transport occurring in the this problem. The effective potential $\widetilde{U}(x, y)$ is plotted in figure 3.3 for $\mu = 0.3$. Also shown are the five Lagrange points (L_1 through L_5), which are fixed points in the rotating reference frame.

For fixed value of energy e, the dynamics in PCR3BP are restricted to a three dimensional manifold (in the four-dimensional phase space), given by

$$\mathbf{M} = [(x, y, \dot{x}, \dot{y}) : E(x, y, \dot{x}, \dot{y}) = e] \tag{3.13}$$

The projection of this surface on the position space is given by

$$M = [(x, y) : \widetilde{U}(x, y) < e], \tag{3.14}$$

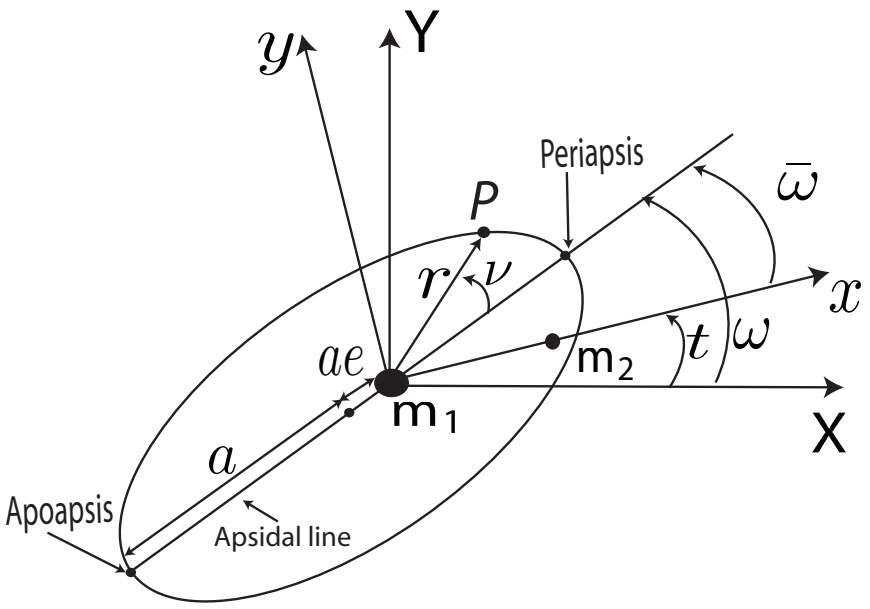

Figure 3.2: Various osculating orbital elements are shown in this figure, representing the instantaneous approximation of the motion of the body P as a Keplerian orbit around the massive body m_1. X-Y axes represent the inertial frame, while x-y axes represent the frame which rotates with the perturber m_2.

The boundaries of this projected surface, known as *zero velocity curves* delineate the regions in phase space in which the motion is allowed for that particular energy value. This results in five qualitatively different cases, depending on value of e, and are shown in figure 3.4. We denote by E_i the energy associated with the fixed point L_i, $i = 1, 2, 3, 4, 5$. The five cases are as follows:

- Case 1: $e < E_1$. The particle cannot move from the realm around m_1 to the realm around m_2 or vice-versa. Also, it cannot go from exterior realm to either of the interior realms or vice-versa.

- Case 2: $E_1 < e < E_2$. The particle can move between realms around m_1 and m_2, but cannot go from interior to exterior realms or vice-versa.

- Case 3: $E_2 < e < E_3$. In addition to moving between realms around m_1 and m_2, the particle can now travel between exterior and interior realms via the neck around L_2.

- Case 4: $E_3 < e < E_4 = E_5$. In this energy case, the particle near m_1 can travel to exterior realms directly via the neck around L_3, in addition to the motion possible in case 3.

- Case 5: $E_4 < e$. There is no forbidden region in this case, and the particle is free to travel to any region in x-y plane.

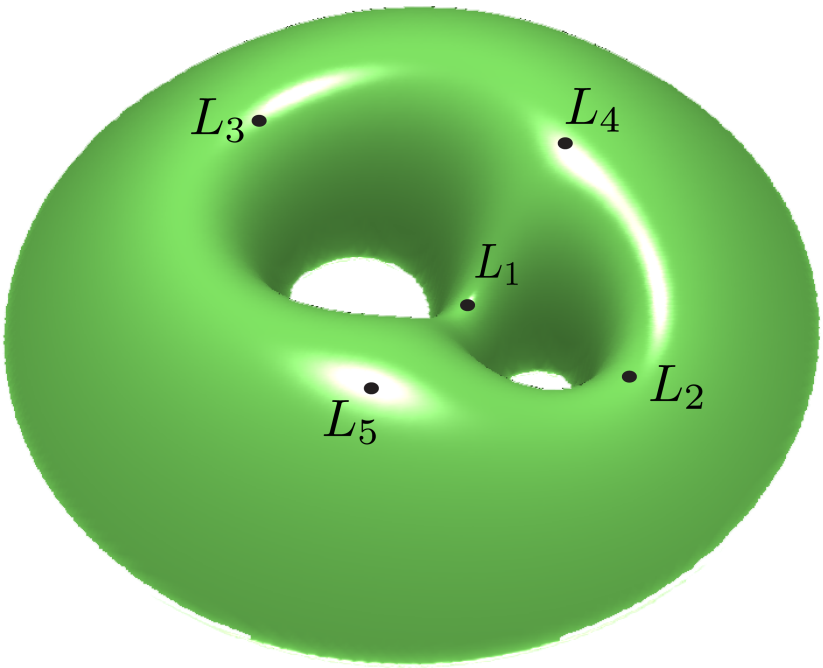

Figure 3.3: Effective potential $\widetilde{U}(x, y)$ for $\mu = 0.3$. The five critical points of this potential, L_1 through L_5, which are the fixed points of the PCR3BP in the rotating frame, are also shown.

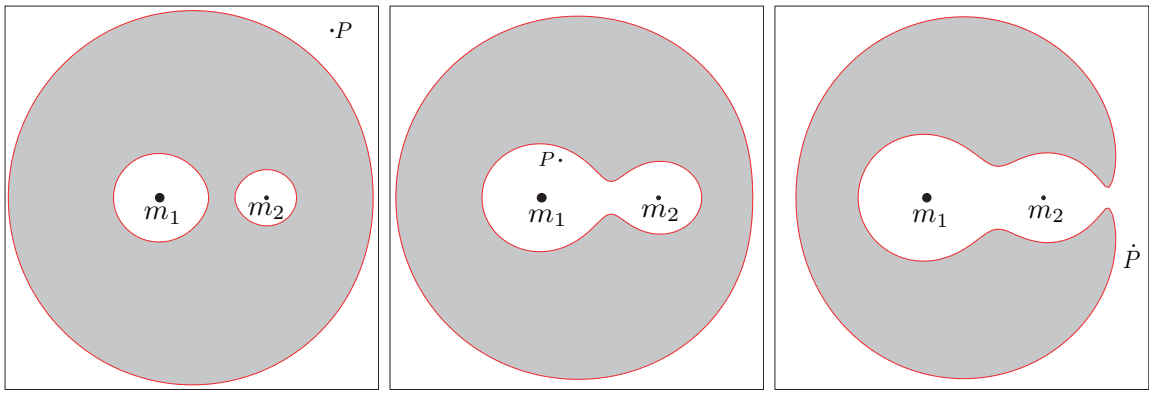

(a) Case 1: $e < E_1$ (b) Case 2:$E_1 < e < E_2$ (c) Case 3:$E_2 < e < E_3$

(d) Case 4:$E_3 < e < E_4$ (e) Case 5:$E_4 < e$

Figure 3.4: The zero velocity curves, and the division in x-y plane by these curves is shown for $\mu = 0.3$. Depending upon the value of energy e of the particle P, this division results in five different scenarios. The particle can move in the white region, while the grey region is forbidden i.e., inaccessible at that particular level of energy.

Dynamics near the Lagrange points L_1 and L_2

Analysis of the linearized dynamics near L_1 and L_2 can surprisingly reveal a lot of information about the global (inter-realm) transport in the PCR3BP. The key result here is that the stable and unstable cylindrical manifolds (i.e., $S^1 \times \Re^1$ geometry) of the periodic orbits around these two fixed points (called the Lyapunov orbits) separate two distinct types of motion: transit orbits and non-transit orbits. The transit orbits, passing from one realm to another, are those inside the cylindrical manifold, or tube. The non-transit orbits, which bounce back to their realm of origin, are those outside the tube. In figure 3.5, we show those tubes (i.e., invariant manifolds of unstable periodic orbit around L2) mediating transport between exterior realm and moon realm. The main computations involved in obtaining phase space structure in PCR3BP are as follows

- Find the fixed points L_1 and L_2 using the Hamiltonian equations of motion in the rotating frame.
- Linearize the system dynamics around each of those two fixed points and find the eigenvalue/vectors of the Jacobian at the fixed points. Since the fixed points have the saddle $\times$ center geometry, the eigen-spectrum consists of a purely imaginary complex conjugate pair, and a pair of real eigenvalues with opposite signs.
- To better understand the geometry of flow around in the equilibrium region, perform a change in coordinates by taking the new axes in the four dimensional phase space to lie along the eigenvectors of the Jacobian.
- Invariant manifolds of the periodic orbits around the two fixed points are then revealed to be the envelopes that enable transport between the different realms in the PCR3BP.

The reader is referred to [28] for an extensive treatment of this topic.

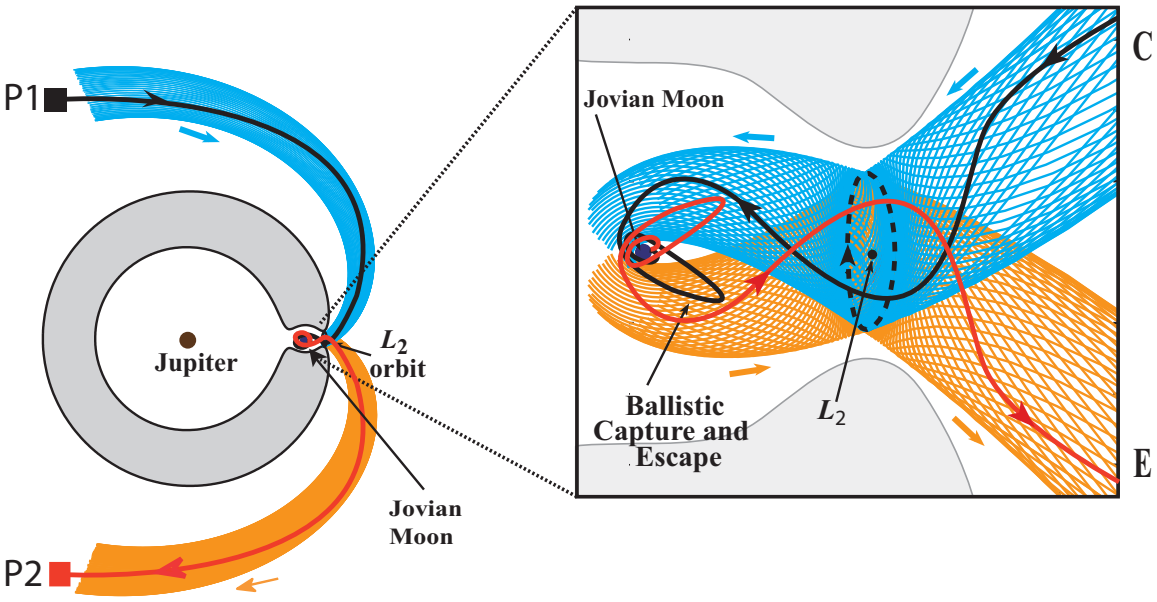

Figure 3.5: Tube dynamics near L_2: The particle P1 which starts out in a manifold tube of the exterior Lagrange point L_2 is ballistically captured into an unstable elliptical orbit around the moon and may soon impact with the moon. Another particle P2, with a velocity slightly above escape velocity, escapes from the moon region via the neck region, again by passing through the tubes. This figure is a modified version of the figure 6.2 in [1].

3.3 Keplerian Map for evolution under natural dynamics of PCR3BP

We use a family of two-dimensional symplectic twist maps to approximate a particles motion in the planar circular restricted three-body problem with Jacobi constant near 3. The maps model a particle on a near-Keplerian orbit about a central body of unit mass, where the spacecraft is perturbed by a smaller body of mass μ. Each map, which we call the *Keplerian map*, is an update map for the angle of periapse ω in the rotating frame and Keplerian energy K (which equals $-\frac{1}{2a}$), $(\omega_n, K_n) \mapsto (\omega_{n+1}, K_{n+1})$. The map has the form

$$\begin{pmatrix} \omega_{n+1} \\ K_{n+1} \end{pmatrix} = \begin{pmatrix} \omega_n - 2\pi(-2(K_n + \mu f(\omega_n; C_J, \bar{K})))^{-3/2} \\ K_n + \mu f(\omega_n; C_J, \bar{K}) \end{pmatrix} \tag{3.15}$$

i.e., a map of the cylinder $\mathcal{A} = S^1 \times \mathbf{R}$ onto itself. This two-dimensional symplectic twist map is an approximation of a Poincaré map of the planar circular restricted three-body problem (PCR3BP), where the surface of section is at periapsis in the space of orbital elements. For this reason, eq. (3.15) could be considered a periapse map.

3.3.1 Derivation

We describe the main steps in the derivation of this map in this section. This map was first derived in [1] and we follow that derivation closely. Recall again that the Hamiltonian of the PCR3BP in the rotating frame is given by

$$H(a, e, \bar{\omega}, \nu) = H_0 + \mu H_p \tag{3.16}$$

where

$$H_0 = -\frac{1}{2a} - G \tag{3.17}$$

$$H_p = \frac{1}{r} + \frac{cos(\theta)}{r^2} - \frac{1}{\sqrt{r^2 + 1 - 2rcos(\theta)}} \tag{3.18}$$

$$r = \frac{a(1-e^2)}{1 + ecos(\nu)} \tag{3.19}$$

$$\theta = \bar{\omega} + \nu = \omega - t + \nu \tag{3.20}$$

$$G = \sqrt{a(1-e^2)} \tag{3.21}$$

$$r_2 = \frac{1}{\sqrt{r^2 + 1 - 2rcos(\theta)}} \tag{3.22}$$

The main steps in the derivation are

- Integrate the perturbations on the spacecraft P due to the small perturber m_2, assuming that the spacecraft is on an elliptical Keplerian orbit around the massive body m_1, and find the change in angular momentum (ΔG) over one complete orbit.
- Use the invariance of Jacobi constant to arrive at the functional dependence of ΔK on ω and K, by relating ΔG and the change in Keplerian energy i.e., ΔK.
- Approximate the change in ω, i.e., Δw as a function of K and ω.
- Compute the ΔK values for a fixed value of K, which makes the map area-preserving, a property of the map computed numerically from the full PCR3BP equations.

We begin the derivation by noting that using the canonical form of the Lagrange planetary equations [32], the change in angular momentum G can be written in differential form as

$$\frac{dG}{dt} = -\mu \frac{\partial H_p}{\partial \omega} \tag{3.23}$$

For this perturbing function, we have

$$H_p \;=\; -\frac{1}{\sqrt{1 + r^2 - 2\ r\cos(\omega - t + \nu)}} + \frac{\cos(\omega - t + \nu)}{r^2} + \frac{1}{r} \tag{3.24}$$

Hence the R.H.S of (3.23) can be calculated using

$$\frac{\partial H_p}{\partial \omega} = \frac{r}{r_2^3}\sin(\omega+\nu-t) - \frac{1}{r^2}\sin(\omega+\nu-t). \tag{3.25}$$

We use the above expression along with (3.23) to calculate the change in G over one complete orbit of the spacecraft. Equation (3.23) is treated as a differential equation w.r.t time. The expression can be integrated for a fixed value of ω over a complete orbit i.e., from apoapse to apoapse. We employ a change in variables, and use the true anomaly ν as the integrating variable. The relation between true anomaly ν and time can be obtained via Kepler's equation i.e., by noting that

$$l = 2\pi(t/T) \tag{3.26}$$

$$l = \lambda - e\sin\lambda \tag{3.27}$$

$$\tan(\nu/2) = \sqrt{\frac{1+e}{1-e}}\tan(\lambda/2) \tag{3.28}$$

where λ is known as the eccentric anomaly and l is the mean anomaly. The time period of an unperturbed Keplerian orbit is $T = 2\pi a^{3/2}$. The distance r can be expressed in terms of the true anomaly as $r = \dfrac{a(1-e^2)}{1+e\cos\nu}$. Using the above information, we can carry out the integration as follows

$$\begin{aligned}
\Delta G &= -\mu\int_{-T/2}^{T/2}\frac{\partial H_p}{\partial\omega}\,dt \\
&= -\mu\int_{-T/2}^{T/2}\left[\frac{r}{r_2^3}\sin(\omega+\nu(t)-t) - \frac{1}{r^2}\sin(\omega+\nu(t)-t)\right]dt \\
&= -\frac{\mu}{G}\int_{-\pi}^{\pi}\left[\left(\frac{r}{r_2}\right)^3\sin(\omega+\nu-t(\nu)) - \sin(\omega+\nu-t(\nu))\right]d\nu \\
&= -\frac{\mu}{G}\left[\left(\int_{-\pi}^{\pi}\left(\frac{r}{r_2}\right)^3\sin(\omega+\nu-t(\nu))\,d\nu\right) - \sin\omega\left(2\int_0^{\pi}\cos(\nu-t(\nu))\,d\nu\right)\right]. \qquad (3.29)
\end{aligned}$$

where the integration is carried from apoapse to apoapse.

Next, we note that by the invariance of the Jacobi constant we have $\Delta H = 0$ in the rotating

frame and therefore using 3.16 (note $K = -\frac{1}{2a}$)

$$\Delta H = \Delta K - \Delta G + \mu \Delta H_p = 0 \tag{3.30}$$

$$\Delta K = \Delta G - \mu \Delta H_p, \tag{3.31}$$

where

$$\begin{aligned} \Delta H_p &= H_p(\nu = \pi) - H_p(\nu = -\pi), \\ &= \frac{1}{\sqrt{1 + Q^2 + 2\ Q\cos(\omega + \tau)}} - \frac{1}{\sqrt{1 + Q^2 + 2\ Q\cos(\omega - \tau)}} + \frac{2}{Q^2}\sin\omega\sin\tau \end{aligned}$$

with $Q = a(1 + e)$ and $\tau = \pi a^{3/2}$, the apoapsis distance and half period of the unperturbed orbit, respectively.

ΔK is a function of ω, K, and e but the invariance of the Jacobi constant yields a relationship between these three variables, implying $\Delta K = \Delta K_{C_J}(\omega, K)$, where C_J is a parameter. The expression (3.31) can be written as $\Delta K_{C_J} = \mu f(\omega, K)$, where f is the *energy kick function*. We can approximate the energy kick ΔK_{C_J} between consecutive apoapsis passages as a discrete event occurring at periapsis passage, and assume that the particle moves in an unperturbed orbit for all times except at each periapse, where it receives the kick that changes its Keplerian energy (and hence it shifts to another Keplerian orbit). For values of K and C_J that we are concerned with, the maximum contribution of $\mu\Delta H_p$ is much smaller than that of ΔG, so we ignore it, i.e., we assume that $\mu\Delta H_p \ll \Delta G$ and

$$f(\omega, K) = \Delta K_{C_J}(\omega, K)/\mu = \Delta G/\mu, \tag{3.32}$$

Note that we want to derive a periapse map that gives us the evolution of an initial condition (at peripapse) on a given PCR3BP energy surface (defined by the pair (μ, C_J)). For our trajectory design purposes, typical values of parameters imply $\mu \ll 1$ and $C_J \approx 3$, which is close to the Jacobi constant of L_2. Our aim is to compute the sequence of pairs (ω_n, K_n), $n = 1, 2, 3, ...$ which result from an initial condition (ω_0, K_0). We assume $t = 0$ at time of periapse. This implies $\omega = \bar{\omega}$ at the periapse (i.e. when the kick is assumed to take place)

and hence we have dropped the bar and will now use only ω. The (ω_n, K_n) pairs represent the angle of periapse in the rotating frame of the PCR3BP and the Keplerian energy of the instantaneous Keplerian orbit of the particle. We have already described the process to compute the change in K, by deriving the kick assumed to be received by the spacecraft at each periaspe. In our approximation, (ω_n, K_n) represents the particle's orbit just before receiving an energy kick. Immediately following the kick, the orbit becomes (ω_{n+1}, K_{n+1}). The time until the next periapsis passage is $\Delta t = 2\pi a_{n+1}^{3/2} = 2\pi(-2K_{n+1})^{-3/2}$. The change in the periapsis angle ω during this period is $\Delta\omega = 2\pi - \Delta t$. Since the variable ω is defined mod 2π, therefore $\Delta\omega = -\Delta t \bmod 2\pi$.

We have neglected the direct effect of the gravity interaction on the argument of periapsis, and the only change in ω is due to the instantaneous change in Keplerian energy, which in turn changes the time period of the Keplerian orbit, and hence, has an effect of changing the relative *phase* of the instantaneous ellipse w.r.t the rotating coordinate system. We obtain a two-dimensional update map at periapse for the four-dimensional PCR3BP (restricted to an energy manifold)

$(\omega_{n+1}, K_{n+1}) = F(\omega_n, K_n)$ of the cylinder $\mathcal{A} = S^1 \times \Re$ onto itself, i.e., $F : \mathcal{A} \to \mathcal{A}$ where

$$F\begin{pmatrix} \omega_n \\ K_n \end{pmatrix} = \begin{pmatrix} \omega_{n+1} \\ K_{n+1} \end{pmatrix} = \begin{pmatrix} \omega_n - 2\pi(-2K_{n+1})^{-3/2} \pmod{2\pi} \\ K_n + \mu f(\omega_n, K_n) \end{pmatrix}. \tag{3.33}$$

We find the Jacobian determinant of F to be $1+\mu\frac{\partial f}{\partial K}$. The map is clearly not area-preserving for a general K dependence of the kick-function f. But if we assume f is independent of K then we have a symplectic (area-preserving) twist map, which is a a property of the Periapse map computed numerically by integration of PCR3BP equations. This assumption also leads to simplification of analysis involved in computing controlled trajectories. It is also a desirable property for maps in general [5, 33]. Hence, we take a reference value of $K = \bar{K}$, and let $f(\omega) = f(\omega, \bar{K})$ and thereby make F area-preserving:

$$F\begin{pmatrix} \omega_n \\ K_n \end{pmatrix} = \begin{pmatrix} \omega_{n+1} \\ K_{n+1} \end{pmatrix} = \begin{pmatrix} \omega_n - 2\pi(-2K_{n+1})^{-3/2} \pmod{2\pi} \\ K_n + \mu f(\omega_n) \end{pmatrix}. \tag{3.34}$$

We can calculate the twist of this map

$$\left.\frac{\partial \omega_{n+1}}{\partial K_n}\right|_{\omega_n} = 3\pi \left(-2(K_n + \mu f(\omega_n)\right)^{-5/2} > 0, \tag{3.35}$$

for $K_n < -\mu f(\omega_n)$. The twist is to the right, which means that the Keplerian energy K acts like velocity for the ω coordinate i.e., higher the value of K, bigger is the change in ω over one iteration.

We compute the value of the integral numerically by quadrature, assuming an average value of K (called $\bar{K}$) over the region where the map is being used. Due to the form of the integrals, the resulting function $f(\omega)$ is odd in ω. For our purposes, we use a discretization over ω for a reference value of $\bar{K}$, and store the value of f for each of the ω values. f for a general value of ω is then calculated by interpolation.

3.3.2 Properties of the Keplerian map

The map captures well the dynamics of the full equations of motion; namely, the phase space, shown in figure 3.6(b), is densely covered by chains of stable resonant islands, in between which is a connected chaotic zone. The more physically intuitive semimajor axis a is plotted for the vertical axis instead of Keplerian energy K, where $a = -1/(2K)$. The kick function obtained from the map shows that the biggest kicks are recieved for a very narrow range of periapse angle values. If the periapse occurs slightly ahead of the perturber, the spacecraft gets a negative a kick, and if the periapse is slightly behind the perturber, the kick is positive. In figure 3.6(a), these regions are labelled A_- and A_+ respectively.

Using similar methods as above, we can construct an apoapse map for the case when the spacecraft is in the interior realm of the CR3BP, i.e., when its apoapse distance is less than the circular orbit of the perturber. In case of an apoapse map, to recieve the positive a kick, the apoapse needs to be slightly ahead of the perturber (or the periapse needs to be slightly less than π). Similarly, for a negative a kick, the apoapse needs to be slightly behind the perturber (or the periapse needs to be slightly more than $-\pi$). Both the periapse and

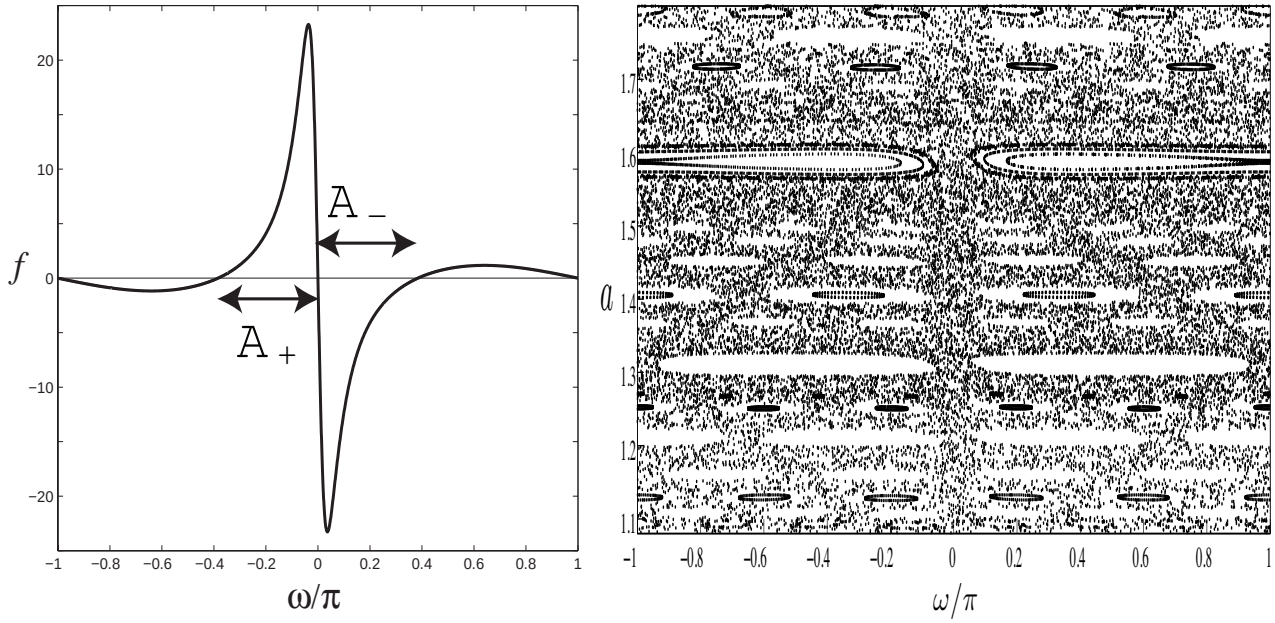

(a) (b)

Figure 3.6: (a) The energy kick function f vs. ω for a typical set of values of the parameters, with the regions of high increase (A_+) and high decrease (A_-) on the ω axis. (b) The connected chaotic sea and the elliptical islands of the Keplerian map. The semimajor axis a vs. the angle of periapsis ω is shown for parameters $\mu = 5.667 \times 10^{-5}$, $C_J = 2.995$, $\bar{a} = -1/(2\bar{K}) = 1.35$ appropriate for a spacecraft in the Jupiter-Callisto system. Several initial conditions were taken randomly in the phase space, and then iterated for a total of ≈ 15000 times.

apoapse maps will be referred to as Keplerian maps, and context should reveal which is being used.

The engineering application envisioned for the map is to the design of low energy trajectories, specifically between moons in the Jupiter moon system. Multiple gravity assists are a key physical mechanism which could be exploited in future scientific missions [23]. For example, in [1], a trajectory sent from Earth to the Jovian system, just grazing the orbit of the outermost icy moon Callisto, can migrate using little or no fuel from orbits with large apoapses to smaller ones was described. This is shown in figures 3.7(a) & (b) in both the phase space and the inertial configuration space. Also, it was shown in [1] that from orbits

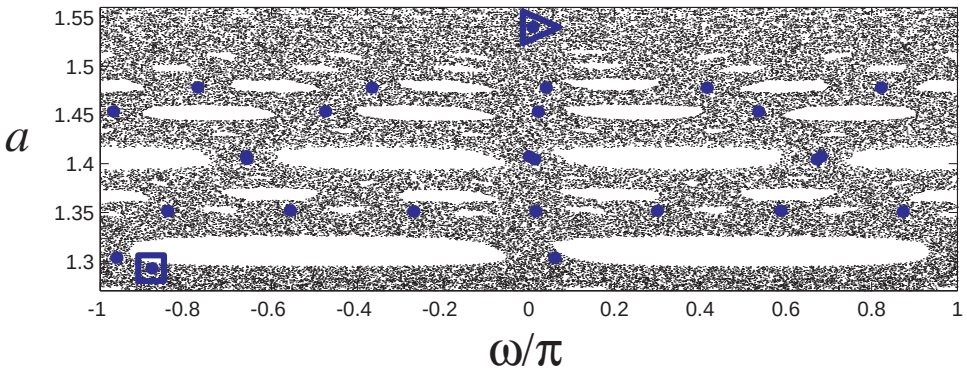

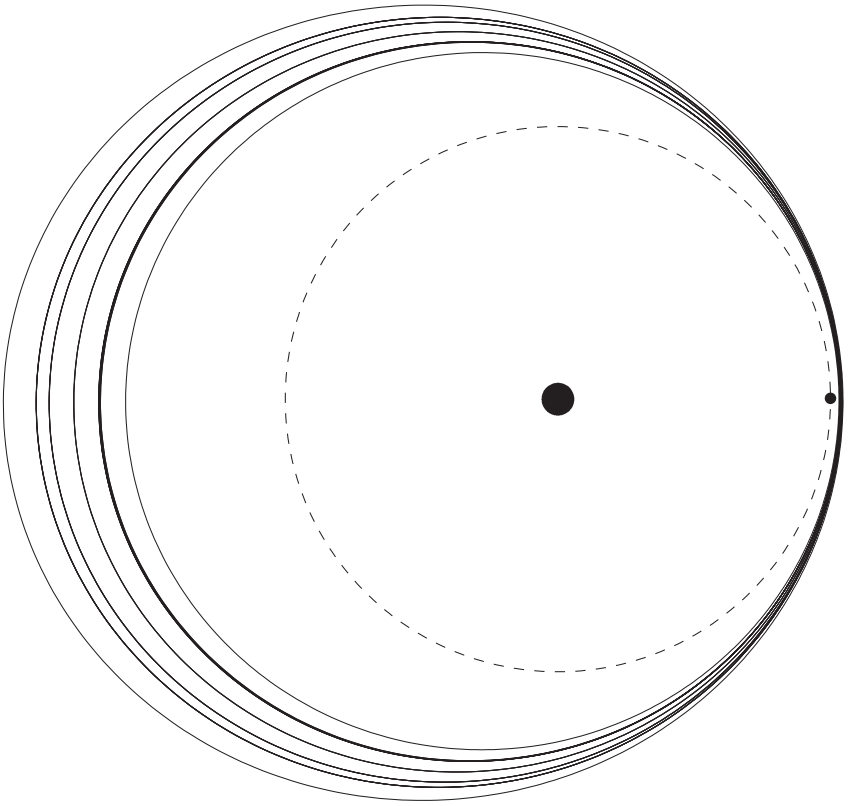

Figure 3.7: This figure shows a trajectory hopping the various resonances which results in rapid decrease in semi-major axis. Top: The trajectory is shown in phase space. The initial point is marked with a triangle, and the final point is marked with a rectangle. Bottom: The trajectory is projected onto the configuration space in an inertial frame. Jupiter and Callisto are shown at their initial positions, and Callisto's orbit is dashed. Note that the periapsis direction remains almost contant during the migration from higher to lower values of semi-major axis takes place. This phenomenon is further explained in section 3.5. This figure has been taken from [1].

slightly larger than Callisto's, the spacecraft can be captured into an orbit around the moon. The set of all capture orbits is a solid cylindrical tube in the phase space, as shown in figure 3.8(a). Followed backward in time this solid tube intersects transversally the Poincaré surface-of-section on which the Keplerian map is defined. The resulting elliptical region, figure 3.8(b), is an *exit* from jovicentric orbits exterior to Callisto. It is the first backward Poincaré cut of the solid tube of capture orbits.

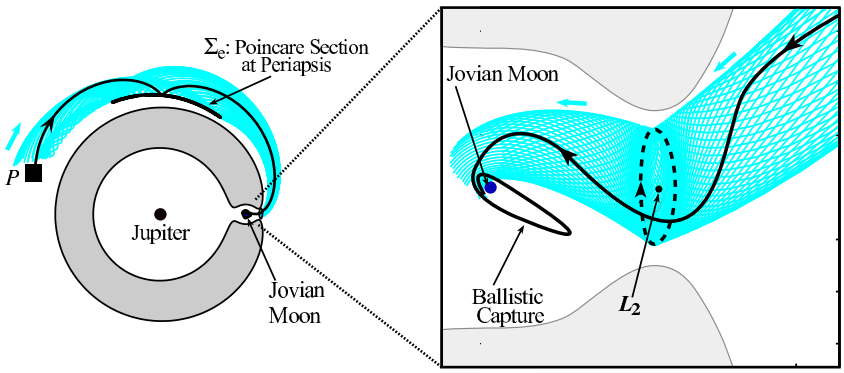

(a)

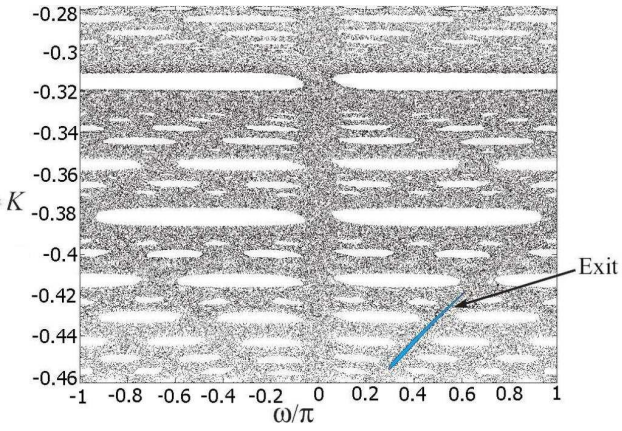

(b)

Figure 3.8: (a) A trajectory of spacecraft P is shown in the configuration space. The spacecraft starts out in the tube whose boundary is the stable invariant manifold of a periodic orbit around L_2. The tube projected onto the configuration space is also shown. We also show the final intersection of the tube with Σ_e, a Poincaré map at periapsis in the exterior realm. (b) The numerically computed location of the same exit on Σ_e, along with the rest of the structure on the phase space of the map. The Spacecraft which reaches the exit will subsequently enter the phase space realm around the perturbing moon. This figure has been taken from [1].

The advantage of considering an analytical two-dimensional map as opposed to full numerical integration of the restricted three-body equations of motion is that we can apply all the theoretical and computational machinery applicable to phase space transport in symplectic twist maps [5]. For example, previous work on twist maps can be applied, revealing the existence of lanes of fast migration between orbits of different semimajor axes. These lanes can be used by a spacecraft sent from Earth to the Jovian system. A spacecraft whose trajectory just grazes the orbit of the outermost icy moon Callisto can migrate using little or no fuel from orbits with large apoapses to smaller ones.

This Keplerian map is an approximate update map for the planar CR3BP; the approximation arises from fact that the kick function f is obtained by evaluating integrals while assuming an average value of K, i.e., $\bar{K}$. An exact map can be obtained, but adds complication. A first attempt to derive an exact map was made by using the actual value K instead of an average value, and mimicking the original procedure, i.e., integrating the perturbation terms over an unperturbed orbit. But this resulted in additional derivative terms, and the resulting map did not turn out to be area-preserving, a key property of the Poincaré map resulting from the full equations of motion which our map (3.34) has.

A second, more complicated way of deriving an exact map is to use the method of Hamilton-Jacobi, which has been developed for general Hamiltonian systems in [34]. The exact map derived this way, though interesting, does not have the simplicity we seek for mission design purposes. This map is discussed next.

3.4 Exact periapse map via Hamilton-Jacobi theory

The derivation of an exact periapse map is described in this section. We generalize the method described in [34] to two degree of freedom systems and apply it to the PCR3BP. This method involves a canonical change of variables, leading to the elimination of perturbation in the time interval between two consecutive intersections with the Poincaré section. This

procedure transforms the perturbed system into an integrable one for the interval between two periapses, and the evolution of transformed variables is then performed. The procedure involves an inverse canonical change of variables at the end of the period. The change of variables is given by generating functions which satisfy the Hamilton-Jacobi equations, and can be solved to arbitrary orders of μ by perturbation theory for finite time intervals. An exact map is derived below using this technique, but we do not get a simple analytical expression for the map, as we do in eq. (3.34).

3.4.1 Review of Hamilton-Jacobi principle and action-angle variables

In a n-degree of freedom Hamiltonian system, let (q, p) be the canonical variables, where $(q, p) \in \Re^n \times \Re^n$, with $H = H(q, p, t)$. The governing equations of motion are given by the canonical Hamilton's equations:

$$\frac{dq}{dt} = \frac{\partial H}{\partial p} \tag{3.36}$$

$$\frac{dp}{dt} = -\frac{\partial H}{\partial q} \tag{3.37}$$

Consider a change of variables from (q, p) to (Q, P), where $Q = Q(q, p)$ and $P = P(q, p)$, with the new Hamiltonian being $\hat{H}(Q, P, t)$. If the transformation preserves the canonical structure, the new equations of motion will be given by:

$$\frac{dQ}{dt} = \frac{\partial \hat{H}}{\partial P} \tag{3.38}$$

$$\frac{dP}{dt} = -\frac{\partial \hat{H}}{\partial Q} \tag{3.39}$$

The generating function that we consider for our problem will of the form $S = S(q, P)$, i.e., its a function of the old coordinates and new momenta. The other variables can be obtained

by the following relations:

$$p = \frac{\partial S(q, P, t)}{\partial q} \tag{3.40}$$

$$Q = \frac{\partial S(q, P, t)}{\partial P} \tag{3.41}$$

Since we want integrability during the interval, we put $\hat{H} = H\hat{(}P)$ only. Clearly, we can see that the evolution of transformed coordinates and momenta is given by :

$$\begin{aligned} Q &= Q_0 + \Omega(P)(t - t_0) \\ P &= P_0 \end{aligned} \tag{3.42}$$

where $\Omega = \dfrac{\partial \hat{H}(P)}{\partial P}$ is the oscillation frequency in the transformed variables. The generating function satisfies the Hamilton-Jacobi equation :

$$H\left(q, \frac{\partial S(q, P, t)}{\partial q}, t\right) + \frac{\partial S}{\partial t} = \hat{H}(P) \tag{3.43}$$

Hence, the time evolution of system is completely determined by the generating function $S(q, P, t)$.

Two different ways of finding the periapse mapping are presented below. The first one is an approximate map in the sense that will be made clear below, and the second one is 'exact' up to order μ.

3.4.2 Method 1

We write the Hamiltonian for the PCR3BP in Delaunay variables as follows:

$$H(l, g, L, G) = H_0(L, G) + \mu H_p \tag{3.44}$$

$$\tag{3.45}$$

where

$$H_0 = -\frac{1}{2L^2} - G \tag{3.46}$$

$$H_p = \frac{1}{r} + \frac{cos(\theta)}{r^2} - \frac{1}{\sqrt{r^2 + 1 - 2rcos(\theta)}} \tag{3.47}$$

$$r = \frac{a(1-e^2)}{1 + ecos(\nu)} \tag{3.48}$$

$$\theta = g + \nu \tag{3.49}$$

$$l = \sqrt{(}a) \tag{3.50}$$

Note here we use g to denote the angle of periapse in the rotating frame, instead of $\bar{\omega}$ used earlier. This is done to be consistent with the literature on Hamilton-Jacobi related computations involving the PCR3BP Delaunay variables.

Let the transformation be from (l, g, L, G) to $(\theta_l, \theta_g, J_l, J_g)$. For an unperturbed system, i.e., $\mu = 0$, we can clearly write the generating function as follows:

$$S_0(l, g, J_l, J_g) = lJ_l + gJ_g - H_0(J_l, J_g)t + \hat{H}(J_l, J_g, t)t \tag{3.51}$$

Note that the above generating function satisfies all the equations given in the previous section. This suggests that for $0 < \mu \ll 1$,we can write the generating function as :

$$S(l, g, J_l, J_g, t) = S_0(l, g, J_l, J_g) + \mu S_1(l, g, J_l, J_g, t; \mu); \tag{3.52}$$

From the generating function, we can do the transformation for momenta at time step k, as done in previous section:

$$\begin{aligned} J_l^k &= L^k - \mu \frac{\partial S_1(l^k, g^k, J_l^k, J_g^k, t^k)}{\partial l} \\ J_g^k &= G^k - \mu \frac{\partial S_1(l^k, g^k, J_l^k, J_g^k, t^k)}{\partial g} \end{aligned} \tag{3.53}$$

Note that the above two equations are implicit in J_l^k and J_g^k. Once we get the transformed momenta J_l^k, J_g^k, we know that these will be constant throughout the interval of interest. To

get the actual momenta at the next time step, we write the equations similar to the above two equations, but now at $t = t^{k+1}$. So we get,

$$\begin{aligned} L^{k+1} &= J_l^{k+1} + \mu \frac{\partial S_1(l^{k+1}, g^{k+1}, J_l^k, J_g^k, t^{k+1})}{\partial l} \\ G^{k+1} &= J_g^{k+1} + \mu \frac{\partial S_1(l^{k+1}, g^{k+1}, J_l^k, J_g^k, t^{k+1})}{\partial g} \end{aligned} \tag{3.54}$$

We observe that to solve the for L^{k+1} and G^{k+1}, we need the original coordinates l and g at $t = t^{k+1}$. Again from the generating function, we write equation relating actual and transformed coordinates:

$$\theta_l^k = l^k + (\Omega_l(J_l^k, J_g^k) - w_l(J_l^k, J_g^k))t^k + \mu \frac{\partial S_1(l^k, g^k, J_l^k, J_g^k, t^k)}{\partial J_l^k} \tag{3.55}$$

$$\theta_g^k = g^k + (\Omega_g(J_l^k, J_g^k) - w_g(J_l^k, J_g^k))t^k + \mu \frac{\partial S_1(l^k, g^k, J_l^k, J_g^k, t^k)}{\partial J_g^k} \tag{3.56}$$

$$\theta_l^{k+1} = l^{k+1} + (\Omega_l(J_l^k, J_g^k) - w_l(J_l^k, J_g^k))t^{k+1} + \mu \frac{\partial S_1(l^{k+1}, g^{k+1}, J_l^k, J_g^k, t^{k+1})}{\partial J_l^k} \tag{3.57}$$

$$\theta_g^{k+1} = g^{k+1} + (\Omega_g(J_l^k, J_g^k) - w_g(J_l^k, J_g^k))t^{k+1} + \mu \frac{\partial S_1(l^{k+1}, g^{k+1}, J_l^k, J_g^k, t^{k+1})}{\partial J_g^k} \tag{3.58}$$

Here, w_l and w_g are the frequencies of the unperturbed system in terms of transformed momenta, given by $\frac{1}{J_l^3}$ and -1 respectively. The evolution of these transformed coordinates is given by equations similar to equation (3.42), i.e., they are linear in time. The evolution equations are as follows:

$$\theta_l^{k+1} = \theta_l^k + (t^{k+1} - t^k)\Omega_l(J_l^k, J_g^k) \tag{3.59}$$

$$\theta_g^{k+1} = \theta_g^k + (t^{k+1} - t^k)\Omega_g(J_l^k, J_g^k) \tag{3.60}$$

Substituting the above 2 eqns in the eqtions (3.55) through (3.58) and re-arranging, we get the following relations for the evolution of original coordinates:

$$\begin{aligned} l^{k+1} &= l^k + w_l(t^{k+1} - t^k) + \mu \frac{\partial S_1(l^k, g^k, J_l^k, J_g^k, t^k)}{\partial J_l^k} - \mu \frac{\partial S_1(l^{k+1}, g^{k+1}, J_l^k, J_g^k, t^{k+1})}{\partial J_l^k} \\ g^{k+1} &= g^k + w_g(t^{k+1} - t^k) + \mu \frac{\partial S_1(l^k, g^k, J_l^k, J_g^k, t^k)}{\partial J_g^k} - \mu \frac{\partial S_1(l^{k+1}, g^{k+1}, J_l^k, J_g^k, t^{k+1})}{\partial J_g^k} \end{aligned} \tag{3.61}$$

So the equations (3.53) , (3.54), and (3.61) are the three sets of coupled nonlinear equations that describe the evolution of the system. The remaining task is to find the perturbed part of the generating function , i.e., S_1. To do so, we will follow the perturbation method. The Hamilton-Jacobi equation for this system is as follows:

$$H_0\left(\frac{\partial S}{\partial l}, \frac{\partial S}{\partial g}\right) + \mu H_p\left(l, g, \frac{\partial S}{\partial l}, \frac{\partial S}{\partial g}, t\right) + \frac{\partial S}{\partial t} = \hat{H}(J_l, J_g) \tag{3.62}$$

We write $\hat{H}(J_l, J_g) = \hat{H}_0(J_l, J_g) + \mu\hat{H}_1(J_l, J_g)$, and substitute R.H.S of equation (3.51) for S in the above equation. Using Taylor series expansions, and comparing coefficients of μ on both sides, we get the following :

$$\frac{\partial S_1(l, g, J_l, J_g, t)}{\partial t} + w_l\frac{\partial S_1(l, g, J_l, J_g, t)}{\partial l} + w_g\frac{\partial S_1(l, g, J_l, J_g, t)}{\partial g} = \hat{H}_1(J_l, J_g) - H_p(l, g, J_l, J_g) \tag{3.63}$$

Remark: We have used the fact that $w_l = \frac{\partial H_0}{\partial J_l}$ and $w_g = \frac{\partial H_0}{\partial J_g}$. To integrate the above equation, we observe that on an unperturbed orbit, the L.H.S reduces to the total derivative of S_1. The unperturbed orbit for l, g can be written as :

$$l(t) = l_0 + w_l(J_l, J_g)(t - t_0) \tag{3.64}$$

$$g(t) = g_0 + w_g(J_l, J_g)(t - t_0) \tag{3.65}$$

So the equation for S_1 reduces to :

$$S_1(l, g, J_g, J_t) = -\hat{H}_1(t - t_0) - \int_{t_0}^{t} H_1(l(t'), g(t'), J_g, J_l)dt' \tag{3.66}$$

$$l(t') = l + w_l(J_l, J_g)(t - t') \tag{3.67}$$

$$g(t') = l + w_g(J_l, J_g)(t - t') \tag{3.68}$$

In the above equation, we need to choose the value of t_0, lying between t^k and t^{k+1}. Following [34], we take it to be the mid-point of the two times. We also need to address the issue

of not knowing the exact time of the next periapse. To use the above formulation as it is, we assume that the time taken is given by $\Delta t = 2\pi/w_l(J_l, J_g)$. Note that this is an approximation, because it actually gives us the time that would be spent on an unperturbed orbit (in transformed coordinates). To integrate, we use a change of variables, as follows:

$$l = l(t') \tag{3.69}$$

$$dt' = \frac{dl}{w_l(J_l, J_g)} \tag{3.70}$$

$$g(l) = g(t') + \frac{w_g(J_l, J_g)(l - l(t))}{w_l(J_g, J_l)} \tag{3.71}$$

$$\tag{3.72}$$

This results in the the following expression for S_1

$$S_1(l(t), g(t), J_g, J_t) = -\hat{H}_1(t - t_0) - \int_{l(t_0)}^{l(t)} H_1(l, g(l), J_g, J_l)dl \tag{3.73}$$

$$\tag{3.74}$$

The above expression, can be integrated numerically, for $t = t^k$ and $t = t^{k+1}$, putting $l(t_0) = l(t^k) + \pi$ and $l(t_0) = l(t^{k+1}) - \pi$, respectively. Note that the transformed momenta are constant within the interval.

3.4.3 Method 2: Using the extended Hamiltonian formulation for obtaining exact mapping

We derive an extended formulation for the system to avoid approximating the time of integration. We take time t as a system coordinate, which in the rotating frame turns out to be a cyclic variable, with the conjugate momenta h being the negative of the original Hamiltonian. We take the mean anomaly, l as the new independent variable instead, and formulate the differential equations with respect to the new 'time'. This will lead to an exact formulation because we exactly know the values of this variable at each periapse, i.e., $l = 2n\pi$. In this case, the negative of the conjugate momentum of l, will be the Hamiltonian,

K. So, $K = -L$. The only extra step in this formulation is obtaining K, by inverting the original equation for the Hamiltonian. We have :

$$K = -L \tag{3.75}$$

$$K = K_0(h, G) + \mu K_p(t, l, g, h, G) \tag{3.76}$$

$$-h = -\frac{1}{2L^2} - G + \mu H_p(l, g, L, G) \tag{3.77}$$

For $\mu = 0$, we get:

$$-h + G = -\frac{1}{2L^2} \tag{3.78}$$

$$K_0(h, G) = -\sqrt{\frac{1}{2(h - G)}} \tag{3.79}$$

We can numerically solve (3.77) for L. We get then:

$$K_p = (-K_0)^3 H_p(l, g, L(l, g, h, G), G) \tag{3.80}$$

$$\tag{3.81}$$

Once K is completely known, the problem is reduced to the same as the one discussed in 3.4.2. Here we have (g, t) as coordinates to be updated, and $(G, h = -H)$ as the conjugate momenta. $K = K(g, t, G, h, l)$ becomes the new Hamiltonian, and l is the new 'time'. Numerical results confirm that this formulation is indeed 'exact' and the kick function obtained is virtually indistinguishable from that obtained from direct integration.

3.5 Fuel efficient (near zero fuel) trajectory design

3.5.1 Patched three body approximation

The 'Patched three body approximation' discussed by Ross et al. [23] considers the motion of a spacecraft in the field of n bodies, considered two at a time, e.g., Jupiter and its ith moon, M_i. When the trajectory of a spacecraft comes close to the orbit of M_i, the perturbation of

the spacecraft's motion away from purely Keplerian motion about Jupiter is dominated by M_i. In this situation, we say that the spacecraft's motion is well modeled by the Jupiter-M_i-spacecraft restricted three-body problem. For each segment of purely three body motion, the invariant manifold tubes of L_1 and L_2 bound orbits (including periodic orbits) lead toward or away from temporary capture around a moon. The transport mechanism is associated with the dynamics of homoclinic and heteroclinic tangles, and the study of this dynamics leads to a general formulation of the transport in terms of distributions of small phase space regions called 'lobes' [35]. Within the three-body problem, we can take advantage of phase space structures such as these tubes of capture and escape, as well as lobes associated with movement between orbital resonances. Both tubes and lobes, and the dynamics associated with them, are important for the design of a MMO trajectory. Portions of these tubes are "carried" by the lobes mediating movement between orbital resonances [28]. Directed movement between orbital resonances is what allows a spacecraft to achieve large changes in its orbit [23, 1]. When the spacecraft's motion, as modeled in one three-body system, reaches an orbit whereby it can switch to another three-body system, we switch or "patch" the three-body model to the new system. This initial guess solution is then refined to obtain a trajectory in a more accurate four-body model. Evidence suggests that these initial guesses are very good [23], even in the full n-body model.

3.5.2 Using the patched three body approximation to design fuel efficient trajectories

We describe a methodology to obtain fuel optimal trajectories for the MMO [2], [36] with the help of the Keplerian map. During the inter-moon transfer—where one wants to leave a moon and transfer to another moon, closer in to Jupiter—we consider the transfer in two portions, shown schematically in figure 3.9, with M_2 as the inner moon. In the first portion, the transfer determination problem becomes one of finding an appropriate solution of the Jupiter-M_1-spacecraft problem which jumps between orbital resonances with M_1, i.e.,

performing resonant gravity assists to decrease the perijove [23]. M_1's perturbation is only significant over a small portion of the spacecraft trajectory near apojove (A in figure 3.9(a)). The effect of M_1 is to impart an impulse to the spacecraft, equivalent to a ΔV in the absence of M_1.

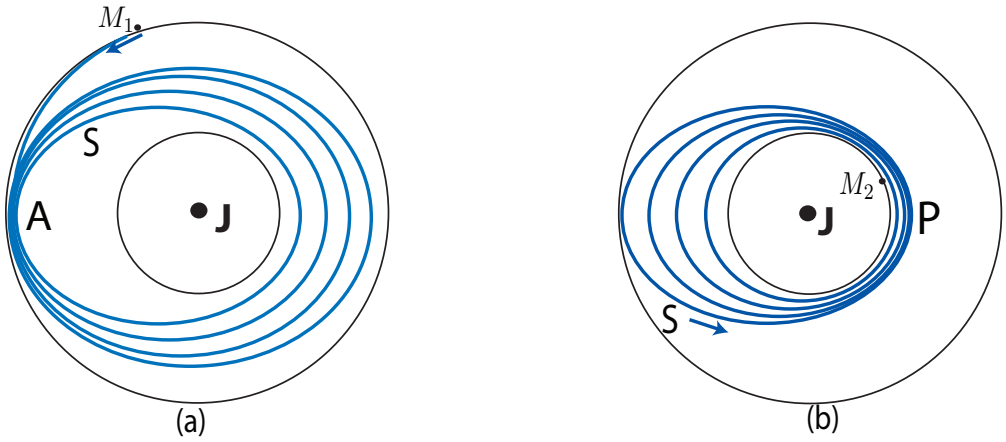

Figure 3.9: Inter-moon transfer via resonant gravity assists. (a) The circular orbits of two moons/perturbers. Once the spacecraft exits the outer moon's (M_1's) sphere-of-influence, it travels in an perturbed (three-body) elliptical orbit about Jupiter. The spacecraft gets a gravity assist from the outer moon when it passes through apojove (denoted A). Note that the several flybys have the same apojove direction because the spacecraft orbit is in near-resonance with the outer moon's orbital period and hence it encounters the moon at about the same point in its orbit each time. Once the spacecraft orbit comes close to grazing the orbit of the inner moon, M_2, the inner moon becomes the dominant perturber. The spacecraft orbit where this occurs is called the switching orbit and is denoted S. (b) The spacecraft now receives gravity assists from M_2 at perijove (P), where the near-resonance condition also applies. The spacecraft is then ballistically captured by M_2.

The perijove is decreased until it has a value close to M_2's orbit, in fact, close to the orbit of M_2's L_2. We can then assume that a gravity assist can be achieved with M_2 with an appropriate geometry such that M_2 becomes the dominant perturber (i.e., the effect of M_1 is now negligible as long as the spacecraft is not pushed towards $M_!$ again) and all subsequent gravity assists will be with M_2 only. When a particular resonance is reached,

the spacecraft can then be ballistically captured by the inner moon [28]. The arc of the spacecraft's trajectory at which the spacecraft's perturbation switches from being dominated by moon M_1 to being dominated by M_2 is called the "switching orbit." A rocket burn maneuver need not be necessary to effect this switch. The set of possible switching orbits is the "switching region" of the P3BA, see figure 3.10 . It is the analogue of the "sphere of influence" concept used in the patched-conic approximation, which guides a mission designer regarding when to switch the central body for the model of the spacecraft's Keplerian motion. A major difference is that the switching region is defined in the phase space and not just in the configuration space.

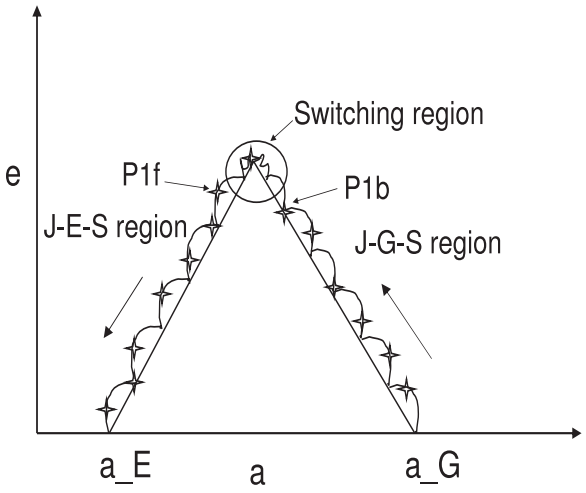

Figure 3.10: Schematic trajectory in a-e plane showing various regions. Various apoapses/periapses are starred. The straight lines represent the constant three body energy contours in J-G-S and J-E-S systems.

The task of searching for trajectories that go from near-Ganymede to near-Europa Jovicentric orbits can be simplified using the Keplerian maps for the two three body systems. Given the size of the periodic orbit around L_1 of Jupiter-Ganymede-Spacecraft (J-G-S) system, we can find its three-body energy . Similarly, given a target periodic orbit around L_2 of the Jupiter-Europa-Spacecraft (J-E-S) system, we can find its three-body energy. The small neighbourhood around the point where J-G-S and J-E-S constant three body energy contour lines intersect for a given set of energies, represents the switching region. Figure 3.10 shows

the various regions. The search for probable trajectories is done as follows:

1). We choose a point outside the switching region, lying on the J-G-S contour line and close to the switching region. Call it $P(=(a_0,e_0))$ and time $t = 0$. Without loss of generality, we assume the spacecraft is currently at (or close to) apojove. To uniquely define a trajectory in the four body system, we need to specify the periapse angle w.r.t the Jupiter-Ganymede line, ω_g and with respect to the Jupiter-Europa line, ω_e at time t=0.

2). We want to choose the periapse angle with respect to J-G line so that the spacecraft get a significant kick from Ganymede towards Europa, and ends up in the switching region. Recall from the previous section that this implies the apoapse should occur with the periapse slightly more than $-\pi$ with respect to J-G line. We can narrow down the search space for ω_g at $t = 0$ to those values, i.e., $-.90\pi < \omega_g < -.99\pi$.

3). The primary interaction with Europa occurs at periapse. Ideally, once the spacecraft gets the previously mentioned kick from Ganymede, we want it to get a further kick from Europa, towards Europa, at the following periapse. Again recall that this implies the next periapse should occur with periapse sligthly greater than zero with respect to J-E line. If we use only the planar CR3BP equations for J-G-S system (i.e., put mass of Europa to zero in the 4-body equations), starting with time $t = 0$, ω_g selected from the above search space, and ω_e with an initial guess, we can find the periapse angle ω_e at the next periapse. Using predictor-corrector sensitivity analysis, we can refine the initial guess for ω_e at $t = 0$, so that the spacecraft gets a significant kick in the next periapse. Once we have a range of values of ω_e at $t = 0$ that give the desired phase for the next few periapses, we can use full 4-body equations to determine the actual trajectory in the switching region. The narrowed down search space for ω_e and ω_g is labelled S_ω. Recall that the path of the spacecraft in this region is called the "switching orbit". The first forward iterate at periapse into the J-E-S region is labelled as $P1_f$ and the first back iterate at apoapse into the J-G-S region is labelled as $P1_b$. Note that if in step 1, the point is chosen exactly at apoapse, then $P1_b = P$.

4). We need to search for the conditions from the set S_ω that will lead to a successive decrease

in the semi-major axis when iterated forward, and will lead to increase in the semi-major axis value when iterated back, outside the switching region. This task of iterating in the J-E-S and J-G-S regions, can be efficiently handled by the Keplerian maps. For each 2-tuple (ω_g,ω_e) and a point $P(a_0,e_0)$ in the switching region, we iterate forward the corresponding point $P1_f$ using the periapse map which is valid only in the J-E-S region, and iterate backward the corresponding point $P1_b$ using the apoapse map, which is valid only in the J-G-S region.

5). Once we have found which values among the set S_ω will result in an Jovicentric orbit from near-Ganymede to near-Europa using the separate Keplerian maps, we use the full four-body equations to get actual trajectories. In some cases, since the maps are not exact, the trajectories and transfer times obtained by full 4-body equations differ significantly from those obtained from the maps. But, we do get a number of topologically different trajectories by using maps, that are verified by full 4-body equations. We can also cycle through various nearby (a, e) values in the switching region to get appropriate trajectories.

We show an actual trajectory for the four body system found out using the method described above in figure 3.11. Figure 3.11(a) shows the semi-major axis time history, starting from exit from Ganymede to capture by Europa. Figure 3.11(b) shows the time history in an a-e plot, clearly showing that the spacecraft closely follows constant energy contours in the two regimes. Figures 3.11(c) and 3.11(d) show the three-body energy history of the spacecraft for Jupiter-Ganymede-Spacecraft and Jupiter-Europa-Spacecraft systems respectively. The two solutions were patched together and the switching region, where the switching of dominant perturber occurs in the actual four body trajectory, is marked. Clearly, the three-body energy for J-G-S system is constant before the switching region and energy for the J-E-S system is almost constant after the switching region. This separation of domains of influence of the two perturbers suggests that the patched three body approach can be used to obtain good initial guesses for the actual trajectory, which can in turn be obtained by using the four body equations. Hence, we can use 2 separate Keplerian maps and patch the solutions appropriately to get initial guesses.

The trajectory shown in figure 3.11 has a very long transfer time between the two moons, arising primarily due to the spacecraft getting stuck in a resonance for a very long time. To overcome this problem and to design fuel efficient trajectories with realistic transfer times, we introduce the controlled Keplerian map in next section.

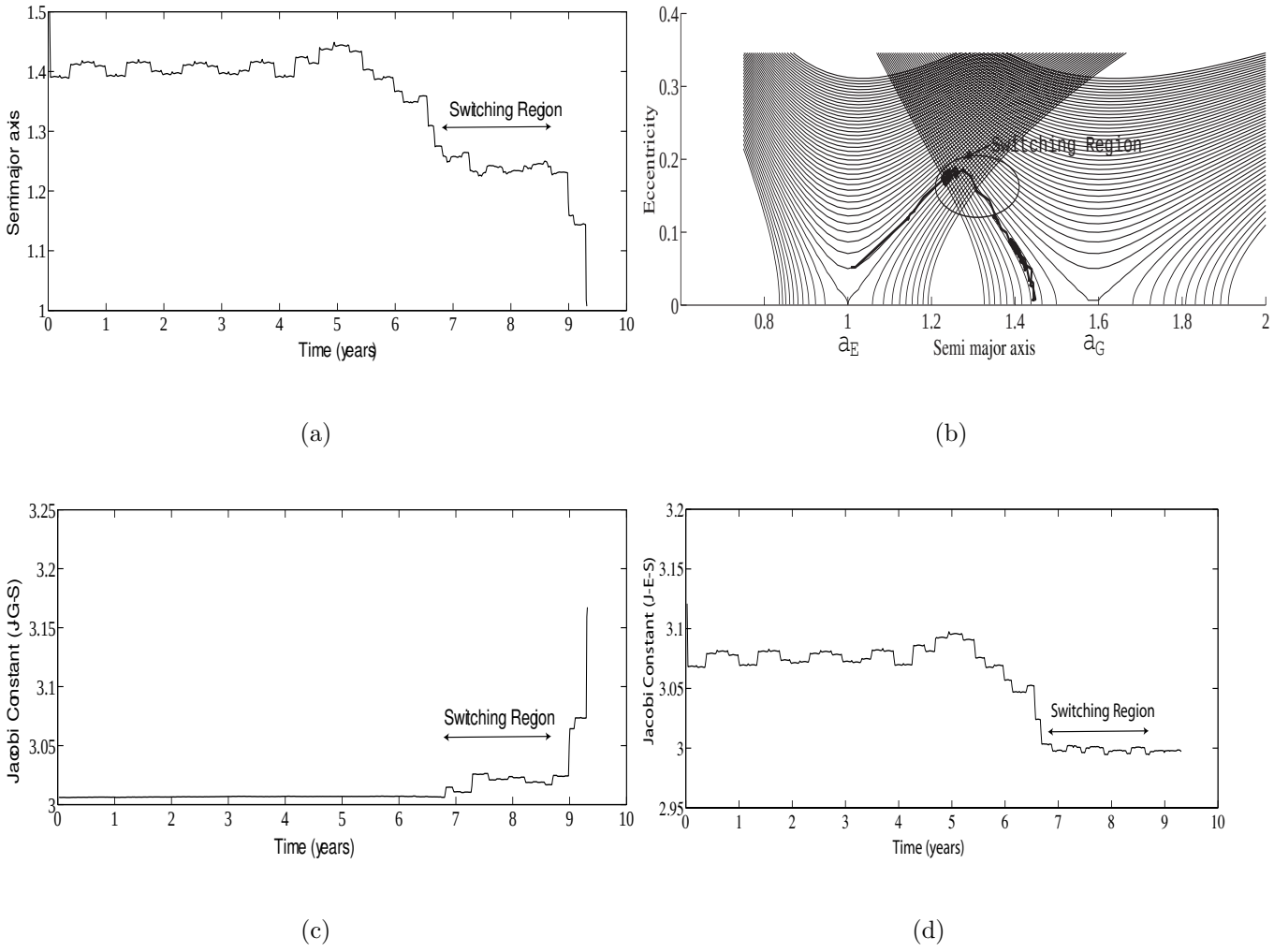

Figure 3.11: Trajectory found using the Patched Three Body Approximation. a). Semi-major axis time history b). Trajectory in 'a-e' plane. c) Jacobi Constant for J-G-S system d). Jacobi Constant for J-E-S system. The trajectory was obtained by integrating the full 4-body system.

3.6 A method for designing trajectories using a controlled map

3.6.1 Controlled Keplerian Map

The controlled Keplerian map [2] with a control u is an update map for the angle of periapse (or apoapse) ω in the rotating frame and Keplerian energy K, $F : \mathcal{A} \times U \to \mathcal{A}$

$$F\left(\begin{pmatrix} \omega_n \\ K_n \end{pmatrix}, u_n\right) = \begin{pmatrix} \omega_{n+1} \\ K_{n+1} \end{pmatrix} = \begin{pmatrix} \omega_n - 2\pi(-2(K_n + \mu f(\omega_n) + \alpha u_n))^{-3/2} \\ K_n + \mu f(\omega_n) + \alpha u_n \end{pmatrix} \quad (3.82)$$

where $u_n \in U = [-u_{\max}, u_{\max}]$, $u_{\max} \ll 1$. The term $\alpha = \alpha(C_J, \bar{K})$ is approximated as constant such that:

$$\alpha(C_J, \bar{K}) = \sqrt{\frac{1}{\bar{a}} \frac{(1+\bar{e})}{(1-\bar{e})}}$$
$$\bar{a} = -\frac{1}{2\bar{K}}$$
$$\bar{e} = \sqrt{1 - \left(\frac{C_J - \bar{a}}{2\bar{a}^{3/2}}\right)^2}$$

The control is modeled as a kick at periapse, which increases the speed by u_n and the Keplerian energy K by αu_n. The control strategy employed to get desired trajectories is two-fold: it involves a coarse control part where the aim is to get rapid decrease in the semi-major axis value of the spacecraft, and a fine control part, where we target specific regions of interest in the phase space. The reason for this two-pronged strategy is that the traditional forward-backward approach [37] works best only if there are no big resonances in between the starting point and the target region. If the source and target regions lie in two distant regions separated by slow transport barriers, then the time before an intersection takes place in this approach is very large. During that time, the extensions of both the image of source segment and preimage of target segment grow exponentially in size, which requires exponentially increasing number of discrete points to resolve them. As was mentioned earlier,

and is evident from figure 3.6(b), the phase space for our problem is populated with big resonances resulting in a mixed phase space, and hence, the forward-backward approach alone would not be sufficient for our purposes.

3.6.2 Coarse control algorithm

The coarse control algorithm is based on the fact that large changes in semi-major axis (i.e., the action) occur for a very small range of values of the periapse angle (i.e., the angle), see figure 3.6a. We adopt the policy of 'going with the flow', until we approach a region where there is going to be large change in the semi-major axis. The outline of the algorithm for a single three body system is as follows:

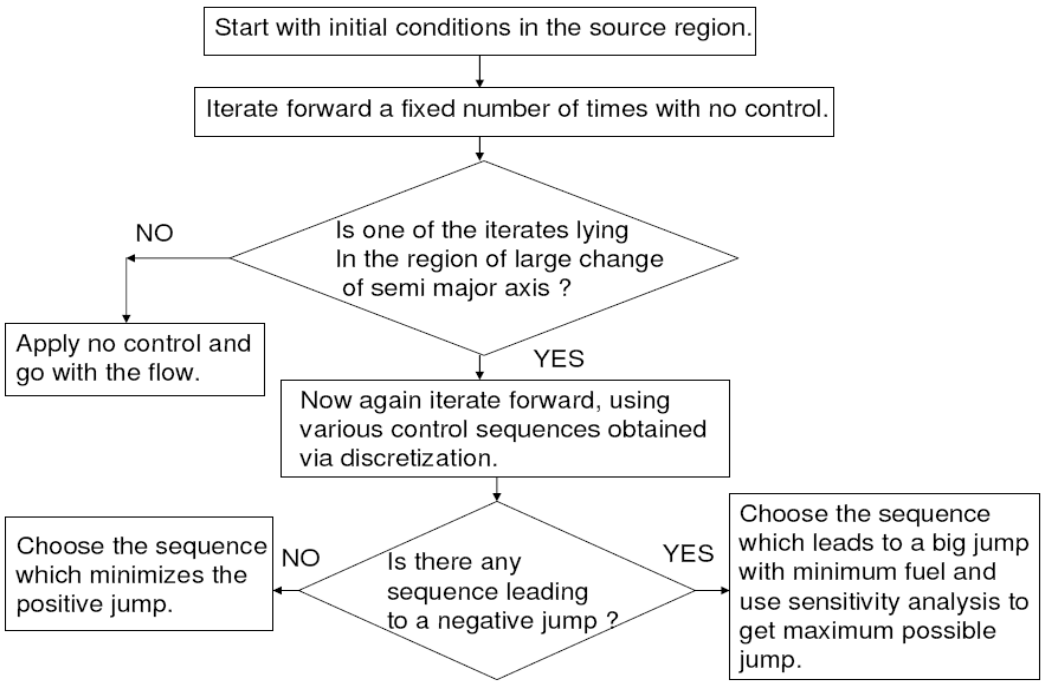

Figure 3.12: The coarse control algorithm

1). At (ω_n, a_n), we iterate forward n_{max} steps with $u = 0$, where n_{max} holds an inverse

relationship with u_{max}. If any of the calculated iterates lies with the region of high increase, labelled A_+ or the region of high decrease, labelled A_-, we calculate the control (2a and 2b, respectively, see below). Else, we do not employ any control at the current iteration step (i.e, $u_n = 0$). The size of both these regions(i.e A_- and A_+) is directly proportional to the parameter $\delta\omega$, i.e. a higher value of $\delta\omega$ implies that control is used for a bigger range of ω values, on either side of $\omega = 0$ line.

2a). Ideally, if one of the future iterates calculated above is in A_+, we want to apply control so as to move the iterate away from it to the neighboring A_- region. If the ith iterate (where $i < n_{max}$) is in A_+, we calculate a control sequence over the next i iterates. The control domain (i.e., $[-u, u] \times [-u, u] \times ...i$ times) is coarsely discretized and we obtain the iterates using each control sequence resulting from the discretization. Computations were done using a discretization equilavent to ΔV of 1 m/s, and u_{max} was taken as equivalent to ΔV of 5 m/s, in either direction. If there are some sequences that result in the final iterate being in A_-, we choose the sequence which results in the final iterate being in a small neighborhood of ω_{opt}. Here ω_{opt} is the value of ω which leads to the maximum decrease in semi-major axis over one iteration. Then, using sensitivity analysis with respect to the control at the last non-zero iterate in the chosen control sequence, we can adjust its value so that the resultant $\omega \approx \omega_{opt}$, and hence get the maximum possible kick in the desired direction.

On the other hand, if there is no such sequence that results in the final iterate being in A_-, we need to move the final periapse angle in the other direction so as to minimize the increase in a. This local optimization can be handled by a similar discretization procedure as above.

2b). If one of the future iterates is in A_-, we again use the aforementioned discretization of the control domain, and choose the control sequence in the same way as before. Sensitivity analysis is used to get final $\omega \approx \omega_{opt}$.

3). Once a threshold value of a is reached, we switch to fine-control. Fine control can be handled by forward-backward method, where the target is the interior of the first intersection of the stable invariant manifold of a periodic orbit around L_2 with the Poincaré section at

periapse.

In figure 3.13 we show a sample trajectory obtained by the above mentioned algorithm, for the Jupiter-Europa-Spacecraft system. Note that as a result of appropriately timed control inputs, the spacecraft visits the region of high decrease of semi-major axis.

We can use this algorithm within the framework of patched three body approximation. We use the controlled apoapse map to get the trajectory from near Ganymede to the switching region, and then patch it with another trajectory obtained by using controlled periapse map to get it near Europa (then we can get it captured by Europa by using the forward-backward fine control). A sample trajectory for such a case is shown in figure 3.14. The spacecraft completes this trajectory using 160 m/s of fuel in 1.7 years, which included 116 revolutions around Jupiter (periapse/apoapse passages). The time taken for this mission is less than 10% of that taken for the previously shown optimal (zero) fuel trajectory for the same four body system. Also, this framework is an improvement over the methods that involve large ΔVs [38] and is a more complete method of designing trajectories in a four-body system than using variants of the traditional patched conics approach [39].

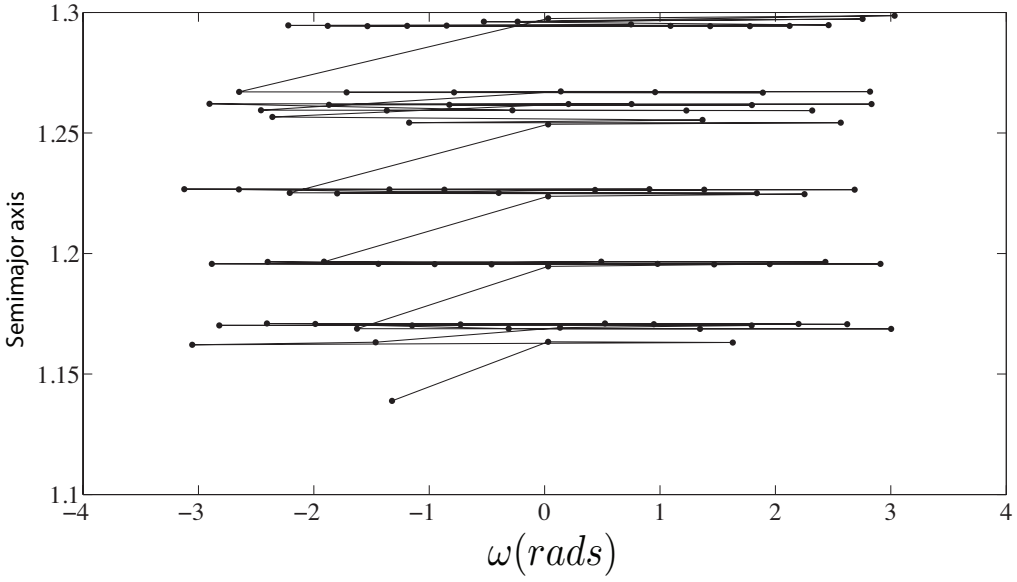

(a)

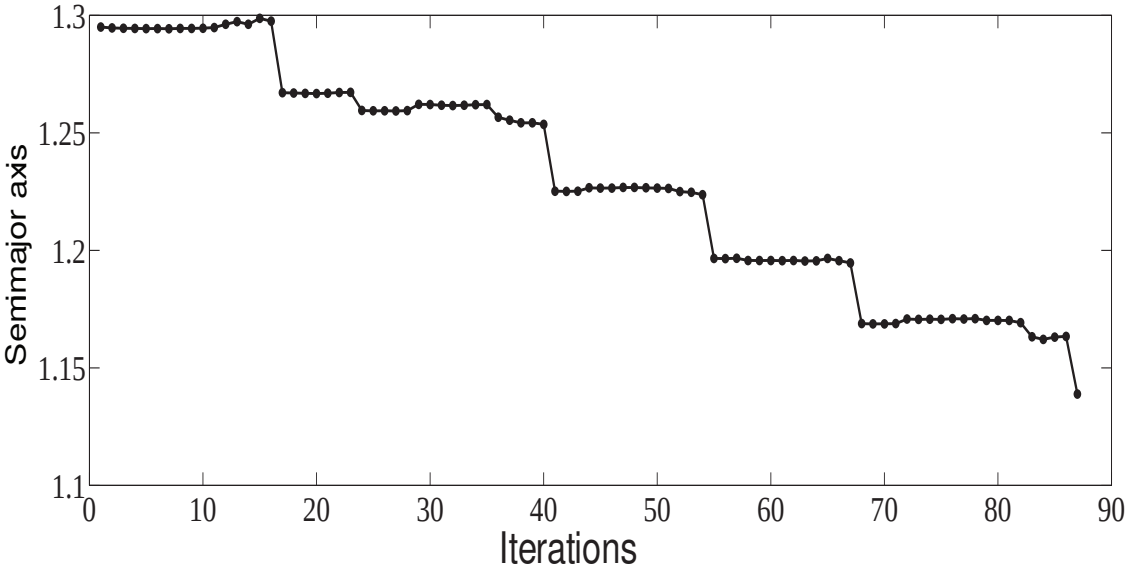

(b)

Figure 3.13: Sample trajectory designed using the algorithm. (a) Plot of Semi-major axis vs. periapse angle. (b) Time history of semi-major axis. The spacecraft repeatedly visits the region of large decrease in semi-major axis.

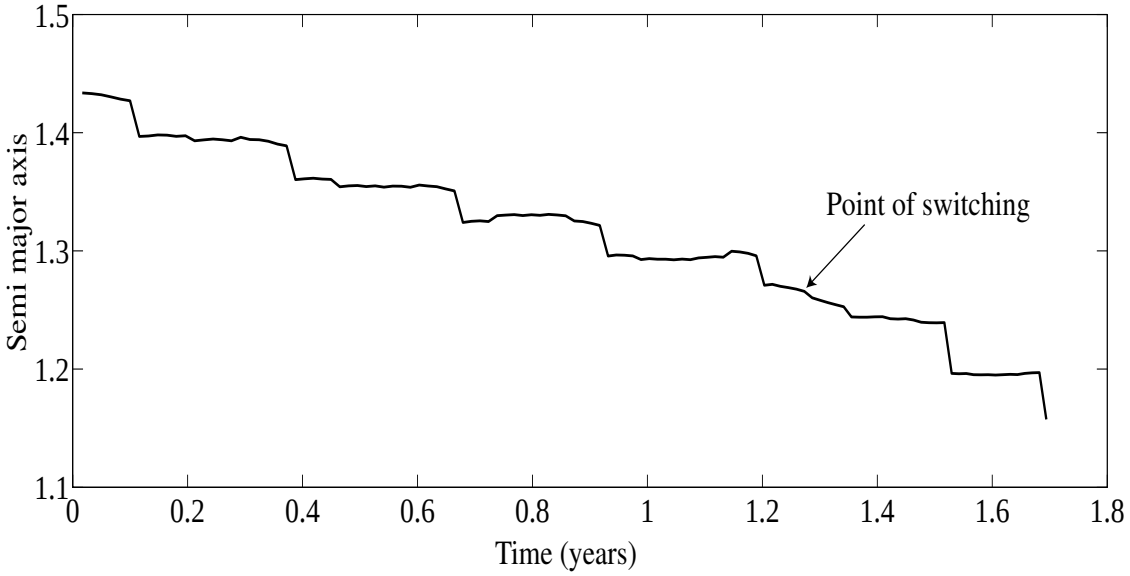

(a)

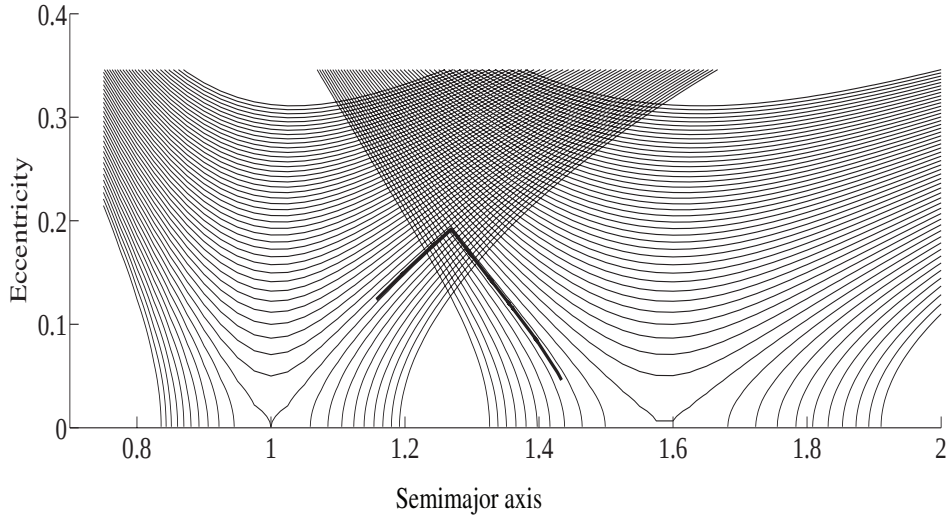

(b)

Figure 3.14: Trajectory for the Jupiter-Europa-Ganymede system using patched three body approach. (a) Time history of semi-major axis. b). Semi-major axis vs. eccentricity plot with three-body energy contours lines in the background.

3.6.3 Trade-off Between fuel and time-of-flight, and other issues

We briefly discuss the tradeoff issues between time-of-flight and fuel(control), since such a tradeoff is typically discussed in all low fuel mission design frameworks. The amount of fuel used for providing ΔVs is expected to be proportional to the parameter $\delta\omega$ upto a saturation point, since this parameter decides the size of the region in phase space where the control is actively applied, as discussed previously. More proactive control is also expected to decrease the time-of-flight up to a certain limit. In figure 3.15, we show plots illustrating the time-of-flight vs. fuel tradeoff for a single three body system (Jupiter-Europa-Spacecraft). Several random initial conditions were taken near $a = 1.5$, and we show the plots for two of those conditions, that take the most (upper line) and the least (lower line) amount of iterations to reach the exit region, for three different values of $\delta\omega$. The basic characteristics of this system are expected to be similar for patched three body systems.

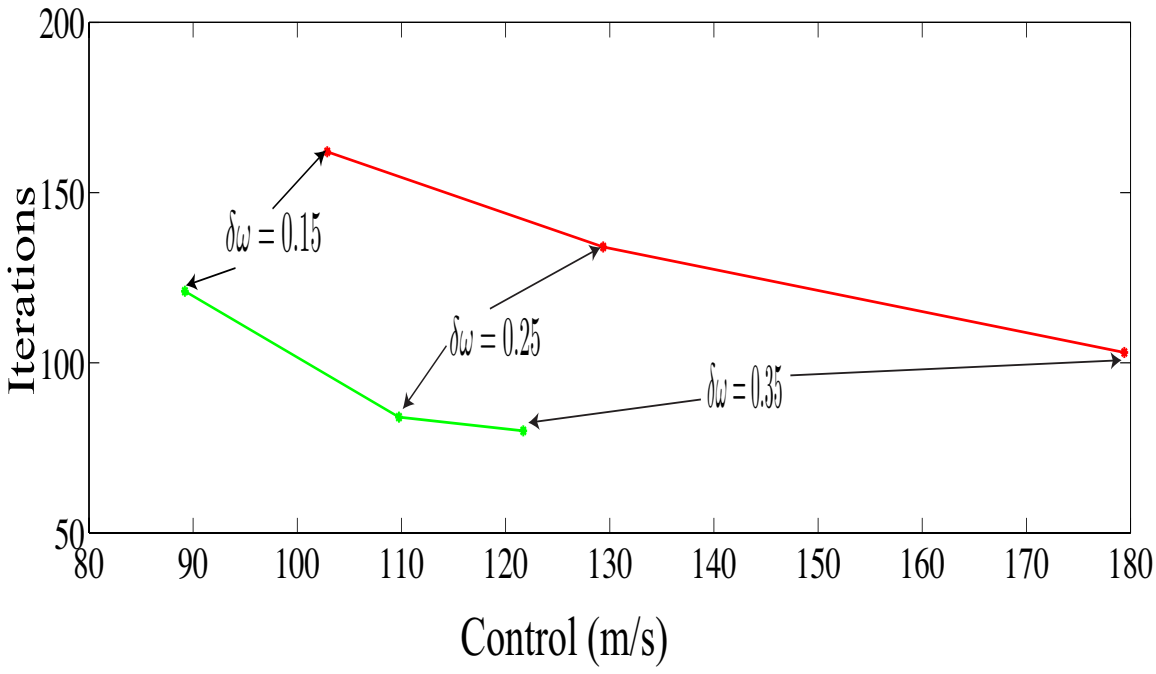

Figure 3.15: Plot showing the tradeoff between control used and number of iterations required for two different intial conditions leading to capture around Europa for the Jupiter-Europa-Spacecraft planar CR3BP

3.7 Conclusion

With the help of a family of analytical two-dimensionalimensional Poincaré maps, exact uncontrolled trajectories in the full equations of motion of the four-body Jupiter-Europa-Ganymede-Spacecraft system were found. The maps were used for fast propagation in regimes where one of the two perturbers is dominant.

Additionally, the maps reduced the patching region search space, i.e., the search for the region where the perturbers have comparable influence, given by critical values of spacecraft phase with respect to the Jupiter-Ganymede and Jupiter-Europa systems. The fast propagation done by the maps on either side of the patching region made preliminary trajectory generation faster than given by integrating the full equations of motion. Many of the trajectories obtained using the algorithm were topologically similar to those finally obtained by full integration (i.e., same number of orbits around Jupiter). The fact that the two three-body energies were almost constant in the actual four-body trajectory on either side of the patching region (a) gives us confidence that there exist actual trajectories that shadow those obtained with the help of the maps and (b) implies a separation of regimes of influence of the perturbers.

The relationship between trajectories found via the maps and trajectories in the full n-body equations of motion needs to be investigated further to make the qualitative analysis given here more applicable to actual implementation for mission design.

Taking note of the apparent validity of the patched three-body approach and utility of the Keplerian maps, we used those Keplerian maps to derive approximate controlled trajectories in the four-body system. Depending upon the chosen value of the parameter of the algorithm, a compromise can be reached between the amount of fuel used and the time taken to complete the mission. We believe that the numbers so obtained should give us a first order estimate of fuel required for actual trajectories in full four-body systems, although this needs to be verified by further investigations.

The use of multiple gravity assists and algorithms such as those mentioned in this paper are stepping stones towards automating the design process of various complicated missions envisioned for the future. This is a significant improvement over the methods that involve large ΔVs and is a more complete method of designing trajectories in a four-body system than using the patched conics approach.

The maps used in both the algorithms are two-dimensionalimensional maps, primarily because the system we considered, the Jupiter-Europa-Ganymede system, is a very nearly coplanar system, and hence, the dynamics involved for a spacecraft restricted to this plane occur in 2 degrees of freedom. This approach can further be extended to model 3 degree of freedom motion, resulting in 4-dimensional maps; the two additional dimensions being inclination i and the longitude of the ascending node Ω. Use of 4-dimensional maps may uncover some exotic trajectories, although the implementation will be difficult since the search space will be larger due to the increase in dimensions.

The algorithm mentioned for finding appropriate control inputs can also be used in any physical modeling problem in which the dynamics are similar to those described by this Keplerian map. The main characteristic of this map is that the kick is significant for only a small range of values of an angle, and hence using appropriate control inputs found out by this algorithm, a particle can be made to have desired large changes in the corresponding action

Chapter 4

Almost Invariant Sets As 'Ghost Rods' In Phase Space Mixing

In collaboration with Mark Stremler and Pankaj Kumar

4.1 Motivation and introduction

Qualitative and quantitative understanding of mixing in phase space is often of great interest while analyzing the dynamics of a complex system. The field of fluid mechanics has proved to be a very productive playground for the understanding of mixing in dynamical systems in general, because of the correspondence between phase space trajectories of Hamiltonian systems and observable fluid (or tracer) particle trajectories for two-dimensional incompressible flows, where the stream-function plays the role of the Hamiltonian of the one degree of freedom system. Dynamical systems theory tells us that while it is impossible for two-dimensional-flows governed by a time-independent Hamiltonian to show chaotic behavior, the systems governed by a time-dependent Hamiltonian can be chaotic under appropriate conditions [15]. The resulting one-and-a-half degree of freedom systems (which in fluid me-

chanics language would correspond to two-dimensional unsteady incompressible flow) can be studied by the use of Poincaré sections, and the resulting two-dimensional maps can be studied by a variety of techniques from the dynamical systems toolbox, such as those mentioned in chapter 2. Meanwhile, the wide variety of experimental techniques available for such fluid systems can further help in motivating and verifying various hypotheses and theoretical results. On the other hand, the application of various dynamical systems techniques has helped gain deeper understanding of dynamics of a wide variety of fluid systems.

Recently, topological methods have been successfully applied towards analyzing mixing in such fluid systems. The basic premise has been to consider the fluid flow as a diffeomorphism on a two-dimensional manifold, and use ideas from Thurston-Nielsen theory (see chapter 2) to obtain lower bounds on the complexity of the flow, by forming a braid composed of (2+1)D (space+time) trajectories of physical stirrers or topological barriers such as fixed points (**'ghost rods'**) of the flow map. In this chapter, we merge statistical and topological approaches, and extend the state-of-the-art in this type of mixing analysis. We argue that the topology of the braid representative of a system can be characterized *more generally* by the almost-invariant-set structure of the flow and hence Thurston-Nielsen theory can still be applied to flows where there are no easily discernible exact periodic orbits (or at least none of low enough period to be of interest). We contend that these almost-invariant-sets are the natural objects on which to pin the Thurston-Nielsen classification theorem (TNCT).

In our example system, we demonstrate that the phase space can be decomposed into two subsets such that there is a very small probability that typical trajectories beginning in each subset will leave this subset in a short time. One of these subsets is a disconnected set of N components, where the N components map one to another. This is the almost-invariant set, and the disconnected components of this set act like N punctures in the original formulation of TNCT. The other subset is its phase space complement. We compute these subsets directly using the eigenvectors of discretized Perron-Frobenius transfer operator via the set-oriented approach, a methodology which has been discussed in some detail in Chapter 2.

We assert that this work marks an important step in making the ghost rod methodology

applicable to realistic fluid flows with arbitrary time-dependence. We also conjecture that this generalization is applicable to a wide variety of dynamical systems, and not just fluid systems.

The chapter is arranged as follows: We give a brief review of the problem of fluid mixing in the next section, focussing on the development of topological techniques in the literature starting with the seminal work of Aref [15]. We then describe the fluid system that we use as a testbed for analysis. In the subsequent section, we go over the results for that system already known in the literature in which a braid is identified by motion of three periodic points in the flow, and the TNCT is applied to obtain a lower bound on the topological entropy of the flow. We then describe the application of the TNCT using an almost-invariant set framework, for a parameter range of the same problem where no discernible periodic points are known to exist.

4.2 Background on fluid mixing

4.2.1 Fluid mixing and chaotic advection

Fluid mixing is an everyday phenomenon. It occurs in nature and in a variety of man-made devices. One of the ways to enhance mixing in a fluid system is to generate turbulence in the flow. However, in the micro and nano scale, due to scaling laws, it is unfeasible to generate turbulence [40]. Thus, the flow is laminar in micro-fluidic systems most of the time and fluid mixing is quite different from that in macro-scale systems. Even in some macro-scale systems, the viscosity of the fluid can be very high and turbulence can also be very difficult to produce.

The theory of chaotic advection [15] has been a fruitful tool for understanding mixing from the geometric point of view. Given an incompressible flow on a two-dimensional domain, we can write the equation of motion for passive fluid particles in terms of derivatives of a

stream-function, $\psi(x, y, t)$.

$$\dot{x} = \frac{\partial \psi(x, y, t)}{\partial y}$$
$$\dot{y} = -\frac{\partial \psi(x, y, t)}{\partial x}$$

As mentioned in the 4.1, $\psi(x, y, t)$ here acts as the Hamiltonian for the dynamical system, and if ψ depends explicitly on time, the resulting flow can be chaotic. The phase space structure that can emerge as a result of a time-dependent Hamiltonian can be quite complicated, and the resulting topological chaos is a major topic of research. There has been a significant amount of interest in understanding how it arises, how to detect it, and how to design for it [41].

One of the methods that has been employed in the literature to study such systems is to compute the Lyapunov exponent or topological entropy by performing brute-force numerical computations to calculate the stretching of non-trivial material lines [16]. Not only is this method resource-intensive, but the results obtained are hardly robust with respect to perturbations in parameters or stochastic perturbations to the system. This approach typically fails to predict how perturbation will impact the chaotic nature of the flow.

The analytical approaches to studying chaos in such systems have been Melnikov-type methods [42],[43] or Kolmogorov-Arnold-Moser (KAM) type methods [44]. The essential idea in this class of techniques for examining chaotic advection is to study chaotic systems which are a result of adding small perturbations to non-chaotic integrable systems. The Melnikov method [45] perturbs the original non-chaotic system with a small excitation, and measures the distance between stable and unstable manifolds of the resulting Poincaré map using a term in the Taylor expansion. While it is one of the few analytical approaches to predicting chaos, it also requires that the original unperturbed trajectory is available in an analytical form, a limitation which severely restricts the use of this method. Moreover, the Melnikov method is useful only when the system is not very far from a non-chaotic state, and hence, cannot be applied to systems which cannot be written in the form of a small perturbation

away from a non-chaotic regime.

4.2.2 Topological approach to fluid mixing by chaotic advection

Topological ideas have been in use for analyzing fluid motion for a long time. Ever since topology was considered an independent field of mathematical study, there have been numerous efforts to apply topological ideas to understand the complex motions that fluid systems are capable of generating. The various topics studied via the topological approach include existence and stability of knotted vortices [46], and motion of vortex rings [47], among other things. See [48] for a historical development of topological ideas in fluid mechanics.

We are mainly concerned with the idea of *topological chaos*, that was first introduced to fluid mechanics in the investigation of the mechanism of stirring in an experimental study [17]. They studied two different periodic motions of three stirrers in viscous fluid flow in a two-dimensional circular domain. The application of the TNCT then led to classification of diffeomorphisms corresponding to different stirring protocols. This classification was used to predict which stirring-protocols will lead to pseudo-Anosov (pA) diffeomorphisms, i.e., the flow in which exponential stretching is experienced in one direction at every point, leading to efficient mixing.

This approach was extended in [49], where the authors showed that physical stirrers are not required for the application of the above framework for classification of the stirring protocols into various TN representatives. It was argued that since topological phase space barriers such as periodic points also 'stir' the fluid by continuity assumptions of the flow, they act like physical stirrers from the topological point of view. The term 'ghost rods' was first used in [50], where the TNCT based topological framework was applied by considering a combination of physical rods and periodic points as the stirrers. It was shown that nonzero topological entropy for certain topologically trivial motions of the physical rod(s) could be accounted for if the braids were formed by considering the trajectories of physical rods and certain periodic points. Further advances in using the concept of periodic orbits as ghost rods

were made in [51] and [52], where the topological approach was applied to design a certain stirrer protocol in two-dimensional and three-dimensional lid-driven cavity flows respectively, consisting solely of periodic points in the flow.
The significance of ghost rods lies in the prediction of chaos based on limited data regarding their motion. In some physical situations, it may be possible to observe ghost rods and from their trajectory topology infer what possible, but unobserved, motions the system can exhibit. For instance, observing only the regular periodic motion of these 'ghost rods' can lead us to infer that the system is chaotic.

In this chapter we use a similar two-dimensional lid-driven cavity flow system and describe how to identify ghost rods and apply the TNCT when periodic orbits no longer exist, or are not readily discernible.

4.3 The lid-driven wide-cavity flow

4.3.1 Designing for chaos: The reference case

The model that we use as the testbed for developing our analysis techniques is described in this section. This model has been described in [53], and is considered here for its simplicity, and the fact that it is amenable to exact solutions. This relatively simple fluid system has an easy to visualize piecewise steady velocity field, but due to this time dependence of the stream function, exhibits complicated dynamics.

Consider the two-dimensional lid-driven cavity flow in an infinitely-wide cavity. If we enforce spatial-periodic boundary conditions on the top and bottom surface, the resulting flow can be viewed as pieces of lid-driven cavity flow with periodic side boundary conditions, and each such piece will represent the whole domain. The vertical boundary between two such pieces is a streamline of the flow, and such boundaries divide the wide cavity into an array

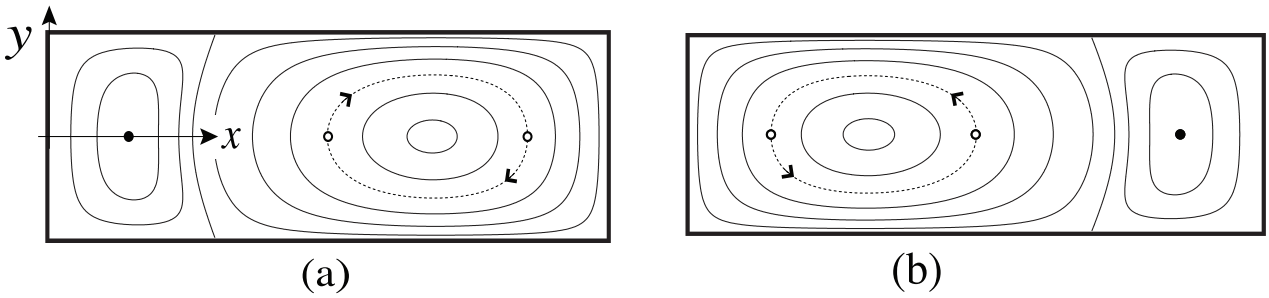

Figure 4.1: Streamlines with both top and bottom walls moving under piecewise uniform velocity: (a) $0 \leq t \leq \tau_f/2$ (b) $\tau_f/2 \leq t \leq \tau_f$. Bottom boundary velocity is mirror image of the top boundary velocity about the horizontal axis.

of rectangles. For Stokes flow in such a two-dimensional rectangular domain

$$M = \{(x, y) : 0 \leq x \leq a, -b \leq y \leq b\}$$

as shown in figure 4.1, the stream function $\psi(x, y)$ satisfies the two-dimensional biharmonic equation

$\nabla^2\nabla^2\psi(x, y) = 0.$

We assume that the tangential velocity on top and bottom boundaries can be expressed as the sum of a series of sinusoidal functions, and for our analysis, we take two terms in such series. Then, the piecewise steady tangential velocity driving the flow on the top boundary is given by

$$V(x) = \begin{cases} U_1 \sin\left(\frac{\pi x}{a}\right) + U_2 \sin\left(\frac{2\pi x}{a}\right) & 0 \leq t \leq \tau_f/2 \\ -U_1 \sin\left(\frac{\pi x}{a}\right) + U_2 \sin\left(\frac{2\pi x}{a}\right) & \tau_f/2 \leq t \leq \tau_f. \end{cases}$$

and corresponding tangential velocity on the bottom boundary is given by $-V(x)$, where τ_f is the normalized period of the periodic boundary conditions (and hence the fluid flow). This symmetry in the boundary conditions implies that the flow pattern is reflected about the line $x = a/2$ every $\tau_f/2$ units of time.

Using the boundary condition above, the streamfunction is given as:

$$\psi(x, y, t) = \begin{cases} U_1 C_1 f_1(y) \sin\left(\frac{\pi x}{a}\right) + U_2 C_2 f_2(y) \sin\left(\frac{2\pi x}{a}\right) & 0 \leq t \leq \tau_f/2 \\ -U_1 C_1 f_1(y) \sin\left(\frac{\pi x}{a}\right) + U_2 C_2 f_2(y) \sin\left(\frac{2\pi x}{a}\right) & \tau_f/2 \leq t \leq \tau_f \end{cases} \tag{4.1}$$

where

$$f_n(y) = \frac{2\pi y}{a}\cosh\left(\frac{n\pi b}{a}\right)\sinh\left(\frac{n\pi y}{a}\right) - \frac{2\pi b}{a}\sinh\left(\frac{n\pi b}{a}\right)\cosh\left(\frac{n\pi y}{a}\right) \tag{4.2}$$

and

$$C_n = \frac{a^2}{2n\pi^2 b}\left[\frac{a}{2n\pi b}\sinh\left(\frac{2n\pi b}{a}\right) + 1\right]^{-1} \tag{4.3}$$

There are no singularities in the boundary conditions for this system, and hence it is a feasible model to build for practical applications. Figure 4.1 shows the possible streamlines with the two different piecewise uniform boundary motions. The motion in the left panel is labeled as FR+ flow (i.e., the flow from $t = n\tau_f$ to $t = (n+1)\tau_f/2$) and the motion on the right is labeled as FL- flow (i.e., the flow for $(n+1)\tau_f/2 \leq t \leq (n+1)\tau_f$) for all non-negative integers n. This set of boundary condition leads to chaotic motion, and a typical picture of a material line (i.e., a horizontal line connecting x_L and x_C as defined below) stretching over three periods is shown in figure 4.2(a).

Using symmetry arguments, a specific ratio of the magnitudes of the two sinusoidal terms in the boundary conditions, U_2/U_1, for a fixed value of the period of the flow τ_f, is found such that it generates three period-3 points in the rectangular domain which form a non-trivial braid in (2+1)D space time dimensions, shown in figure 4.2(b). Looking at figure 4.1, it is apparent that if we can ensure the motion of the three fixed points as given below, it will result in the following stirring protocol in the flow:

1). There exist three points in the flow $\mathbf{x}_L$, $\mathbf{x}_C$ and $\mathbf{x}_R$, such that $\mathbf{x}_C$ is on the centre line $x = 0$ of domain, and $\mathbf{x_L}$ and $\mathbf{x}_R$ are symmetric about $x = 0$.

2). For $0 \leq t \leq \tau_f/2$, i.e., the FR_+ component of the flow period, $\mathbf{x}_L$ is fixed.

3). During the same time, $\mathbf{x}_C$ and $\mathbf{x_R}$ exchange their positions, while moving *clockwise*.

Since the flow pattern is reflected about $x = a$ at $t = \tau_f/2$,

4). For $\tau_f/2 \leq t \leq \tau_f$, i.e., the FL_- component of the flow period, $\mathbf{x}_R$ is fixed.

5). During the same time, $\mathbf{x_C}$ and $\mathbf{x}_L$ exchange their positions, while moving *anti-clockwise*.

The value of U_2/U_1 for which the above conditions are satisfied is found to be ≈ 0.841, and

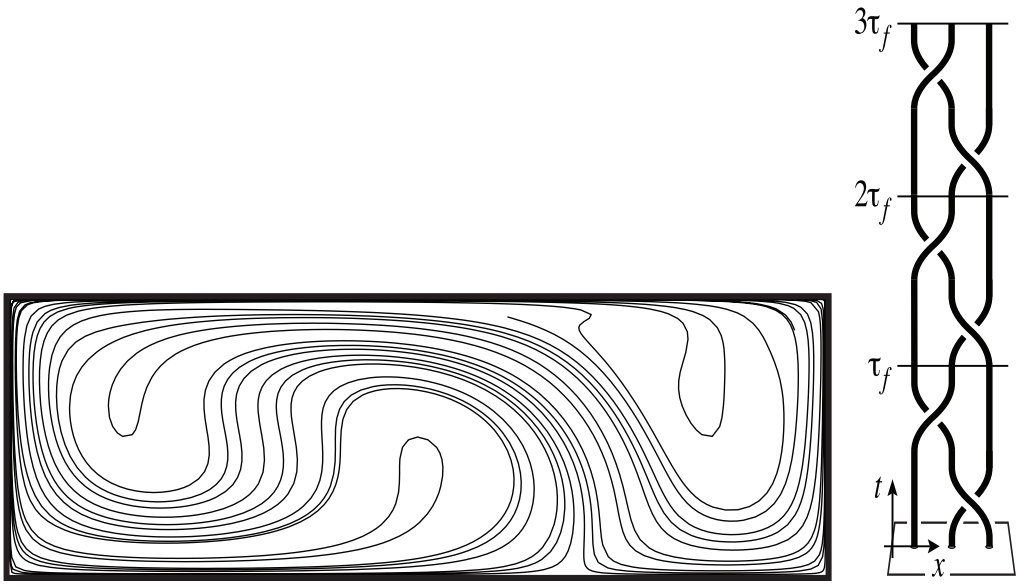

(a) (b)

Figure 4.2: (a).Stretching of material lines for a typical set of parameters in piecewise steady wide-cavity flow. (b) Braiding in the reference case

we normalize the τ_f for this reference case to 1, and call it τ_f^*. Since the braiding protocol in this case is the same as the pA braid discussed in section 2.2, the lower bound h_{TN} on the topological entropy is again given by $\log(\lambda_{TN}) \approx .962$, where $\lambda_{TN} = (3+\sqrt{5})/2$. The braid word for this protocol is $\sigma_{-1}\sigma_2$. For our analysis, we will keep the ratio U_2/U_1 fixed while changing the value of τ_f away from $\tau_f^* = 1$.

4.3.2 Perturbation of the reference case

We study the effect of perturbation in τ_f values on the topological entropy h of the flow. In figure 4.3, the value of h calculated by computing non-trivial material lines in the flows is plotted for different τ_f values away from 1. Also shown in the figure is the lower bound h_{TN} computed via TN theory as discussed in the previous section. The figure shows that this lower bound is very sharp even for a 5% perturbation in τ_f on either side of τ_f^*.

Case 1: $\tau_f > 1$

In the reference case, i.e., when $\tau_f = 1$, there are three period-3 parabolic fixed points that act as ghost rods, and form a non-trivial braid. Since the parabolic fixed points are structurally unstable, we find that for $\tau_f > 1$, each parabolic fixed point bifurcates into a pair of saddles and a pair of centers surrounded by elliptical islands, and the Poincaré section is shown in figure 4.4. The eigenvalues of the fixed points are calculated by numerically forming the Jacobian of the map at the fixed points. The elliptical islands are 'leaky', i.e., there is a small amount of transport across the boundaries of those islands, due the fact that the stable and unstable manifolds of the two saddles intersect transversally for $\tau_f > 1$. In fact, the amount of leaking per period is the amount of phase space enclosed by the lobe(recall section 2.1.2). In figure 4.5, we show the stable and unstable manifolds of saddles in the middle 'blob' and local phase space around it, for $\tau_f = 1.01$ (where the the transversal intersection is present, but not evident) and $\tau_f = 1.04$. Topologically, each blob of phase

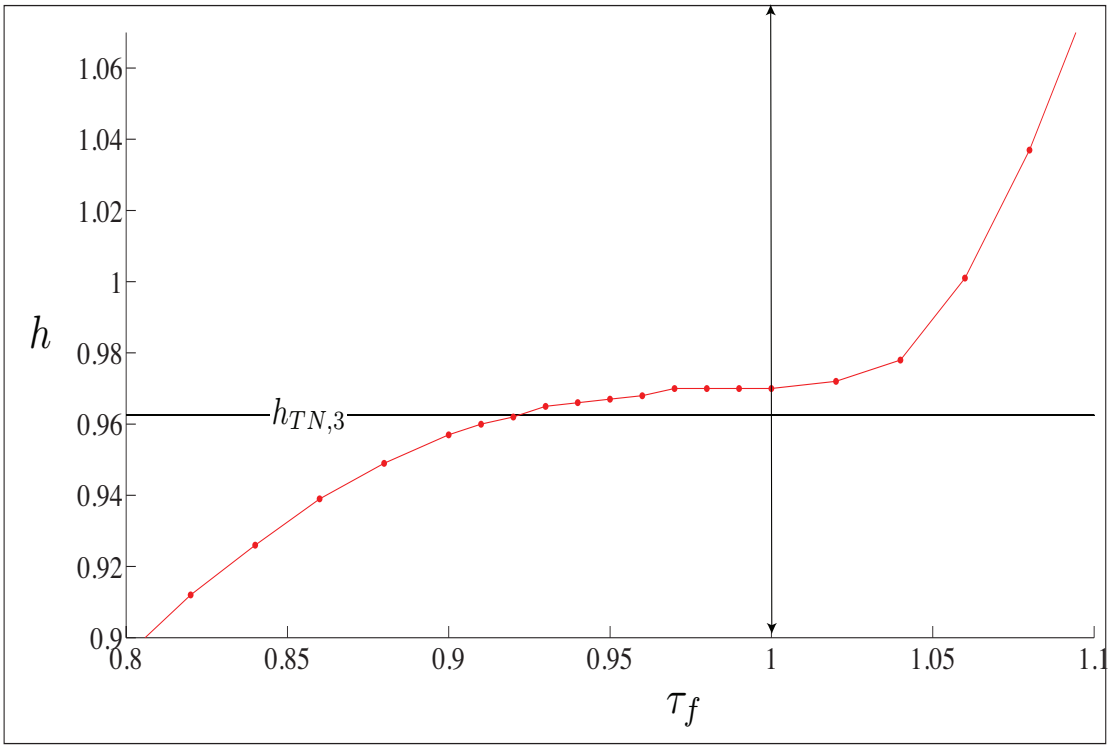

Figure 4.3: Variation of topological entropy as a function of τ_f. Also shown is the lower bound $h_{TN,3}$ computed via TN theory for the braid on 3 strands computed at design point.

space consisting of the above mentioned four fixed points (two saddles and two centers) and the two associated elliptical island pairs act as one ghost rod, thus resulting in a braid on 12 strands reducible to 3 strands. The resulting braiding is topologically exactly the same as in the case of parabolic fixed points (i.e., the reference case), and hence, the lower bound predicted by TNCT remains the same. Figure 4.6 illustrates how such blobs move in phase space to form the same topological braid as before.

Case 2: $\tau_f < 1$

On the other hand, when the value of τ is decreased below 1, no such period-3 fixed points are found in the flow. The Poincaré section looks completely chaotic (see figure **??**. and there are no apparent 'ghost rods' available to form a braid and get a lower bound of the

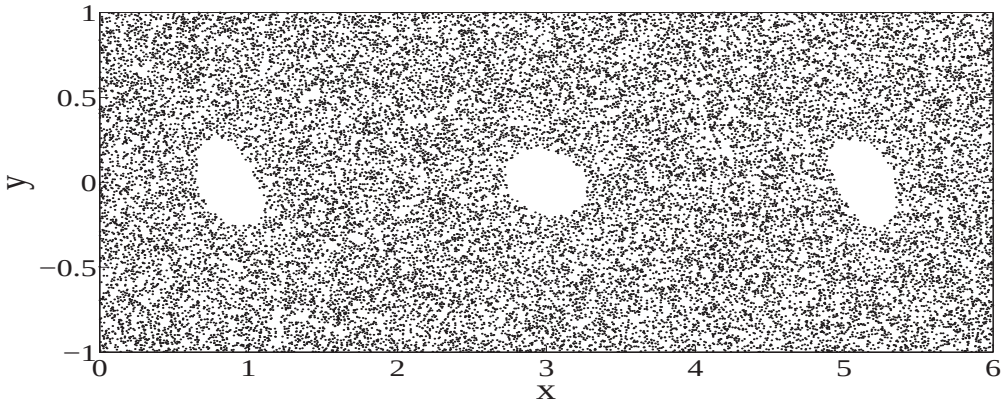

Figure 4.4: Poincaré section for $\tau_f \approx 1.01$. Note the 3 islands that work like stirrers, and are hence called 'ghost rods'. Each such island is associated with 2 saddle and 2 centers, as shown in figure 4.5

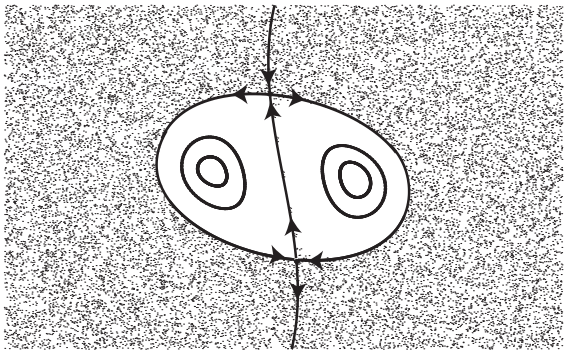

(a) $\tau_f = 1.01$

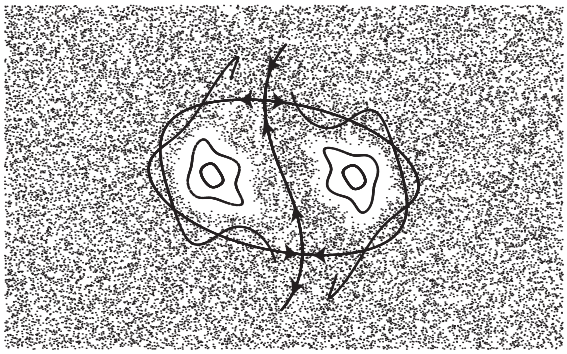

(b) $\tau_f = 1.04$

Figure 4.5: Phase space structure near $x = 0$ (corresponding to middle 'ghost rod' for 2 different τ_f values). While for $\tau_f = 1.01$ the stable and unstable manifolds seem to overlap (a), they clearly intersect transversally for $\tau_f = 1.04$, leading to significant 'leaking' into and out of the region bounded by them (b).

topological entropy of the flow. To explain the fact that the lower bound h_{TN} still holds for $.93 < \tau_f < 1$ as is evident in figure 4.3, we try to extend the TN framework by the use of the concept of almost-invariant sets in the next section.

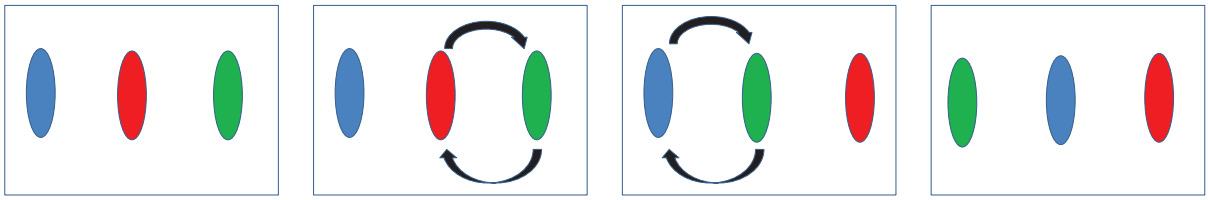

(a) Initial state

(b) First half of the flow period.

(c) Second half of the flow period.

(d) State after 1 flow period

Figure 4.6: Movement of ghost rods in phase space for $\tau_f > 1$

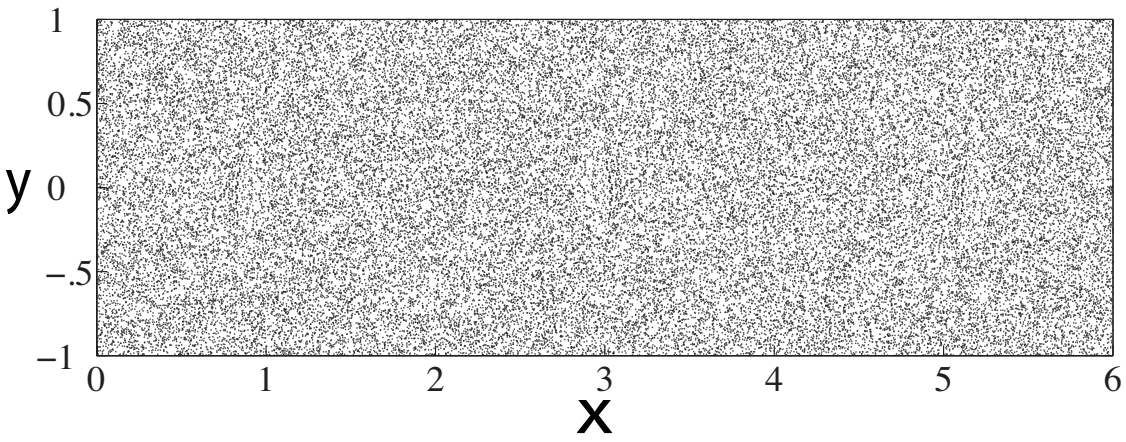

Figure 4.7: Poincaré section for $\tau_f \approx 0.99$. Note the absence of any elliptical islands. No periodic orbits of low period were found.

4.4 Almost-invariant sets

In the absence of periodic points (or elliptical islands), we need to find other structures in phase space that serve used as ghost rods. For this purpose, we use the concept of almost-invariant sets introduced in section 2.2. The motivation of this work comes from the spirit of the TNCT itself. Complexity can be predicted by the motion of periodic points forming a pA braid which lead to exponential stretching because they tend to drag fluid (or phase space volume) with them. One can expect that if the AIS structure braids in a non-trivial way, the TNCT may still be applied to get a lower bound on the stretching and complexity

of the flow.

4.4.1 Procedure

Set oriented methods and the theory of almost-invariant-sets have been described in section 2.2. Here, we concisely describe the procedure of computing almost-invariant sets for the wide-cavity flow system. First, we approximate the dynamics on M by covering it with a collection of $n = 19200$ boxes, i.e., 240 boxes in the x direction and 80 boxes in the y direction. We take 100 equally spaced points in the box, perform a forward iteration for each point for one period of the flow τ_f and monitor the box reached by the iteration. The transition probability from a source box to a destination box is measured by the ratio of the number of points from the source box reaching the destination box in one iteration step. This *transition matrix* P_{t,τ_f} contains all the information for the computation of the transport quantities of interest with entries

$$p_{ij} = m\left(f^{-1}(B_i) \cap B_j\right)/m(B_j)$$

where $B_1, \ldots, B_n$ are the boxes in the covering, f is the solution map $\phi_t^{\tau_f}$ from time t to $t + \tau_f$, and m is the area measure, i.e., the phase space volume measure. Note that the stochastic matrix P_{t,τ_f} may be viewed as a transition matrix of an n-state Markov chain. Since the matrix P_{t,τ_f} is not reversible in time, we form a new reversible matrix R_{t,τ_f} and find its eigenspectrum. We can restrict to only those partitions $(A_1, A_2, ...A_k)$ such that each member (or each almost-invariant set) A of such a partition is a union of some sets in $(B_1, B_2, ...)$, i.e each $A = \cup_{i\in I} B_i$, for some set of box indices $I \in \{1, 2, ..., n\}$. The eigenvalues and eigenvectors of the matrix R_{t,τ_f} provide insight into the various almost-invariant sets present in the system. The first eigenvector v_1, corresponding to an eigenvalue $\lambda_1 = 1$ is the invariant distribution of the system. Since the system under consideration is a Hamiltonian system, we find that v_1 corresponds to a uniform distribution all over the phase space. This implies that $\mu = m$, i.e. the invariant measure is the same as volume measure and this is verified in our computations.

The two sets given by the regions in phase space such that $v_2 > c$ and $v_2 < c$, where the eigenvector v_2 corresponds to the second largest eigenvalue λ_2 isolates an almost-invariant set structure. More precisely, the two almost-invariant-set structures are defined as follows: Let $I_1 = \{i : (v_2)_i > c, 1 \leq i \leq n\}$ and $I_2 = \{i : (v_2)_i < c, 1 \leq i \leq n\}$, then $A_1 = \cup_{i \in I_1} B_i$ and $A_2 = \cup_{i \in I_2} B_i$. Here, by $(v_2)_i$, we mean the ith component of the vector v_2, i.e. the value of v_2 assigned to the box B_i. For the majority of cases, we will take $c = 0$, but to maintain consistency across figures, for non-zero c, we plot $(v_2)_i - c$ values while identifying the almost-invariant sets, so that the zero contour on the figure always refers to boundaries delineating the almost-invariant set structure.

We show the almost-invariant set structure for $\tau_f = 0.99$ in figure 4.8. The collection of the three prominent sets, corresponding to the set A_1 (i.e., the region where $v_2 > 0$), forms an almost invariant set. This almost invariant set actually consists of three almost cyclic components, which form a 3-braid, as discussed next. Each (positive) lower eigenvalue has an associated eigenvector whose zero contour isolates other almost invariant sets, which are more 'leaky', i.e., lower the eigenvalue, lower is the invariance of the associated almost invariant set.

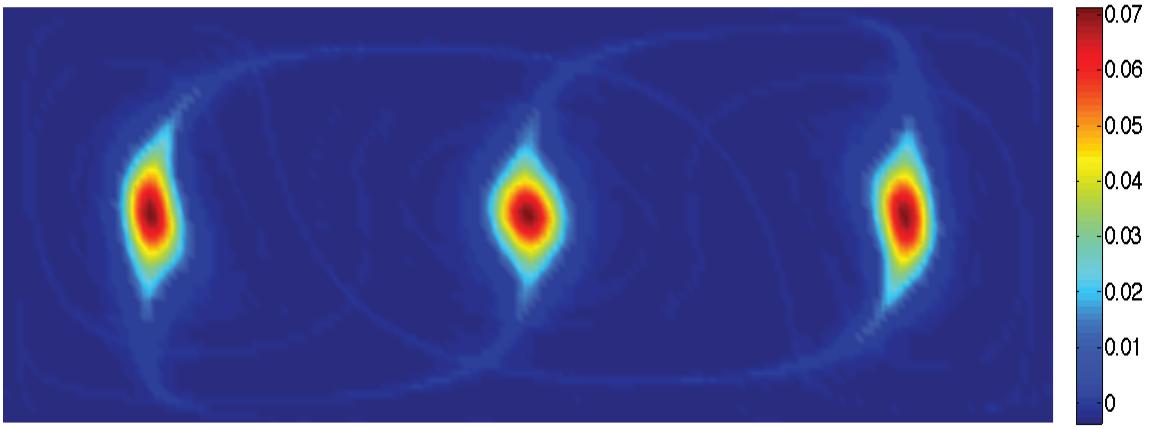

Figure 4.8: AIS structure for $\tau_f \approx 0.99$. The zero contour is the boundary between the two almost invariant sets. Compare with the Poincaré section for the same τ_f shown in figure 4.7

4.4.2 Braiding of almost-invariant sets

While the period-3 fixed points cease to exist for $\tau_f < 1$, we can see from figure 4.8 that the almost-invariant sets still exist in the same region in the phase space. We look for braiding of these sets, and see if this structure forms a pA braid for $\tau_f < 1$ similar to the one formed by periodic points (and elliptical islands) for $\tau_f > 1$. We use $\tau_f \approx 0.975$ for our analysis in this case. We form 20 different *time-shifted* versions of the Markov operator P, i.e., P_{t_i,τ_f} for $i = 1, 2, ...20$, and $t_i = (i-1)\tau_f/20$. Then, for each of the corresponding R_{t_i,τ_f}, we find the almost-invariant structure based on the second eigenvector as mentioned previously. In figure 4.9, we show these structures for the first half of the time period of the flow. Recall that this braiding protocol corresponds to σ_2, and is the same as the one formed by parabolic periodic points for $\tau_f = 1$. Similarly, for the second half of the time-period of the flow, the stirring protocol is the one given by σ_{-1}. Hence, the braid formed by the almost-invariant sets structure (given by $\sigma_{-1}\sigma_2$) for $\tau_f \approx 0.975$ is exactly the same as the braid formed by periodic points for $\tau_f = 1$ or by elliptical islands for $\tau_f \geq 1$. Three periods of the complete braid in (2+1)D formed by this structure is shown in figure 4.10. So the lower bound on topological entropy is again given by $h_{TN} \approx 0.962$, and we can see from figure 4.3 that this lower bound is still valid.

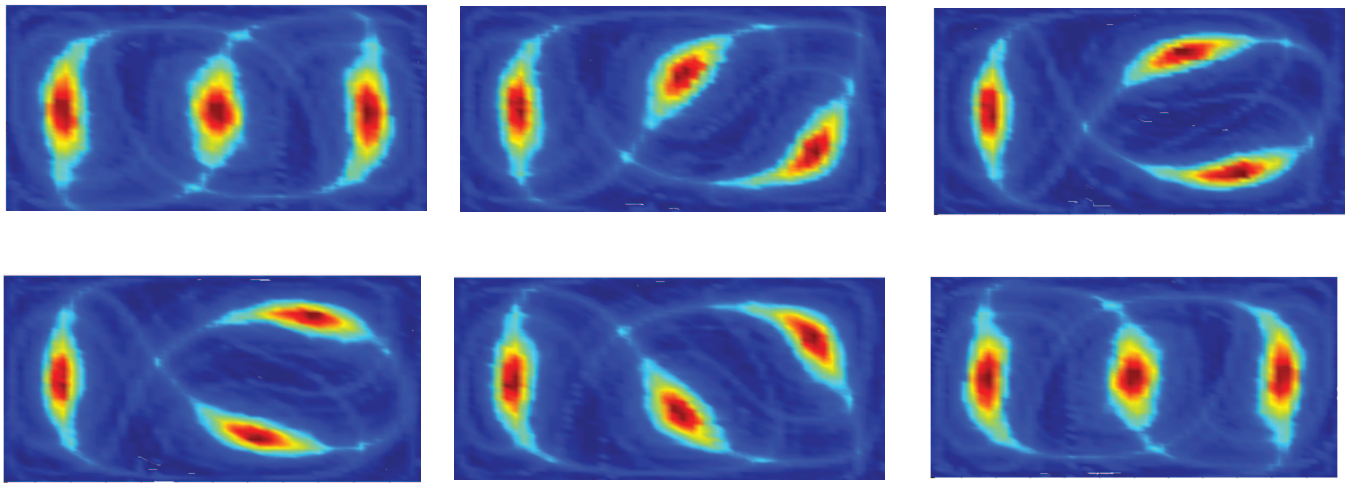

Figure 4.9: Almost-invariant sets structure for time shifted Markov operators for $\tau_f \approx 0.975$. Left to right: Top-row: t_i= 0, $0.1\tau_f$, $0.2\tau_f$. Bottom row: $0.3\tau_f$, $0.4\tau_f$, $0.5\tau_f$

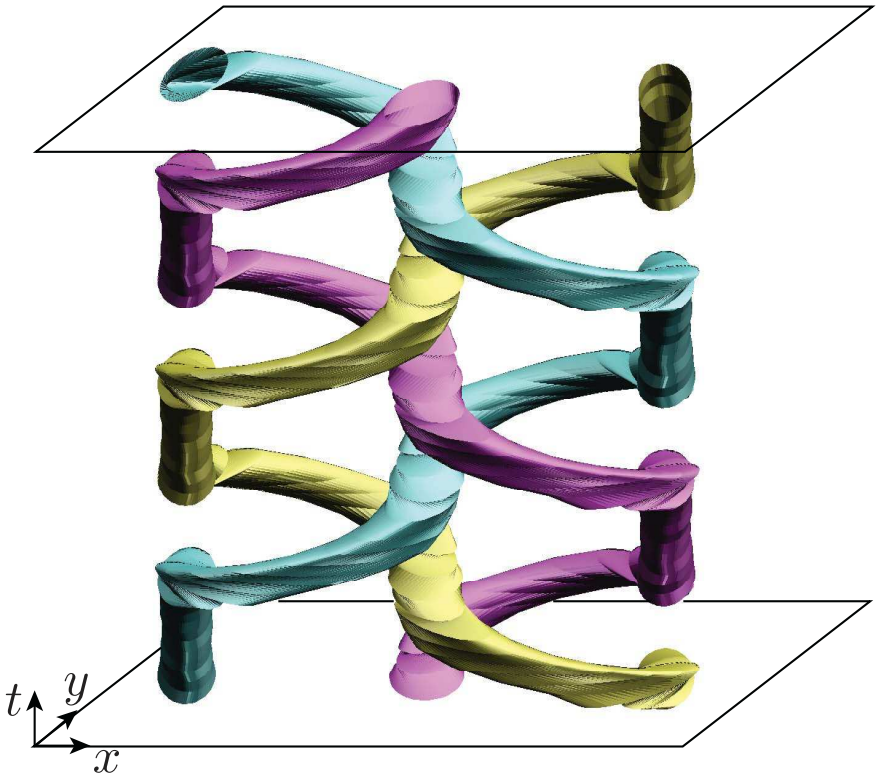

Figure 4.10: Braiding in (2+1)D via three almost invariant sets for $\tau_f \approx 0.975$, a parameter value where the corresponding periodic points no longer exist. The braid is shown for 3 periods of flow. The braid is topologically the same as figure 4.2(b)

4.4.3 Persistence of almost-invariant set structure: Bifurcation of the braids

Figure 4.11 shows the continuation of the eigenvector which captures the braiding structure correctly for $\tau_f \leq 1$, and the corresponding eigenvalues.

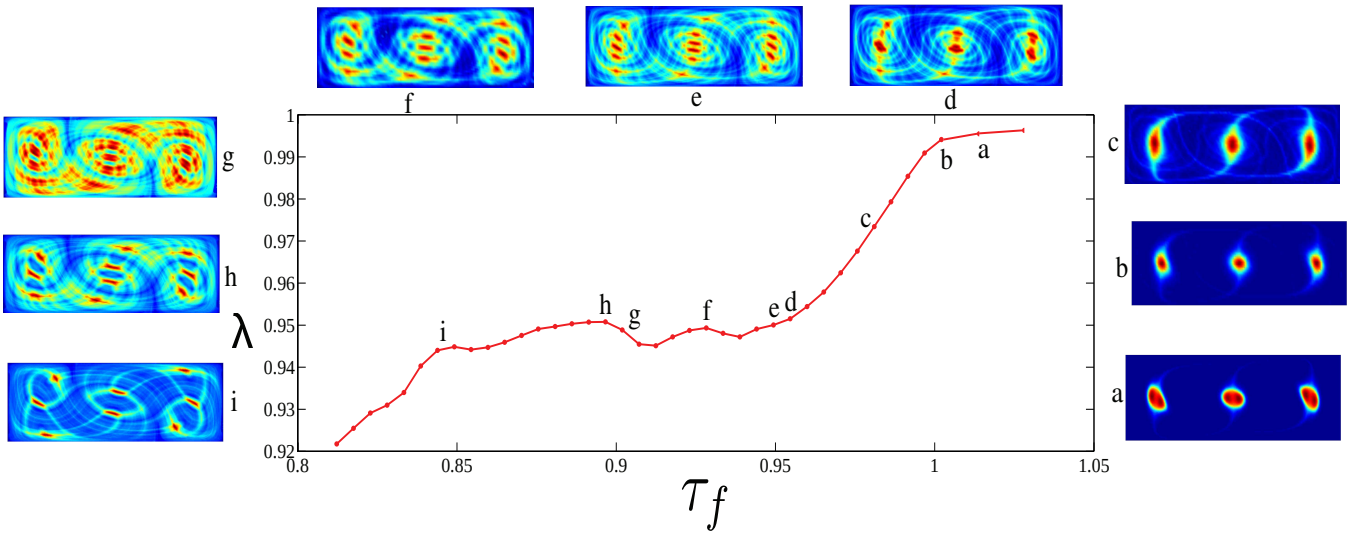

Figure 4.11: Almost-invariant set structure via continuation of the 3-strand eigenvector found at (b) for various values of τ_f and the corresponding eigenvalue. The structure shown in (a), (b) and (c) can clearly be identified as the 3-strand mode. The structure in (e) consists of 16 strands, while (f) can be seen to have 13 strands. (h) has 10 strands while (i) consists of 8 clearly identifiable strands. The structures in (d) and (g) are the fuzzy ones which belong to different transition regions.

For $1 < \tau_f < 1.05$, the second eigenvector of the corresponding R_{0,τ_f} matrix gives the correct braiding structure. The continuation of the 3-strand eigenvector for $\tau_f < 1$ is carried out as follows. We discretize the parameter space $.8 < \tau_f \leq 1$ into intervals of size $\delta\tau_f = (0.025/4.74) \approx .005$. Then we calculate the reversibilized Perron-Frobenius operator R_{0,τ_f} for each of those parameter values. We compute the top 10 eigenvectors (excluding the eigenvector corresponding the eigenvalue 1) $(\nu_2^{\tau_f}, .., \nu_{11}^{\tau_f})$ for each of those operators. Our aim is to identify the eigenvector for each τ_f which gives the braiding structure for the flow at that parameter value. We denote this eigenvector by $\nu_*^{\tau_f}$. We know that for $\tau_f = 1$, the

eigenvector that gives the relevant braiding structure is the second eigenvector, so $\nu_*^1 = \nu_2^1$. We calculate the inner product of ν_*^1 with each of the 10 eigenvectors of the next lowest τ_f value, i.e., $\tau_f = 1 - \delta\tau_f$, and we compute the inner-product $\langle \nu_*^1, \nu_j^{1-\delta\tau_f} \rangle$ for $j = 2, ..., 11$. Then we select the eigenvector at $1 - \delta\tau_f$ which gives highest absolute value among the dot products, and call it $\nu_*^{1-\delta\tau_f}$. Similarly the continuation is carried out for $\tau_f = 1 - 2\delta\tau_f$ by taking the dot products with $\nu_*^{1-\delta\tau_f}$ and so on. Denote by β_{τ_f} the value $\langle \nu_*^{\tau_f}, \nu_*^{\tau_f - \delta\tau_f} \rangle$.

We make some observations based on figure 4.11. The almost-invariant set structure consisting of 3 sets seems to persist till $\tau_f \approx 0.96$. We also observe that as the value of τ_f decreases further, the structure consisting of 3 almost cyclic sets starts breaking up, as seen in figure 4.11(d). Observe that at $\tau_f \approx 0.95$, a structure consisting of 16 almost invariant sets can be seen (figure 4.11(e)). There is another change in the braiding structure, and figure 4.11(f) shows a 13-strand structure. Moving further to the left on the τ_f axis, we see 10-strand and 8-strand structures in figures 4.11(h) and 4.11(i). We show another structure which occurs during the transition between 13 and 10 strand structures in 4.11(g).

This break up of the AIS-based braiding structure can be better understood by plotting the β_{τ_f} values, figure 4.12. This inner product gives a measure of *closeness* of the eigenvectors for two neighboring τ_f values and captures changes in the eigenmode morphology. We observe that in regions where we can clearly identify the different braiding protocols consisting of 3, 16, 13, 10 or 8 stands, the value of β_{τ_f} remains almost constant. On the other hand in the transition regions where there is no clearly identifiable braid structure, there is a sharp drop in the β_{τ_f} value, signifying large change in the structure of the eigenvector. Intuitively, this means that each of the braiding structures persists for a range of τ_f values, and then undergoes a transition (or bifurcation) into another braiding structure. Comparing figure 4.11 with figure 4.12, we see that the dips in β_{τ_f} vesus τ_f seem to capture the boundaries of different braiding structures and transition regions well.

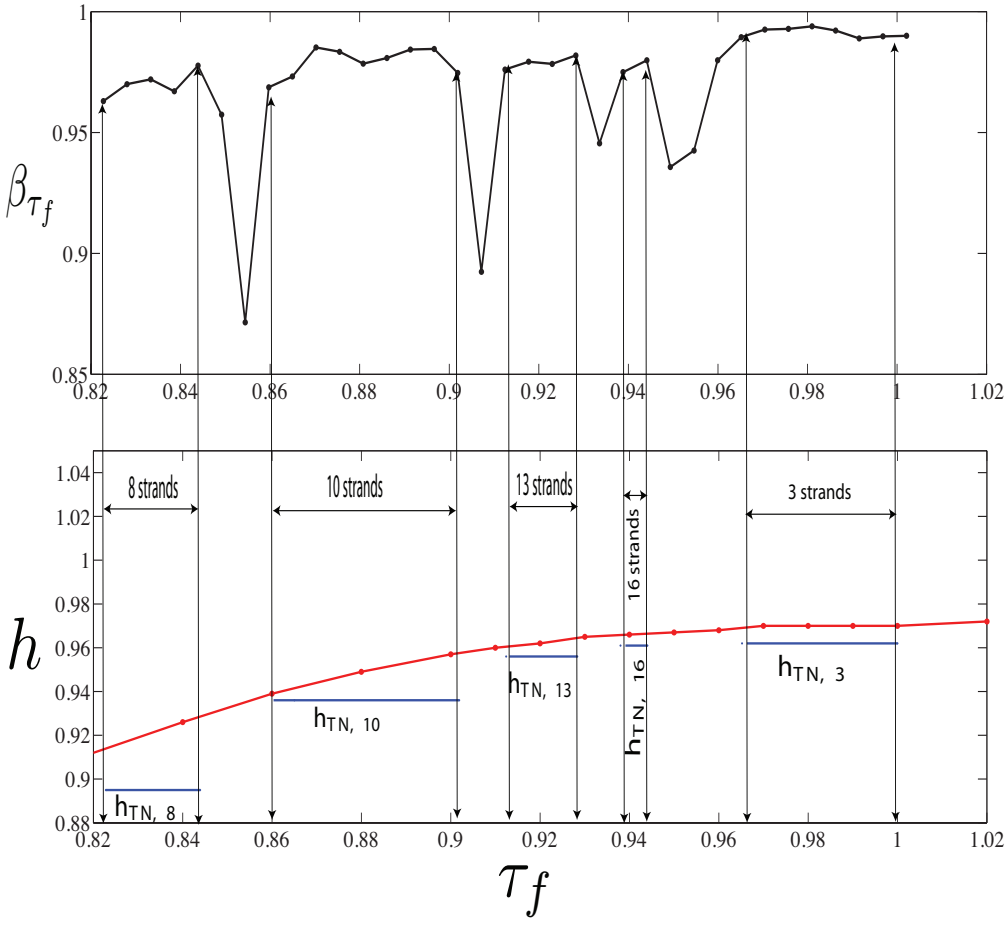

Figure 4.12: (Top) β_{τ_f} for the range of τ_f values. The regions where this value stays almost constant are the regions of persistence of different braiding structures, separated by transition regions where the value drops significantly.(Bottom) The topological entropy of the flow computed by line stretching is shown in red. The lower bound computed by TNCT for different braiding structures is shown in blue in the relevant regions.

We are interested in finding the lower bound using the TNCT for each of the braiding structures that we have identified. We compute the time-shifted Markov operators, similar to what was done for the 3-strand structure in the previous section. We discuss the process for $\tau_f \approx 0.93$, where a 13-strand structure is found. In figure 4.13, we show the phase-shifted eigenvectors corresponding to $\tau_f = 0.93$ for first half of the time period $\tau_{f,13}$, where the braiding motion of 13-strand structure can be clearly seen. In figure 4.14, we illustrate the motion of various strands during one period of the flow. Each of the 13 strand structures consists of four strands each on left and right, and five in the center. During the first half of the time period (i.e., R_+ flow), the center blob moves as in the case of 3-strand structure, but one of the strands (labelled B1 in figure 4.14) breaks away from the center blob, and does not undergo the prescribed R_+ motion completely. Similarly, during pulse 2, the strand labelled C1 moves out of the central blob and does not complete the prescribed L_- motion. This leaking of phase space volume, captured by the AIS computation, helps us identify the correct braiding occuring in the flow. This braiding is clearly topologically different from the braiding on 3 strands shown earlier in figure 4.9.

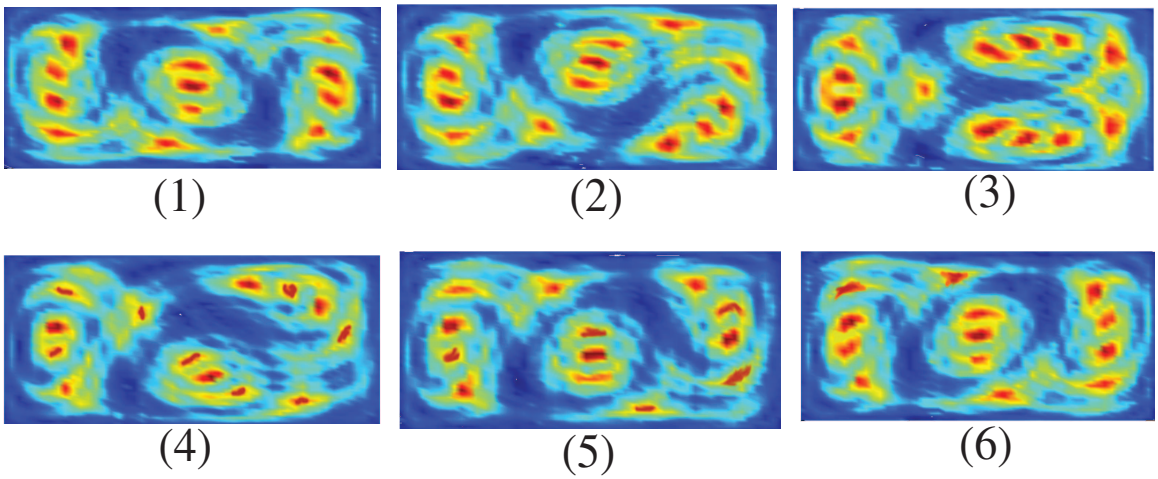

Figure 4.13: AIS identified by second eigenvectors of time-shifted Markov operators for the first half of the time period (the time-shift is increases from t=0 at (1) to t=$\tau_f/2$ at (6)), for $\tau_f \approx 0.93$. The braiding motion of the 13-strand structure is clearly evident.

(a) Initial state

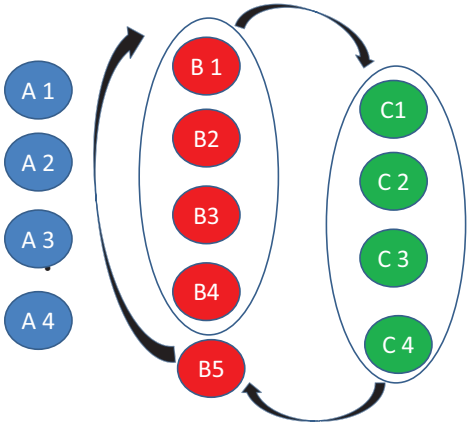

(b) Movement during pulse 1

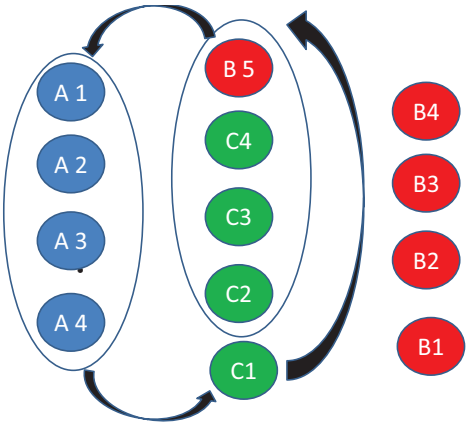

(c) Movement during pulse 2

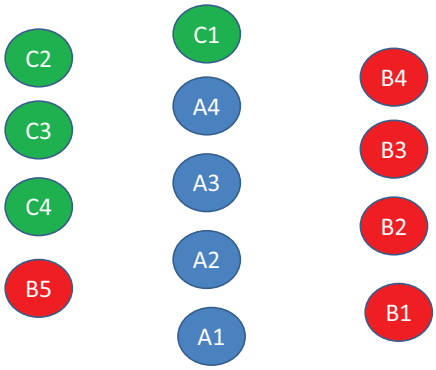

(d) State after 1 period(or 2 pulses)

Figure 4.14: Movement of 13 almost invariant sets over 1 period consisting of 2 pulses. The braiding is period-13. Note that what was formerly the central blob now consists of five disjoint sets (strands), shown in red. During the first pulse, the strand B5 breaks away from the blob, and does not follow the prescribed motion. Similarly during pulse 2, C1 does not move with rest of the central blob. This phenomenon captured by the AIS structure, makes the braiding different from the braiding on 3-strand shown in figure 4.9

Number of strands	Topological entropy of the braid
3	0.962
16	0.961
13	0.956
10	0.936
8	0.894

Table 4.1: List of topological entropy values of the braids formed by AIS structures as τ_f is decreased below 1.

The complete mathematical braid for the 13-strand structure for one time period is shown in figure 4.15. This braid consists of 22 'interchanges' or crossings in each half of the time period, and the braid word is given by:

$\tau_f \geq t \geq \tau_f/2 : \sigma_L = \sigma_{10}\sigma_{11}\sigma_{10}\sigma_{12}\sigma_{11}\sigma_{10}\sigma_{-4}\sigma_{-5}\sigma_{-3}\sigma_{-6}\sigma_{-4}\sigma_{-2}\sigma_{-7}\sigma_{-5}\sigma_{-3}\sigma_{-1}\sigma_{-6}\sigma_{-4}\sigma_{-2}\sigma_{-5}\sigma_{-3}\sigma_{-4}$

$\tau_f/2 \geq t \geq 0 : \sigma_R = \sigma_{-3}\sigma_{-2}\sigma_{-3}\sigma_{-1}\sigma_{-2}\sigma_{-3}\sigma_9\sigma_8\sigma_{10}\sigma_7\sigma_9\sigma_{11}\sigma_6\sigma_8\sigma_{10}\sigma_{12}\sigma_7\sigma_9\sigma_{11}\sigma_8\sigma_{10}\sigma_9$.

The complete braid word for one time period is formed by composing the above two braid words together (i.e., $\sigma_L\sigma_R$). Note that the above braid word is given in the convention described earlier, i.e., the last interchange appears first. The lower bound on the topological entropy of this braid is found to be $h_{TN,13} \approx 0.956$. This braid persists for roughly $0.91 \leq \tau_f \leq 0.93$. We follow a similar procedure for finding the lower bound on topological entropy for braids consisting of 8, 10 and 16 strands. Table 4.1 lists the topological entropy of the various braids. The braid words for all the braids are given in the appendix. We see that the lower bounds are sharp lower estimate, and more importantly, a good estimate for the *actual* topological entropy calculated by line stretching for τ_f values in the respective τ_f regions, as shown in figure 4.12. **This is a key result and gives us confidence in asserting that the AIS-based topological analysis can be used in the framework of the TNCT**. We have first identified the eigenvector ν_*^1, of the Markov operator that

correctly picks up the braiding at the design point, i.e., $\tau_f = 1$. Then we identify braiding structures defined by the eigenvectors formed by continuation of ν_*^1, and applied the TNCT on those braiding structures and found that topological entropy of those braids are excellent lower bounds and estimates of the actual entropy of the system for the relevant parameter values.

Next, we show the mathematical representations of the various braids described above. Note that the basic behavior in all these cases tends to follow the pattern observed in the 13-strand case. As is evident from figure 4.14, one of the strands from the center blob tends to break away from the prescribed R_+ and L_- motions, and hence we get topologically different braiding in each case. Notice that since the number of strands decreases monotonically from 16 to 8 while moving left on the τ_f axis, the fraction of phase space volume effectively not folllowing the prescribed motions of the original 3-strand design point increases monotonically as (1/16),(1/13),(1/10) and finally (1/8). This deviation from the braiding protocol of design points (i.e., $\tau_f = 1$) due to the result of phase space leaking, results in inefficient mixing away from the design point, as evident in figure 4.12 and is captured by the AIS structures.

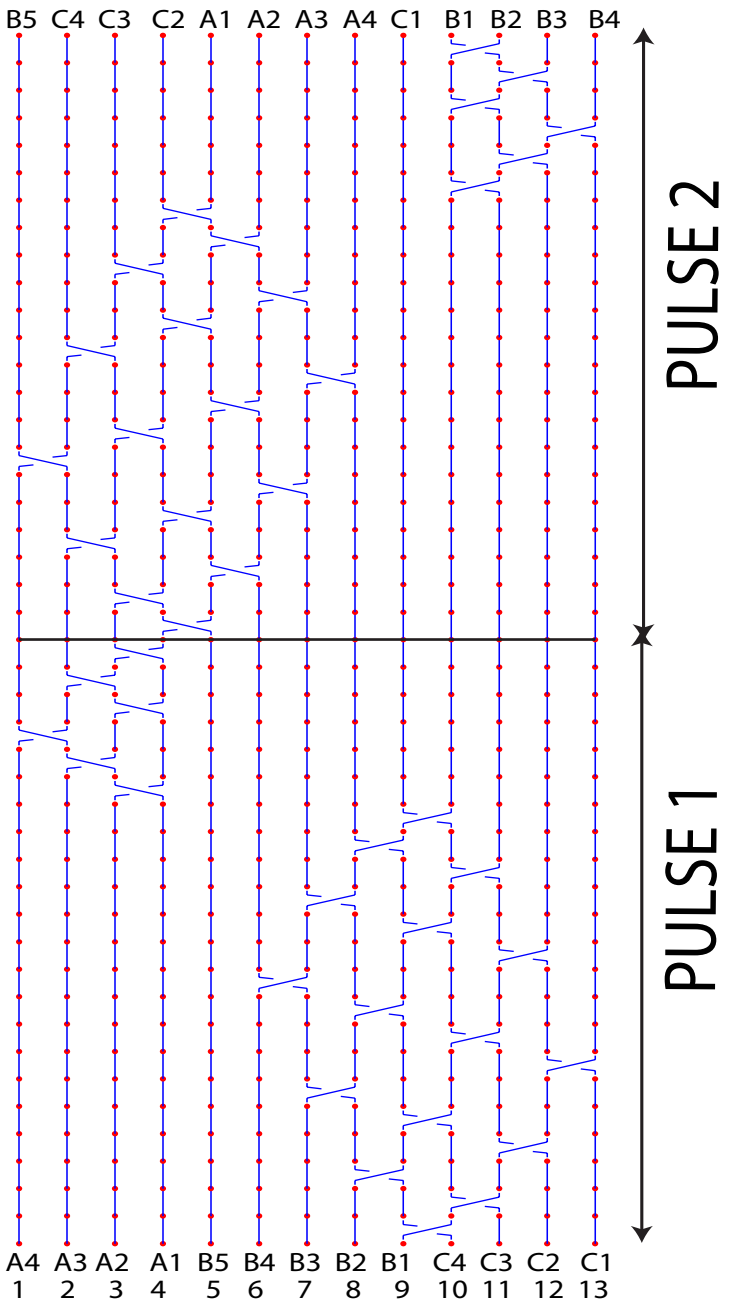

Figure 4.15: Mathematical representation of the braid on 13 strands, $\tau_f = .9283$. Pulse 1 refers to first half of the time period, and Pulse 2 is the second half. This is a periodic braid with period 13. The time is increasing from bottom to top.

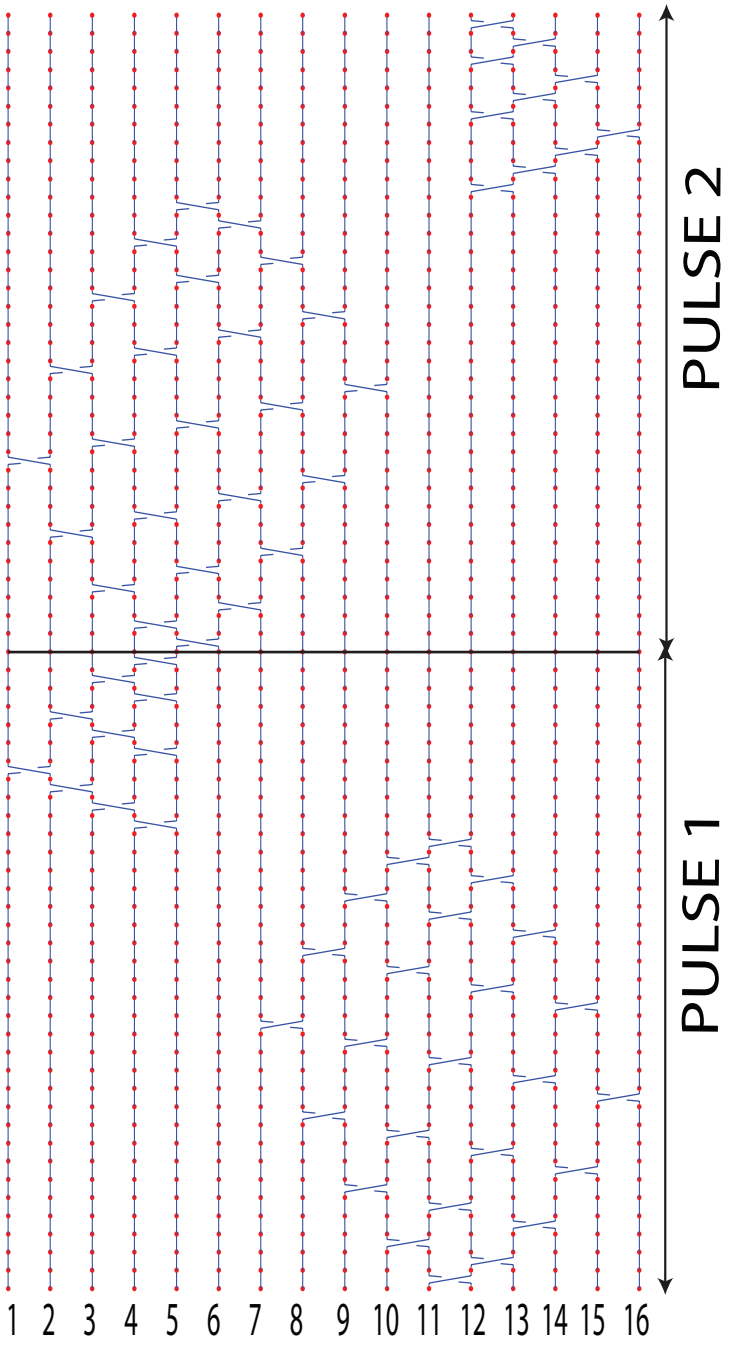

Figure 4.16: Mathematical representation of the braid on 16 strands, $\tau_f = 0.9494$. Pulse 1 refers to first half of the time period, and Pulse 2 is the second half. This is a periodic braid with period 16. The time is increasing from bottom to top.

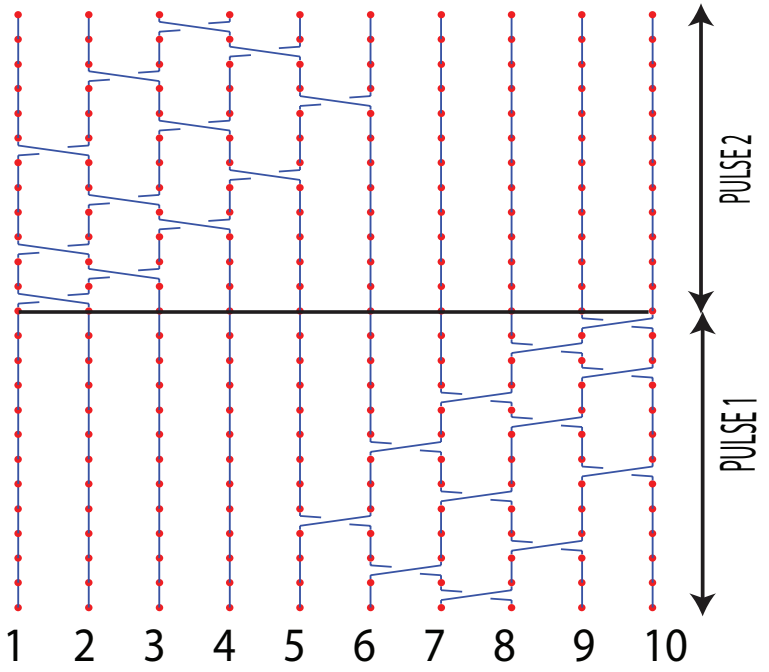

Figure 4.17: Mathematical representation of the braid on 10 strands, $\tau_f = 0.8966$ Pulse 1 refers to first half of the time period, and Pulse 2 is the second half. This is a periodic braid with period 10. The time is increasing from bottom to top.

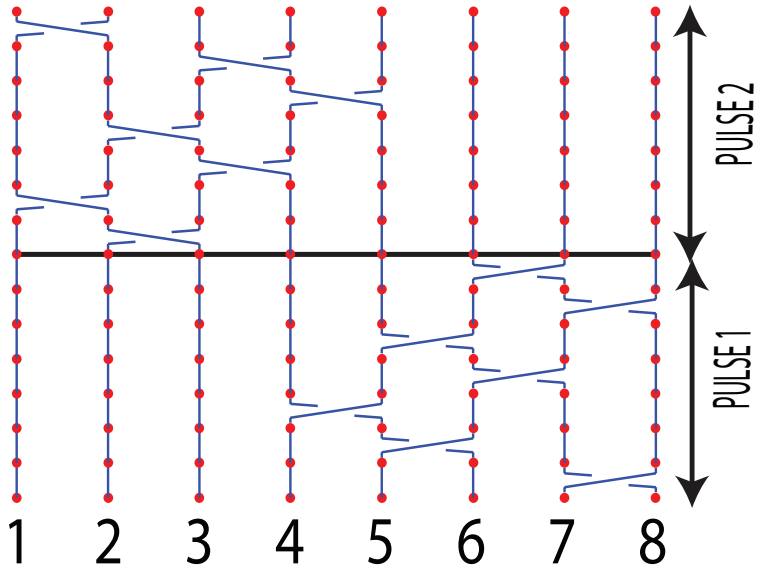

Figure 4.18: Mathematical representation of the braid on 8 strands, $\tau_f = 0.8439$. Pulse 1 refers to first half of the time period, and Pulse 2 is the second half. This is a periodic braid with period 8. The time is increasing from bottom to top.

Remarks:

- Our work generalizes the TN-framework to systems which have no periodic fixed points by the use of AIS structure of the system. This method is effective because the set oriented approach enables us to find the sets that do not 'leak' significantly and also are almost cyclic (or periodic) in time. If they braid non-trivially, they mimic the behavior of physical rods or motion of punctures that is required for existence of chaos by the application of TNCT.

- The braids on 8, 10, 13 and 16 strands comprise of 'blobs' of phase space that have formed after the break up of sets that made up the 3-set AIS. This breakup can be seen to be a result of leaking of phase volume roughly along the invariant manifolds of periodic points for $\tau_f > 1$. In figure 4.19, the invariant manifolds are plotted for $\tau_f \approx 1.01$, and the AIS structure for $\tau_f = 0.93$ is also highlighted. It is observed that the new sets appear in the AIS structure along the manifolds, close to primary intersection points.

- The braid words for the braids consisting of different number of strands have been identified by visually inspecting the space-time crossings of the various sets that form the AIS structure. This process can potentially be automated in the spirit of [54], where an algorithm to automatically compute braid crossings of particle trajectories has been described. The automation for AIS is more involved because of the fact that crossings of different sets may be hard to define mathematically in a general way. Defining the geometric center of each set as the 'fixed' point could be a starting point for such a procedure.

- The computation of the entropy of a given braid has been carried out using the freely available software based on the Bestvina-Handel [20] train track algorithm. But recently, another more computationally efficient algorithm [55] has been reported, which can significantly speed up the process.

- AIS structures can be computed for systems accessible solely by time series data. See [56] for an application of set-oriented techniques to detect AIS structures using position data of ocean surface flows. This implies that the TN-framework may be extended to such systems, making it potentially a very powerful technique for quantitative and qualitative analysis of complex systems.

4.5 Contribution to the literature

Our work is the first instance of using the concept of almost-invariant sets as central objects in the context of Thurson-Nielson classification theorem for the purpose of calculating lower bounds on topological entropy by looking at the non-trivial braids formed in the flow. This broadens the scope of problems where such a bound could be found i.e., time varying systems that do not have any well defined fixed points, such as free surface flows, or time-independent systems which are operating in a parameter regime where there do not exist any easily-identifiable fixed points. We give numerical evidence that these almost-invariant-sets are the natural objects on which to pin the Thurston-Nielsen classification theorem. This implies that prediction about chaos can be made by looking at regions in phase space that move together for finite amount of time. We also show that the lower bound given by this procedure holds even in the case where the braid word is not the one originally formed by periodic points i.e., in case of braid bifurcation, the new braid dictates the complexity of the flow.

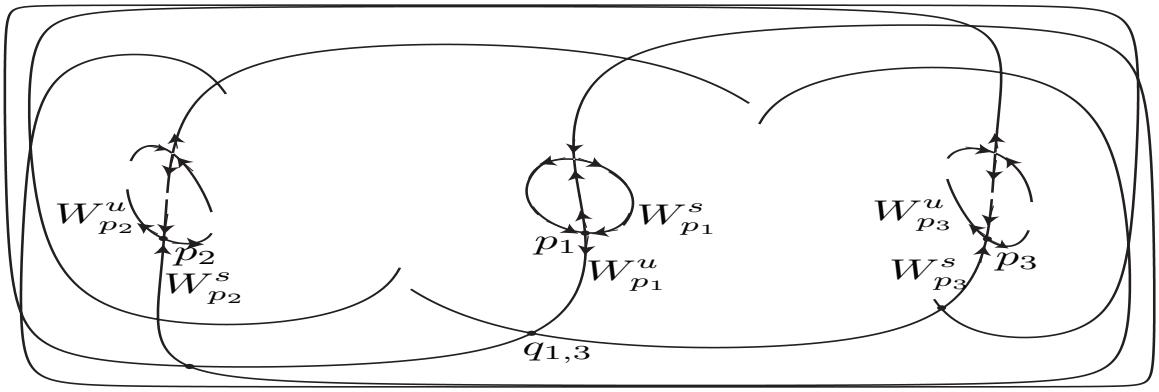

(a)

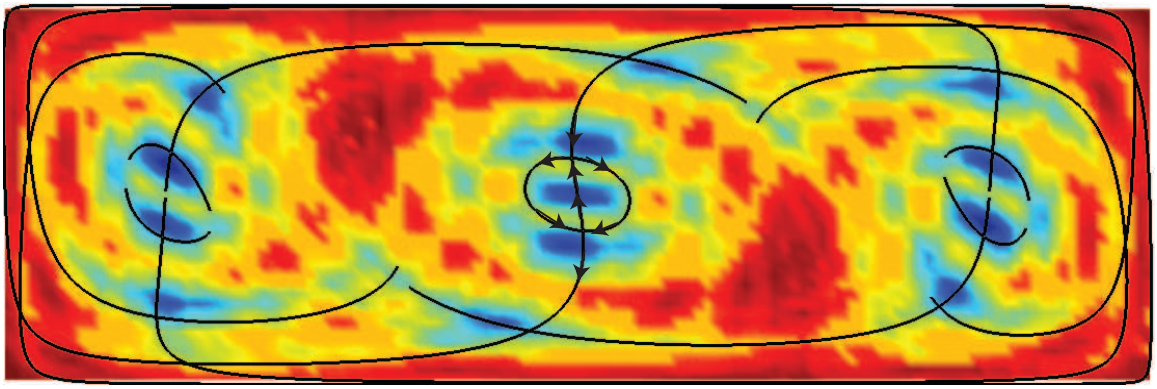

(b)

Figure 4.19: (a) Invariant manifolds for $\tau_f = 1.01$, with three of the six saddle points marked. Also marked is the primary intersection point $q_{1,3}$. (b) The 13-AIS structure for $\tau_f \approx 0.93$ is superimposed. Notice that the sets in this structure seem to lie on or very close to the manifolds, and the new sets appear near the primary intersection points.

4.6 Addendum: Phase space mixing in the three-body problem

The planar circular restricted three-body problem, described in chapter 3 is a classical problem in celestial mechanics, and has been analyzed using a variety of dynamical systems techniques. In this section, we document an attempt to study mixing in the phase space of the PCR3BP using topological methods, and the almost-invariant sets framework described earlier in this chapter. Braiding in the three-body problem has generally been studied in the context of configuration-space (position space) orbits of various bodies that form interesting looking braids [57], [58]. But our aim is different as we want to explore the possibility of proving and estimating chaotic behavior in a specific case of the three-body problem, as was attempted in [59] by a different set of topological methods.

4.6.1 Description of the problem

We are interested in finding non-trivial braids that occur in the phase space of the PCR3BP, using the framework of almost-invariant sets developed previously in this chapter. We restrict our attention to two-dimensional Poincaré maps on the three-dimensional energy manifold of the PCR3BP, and hence look for (2+1)D braids. One key difference between this problem and the fluid-flow problem that was discussed earlier is that the braids in PCR3BP lie in the phase space itself, unlike the extended phase space (of two space and one time dimension) braids discussed before. For our computations, we choose the mass parameter μ of the system to be ≈ 0.001, and choose the Jacobi constant $C_J \approx 3.04$, which implies that the particle P cannot move between different realms. The particle is initially chosen to be in the interior realm, and will stay there for all time. We will work in the rotating coordinate system and use polar coordinates $(r, \theta, \dot{r}, \dot{\theta})$ for our computing the Poincaré sections.

Poincaré maps defined

We consider the Poincaré surface of section defined by $(\theta = \theta_i, \dot{\theta} > 0)$ and the coordinates on the section are $(r, \dot{r})$. Defining a family of Poincaré maps $\mathbf{P}_{\theta_i}$ on a two dimensional section Σ_{θ_i} in the four dimensional phase space, where

$$\Sigma_{\theta_i} = \{(r, \theta, \dot{r}, \dot{\theta}) | \theta \bmod 2\pi = \theta_i \text{ and } H(r, \theta, \dot{r}, \dot{\theta}) = -0.5 C_J, \text{ with } \dot{\theta} > 0\} \tag{4.4}$$

We define the map as,

$$\mathbf{P}_{\theta_i} : \Sigma_{\theta_i} \to \Sigma_{\theta_i} \tag{4.5}$$

$$R(\theta_i) \to R(\theta_i + 2\pi) \tag{4.6}$$

where $R = (r, \dot{r})$, $\theta_i = i(\delta\theta)/(2\pi)$ for $i = 1, ..., n$ and $\delta\theta = (2\pi)/n$. We take $n = 16$ for our analysis.

Given an initial condition $(r, \dot{r})$ on the section Σ_θ, we perform the following computations to obtain the Poincaré map numerically. First, $\dot{\theta}$ is found by using the relation obtained by invariance of Jacobi constant

$$\dot{\theta} = \frac{\sqrt{-(C_J + 2\bar{U} + \dot{r}^2)}}{r}$$

Then we obtain the positions and velocities in rectangular coordinates in the rotating frame

$$x = r\cos\theta$$

$$y = r\sin\theta$$

$$\dot{x} = \dot{r}\cos\theta - r\sin\theta\dot{\theta}$$

$$\dot{y} = \dot{r}\sin\theta + r\cos\theta\dot{\theta}$$

The initial condition is propagated forward using the PCR3BP equations, and intersections with the Poincaré section Σ_{θ_i} are recorded. Figure 4.20 shows the connected chaotic components of the Poincaré sections for $\theta_i = 0, \pi/8, 2\pi/8$. We notice that various elliptical islands associated with different resonance regions move in a circular motion as θ_i is increased from 0

to $\pi/8$ and beyond. The direction of motion of these resonances can be identified by seeding a point inside the elliptical islands, and then looking at the iterates of this point. For instance, the motion of the resonant islands with the red circles in figure 4.21 is anti-clockwise (period 4 and period 5), and those shown with green circles move clockwise (period 2 and period 3) as the angle of section θ_i is increase from 0 to 2π. The big period one resonance in the middle of the surface of section is the dividing surface between resonant islands rotating in the two directions.

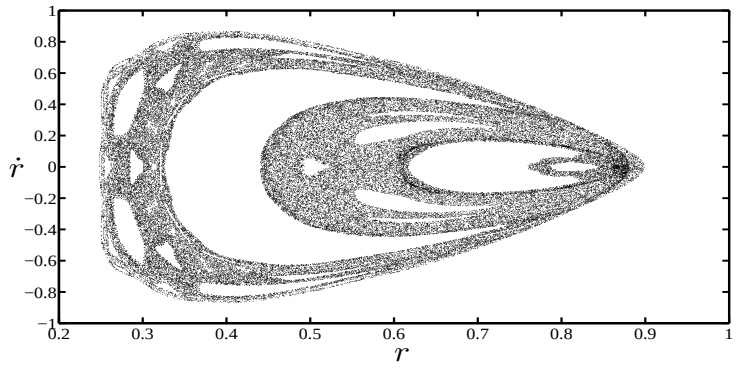

(a)

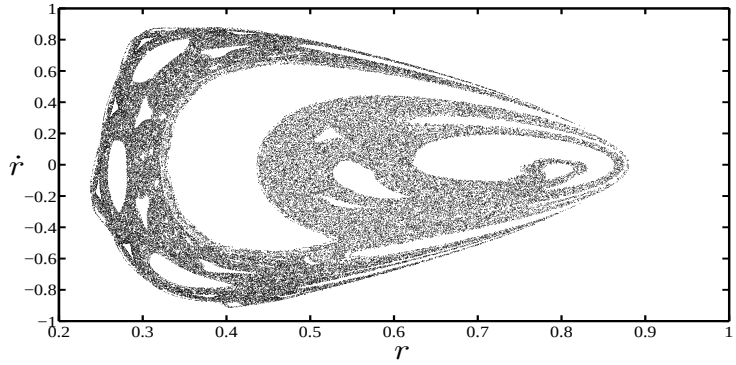

(b)

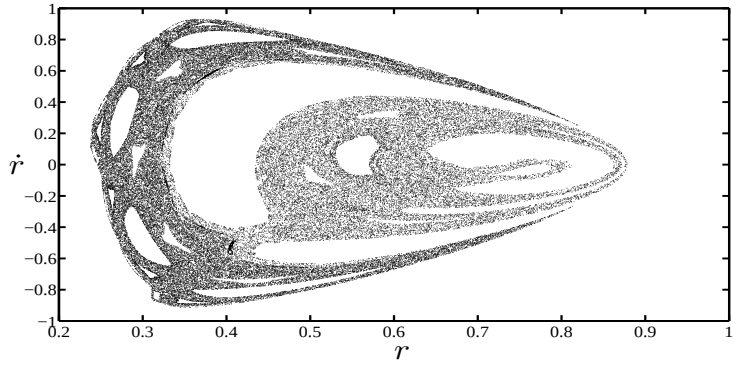

(c)

Figure 4.20: The connected chaotic component for three different Poincaré sections, where an initial condition was iterated forward for 50000 times (a) $\theta_i = 0$ (b) $\theta_i = \pi/8$ (c) $\theta_i = \pi/4$

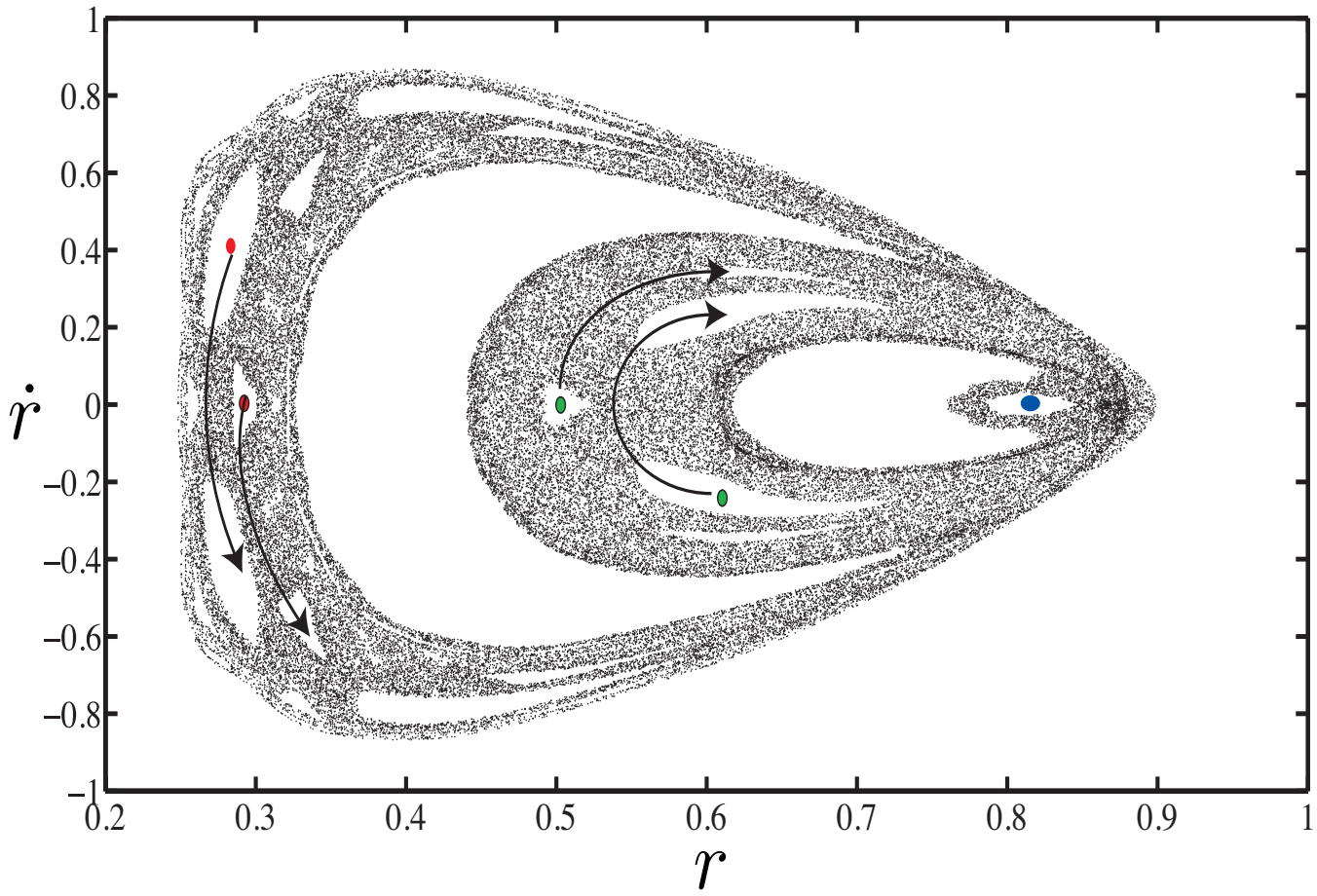

Figure 4.21: Direction of movement of different resonances as stirrers. Two of the resonances that move anti-clockwise are shown with red circles inside them, while the the two with the green circles move clockwise as θ_i is increased from 0. The resonance containing the blue circle acts like the central stirrer for braid analysis.

The above observation implies the saddle (or center) points associated with these resonances act like stirrers, moving in opposite directions. First we consider one resonant island moving in each direction (since the others rotate parallel to one of the two chosen resonant islands, this is is sufficient) . If we pick a period k island moving clockwise, and a period m island moving anti-clockwise, we can look at a higher iterate of the map (where the period will be given by the lowest common multiple of m and k) in which both the islands will come back to the starting position after one iteration of this higher period map. We use the mapping described in [22] for circular motion on a periodic domain, and consider the resonance containing the blue circle in to be the stationary central stirrer. Consider the motion of the saddle points which rotates anti-clockwise around this central stirrer, as shown in 4.22. The braid word for this motion can be written as $\sigma_{-2}\sigma_1\sigma_2\sigma_{-1}\sigma_2\sigma_1$, which is a trivial braid, and hence the TNCT predicts the lower bound to be 0. Thus, we do not get any useful information by doing the topological braid analysis of this flow, by solely looking at periodic points.

Since the braid formed by looking solely at periodic points does not yield any useful information, we use the set-oriented method of finding almost-invariant sets and try to identify other braids that could possibly exist in the PCR3BP problem.

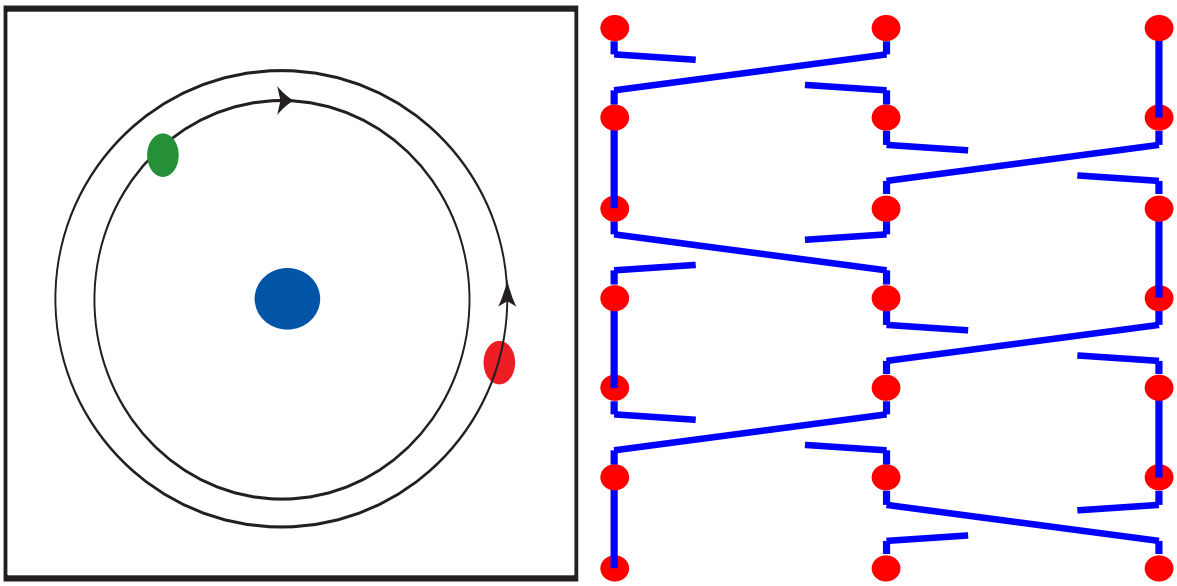

(a) (b)

Figure 4.22: (a) The braiding motion of the two counter-rotating saddle points. (b) The mathematical braid formed by the motion. This braid is topologically trivial and TNCT does not give any lower bound on this braid.

4.6.2 Almost invariant sets in the Poincaré section

Similar to the procedure followed earlier in this chapter for the fluid system, we form a number of time-shifted Perron Frobenius operators, which we denote by M_{θ_i} on section θ_i, since the role of time is now played by the angle θ_i in this problem. The region in the two dimensional section on which we compute this operator is isolated by computing the outer boundary of the connected chaotic sea in the respective Poincaré section. In figure 4.23, the relevant section of the phase space over which the operator is computed is shown in black. We discretize the region $(0.1 < r < 1, -1 < \dot{r} < 1)$ using 16000 equally spaced boxes, and then extract the region of interest (called the recurrent set in literature) consisting of ≈ 7000 boxes.

We plot the various eigenvectors of the reversibilized operator constructed on $\theta_i = 0$ section, i.e., M_0 in figure 4.24. By comparing the eigenvector plots to figure 4.20(a), we see that these eigenvectors capture the various resonant islands, and also the boundary between division between the chaotic sea, and rest of the surface of section features. We extract the almost-invariant structure based on the second eigenvector for four different θ_i values, and plot the m in figure 4.25. While this is helpful in determining the macroscopic transport in the PCR3BP, we do not find any new braiding structure using this approach. The braids formed by components of various almost-invariant sets can be identified easily by just looking at the motion of fixed points (saddles and centers) in the various Poincaré section. We conclude that the almost-invariant set approach is not suited for the purposes on finding the braiding structure for this problem.

Remarks on braiding in PCR3BP

We have presented an attempt to find pseudo-Anosov braids in the PCR3BP by constructing Perron Frobenius operators on a family of two dimensional surface of section. The structure revealed by various almost-invariant sets contructed via the eigenvectors of the operators do

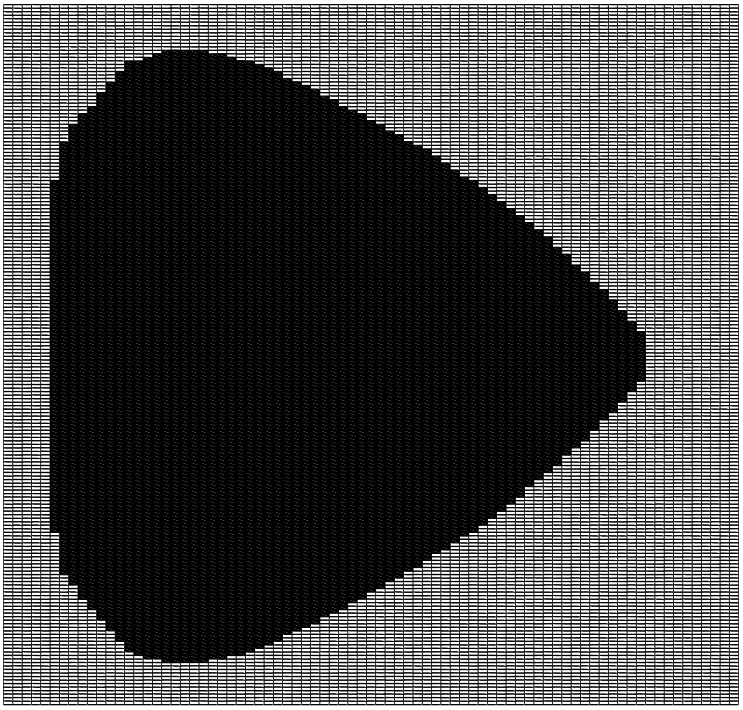

Figure 4.23: The discretization of the two dimensional section in 16000 boxes. The PF operator is computed over the region shown in black, called the recurrent set.

not reveal any new information regarding the presence of any non trivial braids in the phase space. We believe that the method of using a ensemble of random initial conditions and finding random braids, as was mentioned in [54], may be better suited to this problem.

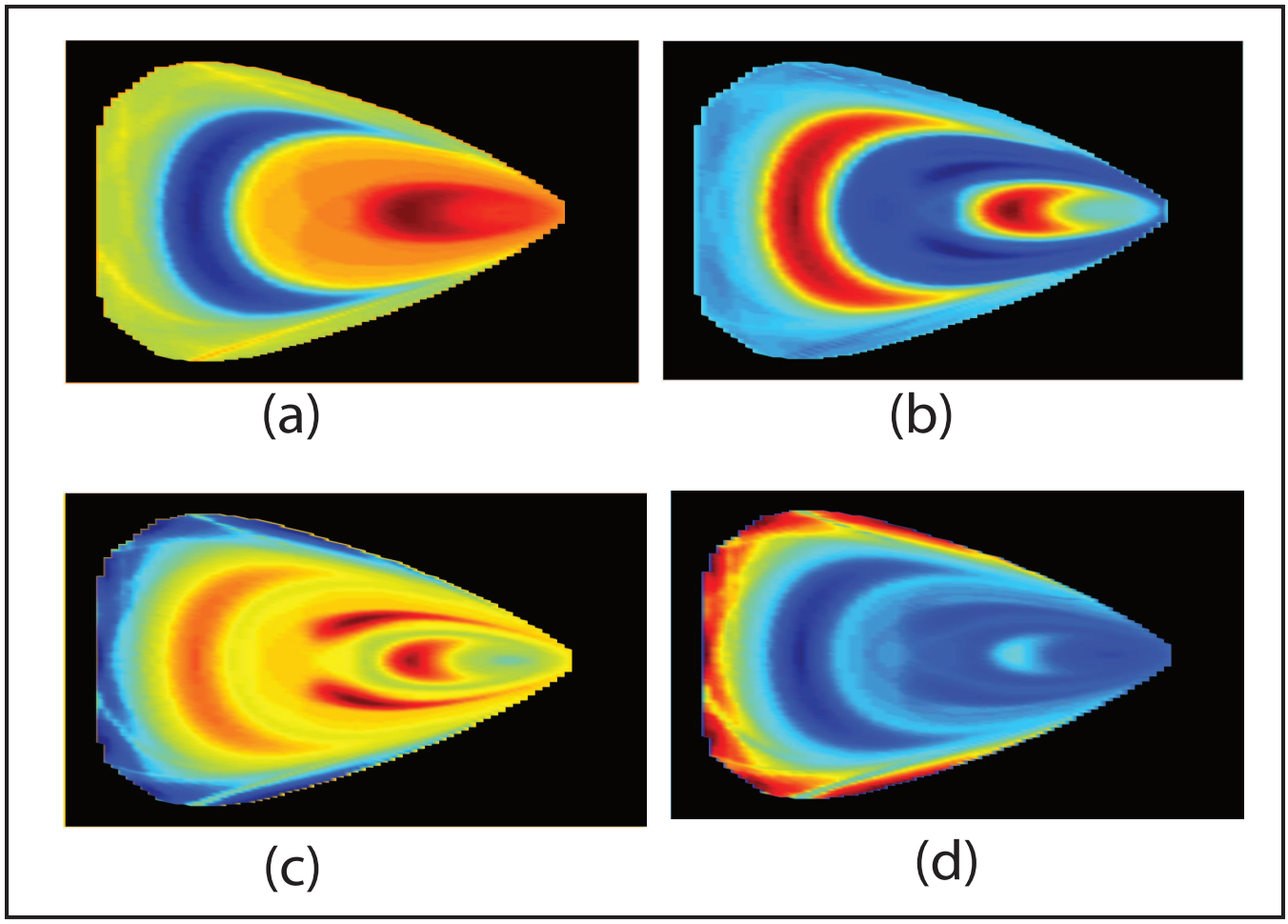

Figure 4.24: Four eigenvectors corresponding to leading eigenvalues (< 1) of the reversibilized PF operator M_0. Compare with 4.20(a) and notice that these eigenvectors capture the various resonant islands.

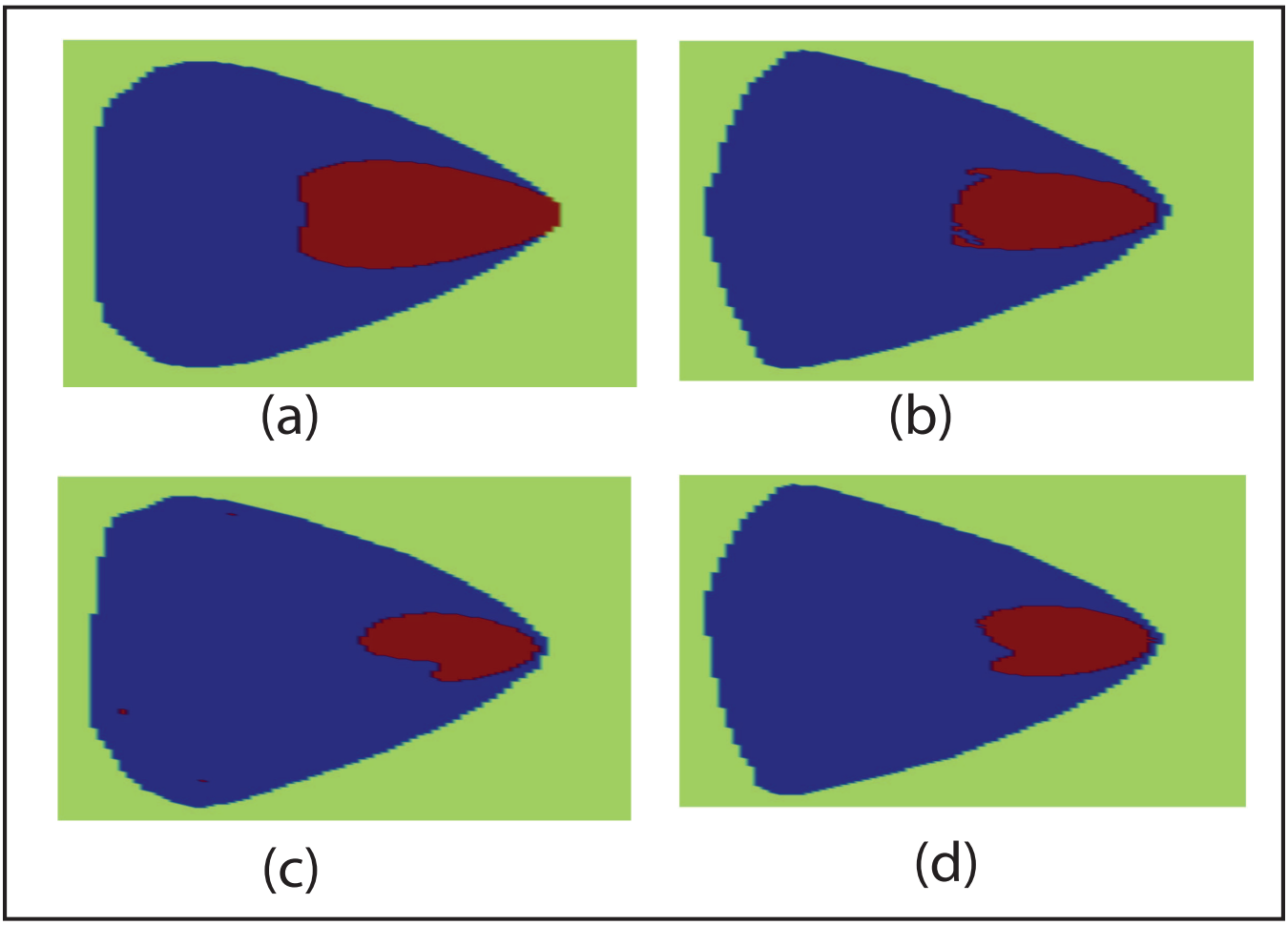

Figure 4.25: Almost invariant set structure extracted using the second eigenvector for (a) M_0 (b) $M_{\pi/2}$ (c) $M_{5\pi/8}$ (d) $M_{7\pi/8}$. The regions shown in green and blue have minimal transport amongst them.

Chapter 5

Conclusion

In this thesis, we have applied geometric and statistical methods to

- Exploit structure in an intelligent way to achieve certain objectives using minimal but effective control (Chapter 3).
- Find structure in a class of complex systems where there is an apparent loss of structure due to perturbation in parameters (Chapter 4).
- Provide numerical evidence of applicability of topological techniques to a class of systems where it hasn't been applied before (Chapter 4).

In chapter 3, our main contribution is the demonstration of the use of a family of controlled Keplerian Maps in the Patched-Three-Body framework to design fuel efficient trajectories with realistic flight times. This approach is a stepping stone towards automating the design process of complicated missions such as multi-moon orbiters. We use analytically derived symplectic maps that approximate the dynamics of PCR3BP and patch solutions in two different PCR3BPs to form a trajectory in the the four-body planet-moon environment of Jupiter-Europa-Ganymede-Spacecraft. We demonstrate that the use of intelligent control

that takes full advantage of structure of the PCR3BP can lead to desirable trajectory characteristics.

In chapter 4, our main contribution is the extension of the Thurston-Nielsen classification theorem based framework to systems that do not have any easily discernible fixed points. We use set-oriented transfer operator methods to find almost-invariant set structure in the phase space of a lid-driven cavity flow system. We numerically demonstrate the validity of the lower bound predicted by Thurston-Nielsen theorem based on braids formed by almost-invariant-sets. We also demonstrate the phenomenon of braid-bifurcation, where the almost-invariant-set structure consisting of 3 sets can be continued to generate almost-invariant sets with topologically different braid structures consisting of 16, 13, 10 and 8 sets, each of which give a good lower bound on the topological entropy of the flow in the regions where they persist. This extension of the Thurston-Nielsen theory based framework to a more general class of systems appears to be a very promising approach for analysis of complex systems encountered in a wide variety of situations.

Bibliography

[1] S. D. Ross and D. J. Scheeres, "Multiple gravity assists, capture, and escape in the restricted three-body problem," *SIAM Journal on Applied Dynamical Systems*, Vol. 6, No. 3, 2007, pp. 576–596.

[2] P. Grover and S. D. Ross, "Designing trajectories in a planet-moon environment using controlled Keplerian Map," *AIAA Journal of Guidance,Control and Dynamics*, Vol. 32(2), 2009, pp. 437–444.

[3] M. Stremler, S. Ross, P. Grover, and P. Kumar, "Almost invariant sets as ghost rods for fluid stirring," 2010. submitted.

[4] S. Wiggins, *Introduction to Applied Nonlinear Dynamical Systems and Chaos*. Springer, 2006.

[5] J. D. Meiss, "Symplectic maps, variational principles, and transport," *Rev. Mod. Phys.*, Vol. 64, 1992, pp. 795–848.

[6] S. Wiggins, *Chaotic Transport in Dynamical Systems*, Vol. 2 of *Interdisciplinary Appl. Math.* Berlin-Heidelberg-New York: Springer, 1992.

[7] A. Lasota and M. Mackey, *Chaos, Fractals and Noise*. New York: Springer-Verlag, 1994.

[8] L. Young, "What are SRB measures, and which dynamical systems have them?," *Journal of Statistical Physics*, Vol. 108, 2002.

[9] M. Dellnitz and O. Junge, "On the Approximation of Complicated Dynamical Behavior," *SIAM Journal on Numerical Analysis*, Vol. 36, 1998, pp. 491–515.

[10] G. F. Michael Dellnitz and O. Junge, "The algorithms behind GAIO – Set oriented numerical methods for dynamical systems," *Ergodic Theory, Analysis, and Efficient Simulation of Dynamical Systems*, Springer, 2001, pp. 145–174.

[11] G. Froyland, "Extracting dynamical behaviour via Markov models," *Nonlinear dynamics and statistics: Proceedings, Newton Institute*, Birkhauser, 1998, pp. 283–324.

[12] P. Bremaud, *Markov Chains: Gibbs Fields, Monte Carlo Simulations and Queues*. Springer, 2008.

[13] W. Huisinga and B. Schmidt, "Metastability and Dominant Eigenvalues of Transfer Operators," *Algorithms for Macromolecular Simulation*, Springer-Verlag, 2002.

[14] G. Froyland and M. Dellnitz, "Detecting and Locating Near-Optimal Almost-Invariant Sets and Cycles," *SIAM Journal on Scientific Computing*, Vol. 24, 2003, pp. 1839–1863.

[15] H. Aref, "Stirring by chaotic advection," *Journal of Fluid Mechanics*, Vol. 143, 1984, pp. 1–21.

[16] S. Newhouse and T. Pignatro, "On the estimation of topological entropy," *Journal of Statistical Physics*, Vol. 72(5-6), 1993, pp. 1331–1351.

[17] P. Boyland, H. Aref, and M. Stremler, "Topological fluid mechanics of stirring," *Journal of Fluid Mechanics*, Vol. 362, 2000, pp. 1019–1036.

[18] W. Magnus, "Braid group: A survey," *Proceedings of the Second Interational Conference on The Theory of Groups, Lecture notes in Mathematics*, Springer-Verlag, 1974, pp. 463–487.

[19] W. Barau, "Uber Zopfgruppen und gkichsinning verdrillte Verkettunger," *Abh. Math. Sem. Hanischen Univ.*, Vol. 11, 1936, pp. 171–178.

[20] M. Bestvina and M. Handel, "Train-tracks for surface homeomorphisms," *Topology*, Vol. 34, No. 1, 1995, pp. 109–140.

[21] T. Hall, *Train: A C++ program for computing train tracks of surface homoemorphism.*

[22] M. Finn, J. Thiffeault, and E. Goulliart, "Topological chaos in spatially periodic mixers," *Physica D*, Vol. 221(1), 2006.

[23] S. D. Ross, W. S. Koon, M. W. Lo, and J. E. Marsden, "Design of a Multi-Moon Orbiter," *13th AAS/AIAA Space Flight Mechanics Meeting*, Ponce, Puerto Rico, February 2003. Paper No. AAS 03-143.

[24] G. J. Whiffen, "An Investigation of a Jupiter Galilean Moon Orbiter Trajectory," *AAS/AIAA Astrodynamics Specialist Conference*, Big Sky, Montana, August 2003. Paper No. AAS 03-544.

[25] S. D. Ross, "The interplanetary transport network," *American Scientist*, Vol. 94, 2006, pp. 230–237.

[26] C. C. Conley, "Low energy transit orbits in the restricted three-body problem," *SIAM J. Appl. Math.*, Vol. 16, 1968, pp. 732–746.

[27] E. A. Belbruno and J. K. Miller, "Sun-perturbed Earth-to-Moon transfers with ballistic capture," *Journal of Guidance, Control and Dynamics*, Vol. 16, 1993, pp. 770–775.

[28] W. S. Koon, M. W. Lo, J. E. Marsden, and S. D. Ross, "Heteroclinic connections between periodic orbits and resonance transitions in celestial mechanics," *Chaos*, Vol. 10, 2000, pp. 427–469.

[29] W. S. Koon, M. W. Lo, J. E. Marsden, and S. D. Ross, "Low energy transfer to the Moon," *Celestial Mechanics and Dynamical Astronomy*, Vol. 81, 2001, pp. 63–73.

[30] E. Belbruno, *Capture Dynamics and Chaotic Motions in Celestial Mechanics: With Applications to the Construction of Low Energy Transfers.* Princeton University Press, 2004.

[31] W. Koon, M. Lo, J. Marsden, and S. Ross, *Dynamical Systems, the Three-Body Problem and Space Mission Design*. Marsden Books, 2008.

[32] D. Brouwer and G. M. Clemence, *Methods of Celestial Mechanics*. New York: Academic Press, 1961.

[33] C. C. Conley, "Twist mappings, linking, analyticity, and periodic solutions which pass close to an unstable periodic solution," *Topological Dynamics* (J. Auslander, ed.), New York, Benjamin, 1968, pp. 129–153.

[34] S. Abdullaev, *Construction of Mappings for Hamiltonian Systems and Their Applications*. Springer, 2006.

[35] M. Dellnitz, O. Junge, W. S. Koon, F. Lekien, M. W. Lo, J. E. Marsden, K. Padberg, R. Preis, S. D. Ross, and B. Thiere, "Transport in dynamical astronomy and multibody problems," *Int. J. Bifurc. Chaos*, Vol. 15, 2005, pp. 699–727.

[36] S. D. Ross and P. Grover, "Fuel-optimal trajectories in a planet-moon environment using multiple gravity assists," *20th International Symposium on Space Flight dynamics*, 2007, pp. NASA/CP–2007–214158.

[37] C. G. T.Shinbrot, E. Ott and J. Yorke, "Using chaos to direct trajectories to targets," *Phys. Rev. Lett.*, Vol. 65, 1990, pp. 3215–3218.

[38] W. S. Koon, M. W. Lo, J. E. Marsden, and S. D. Ross, "Constructing a low energy transfer between Jovian moons," *Contemporary Mathematics*, Vol. 292, 2002, pp. 129–145.

[39] N. J. Strange and J. M. Longuski, "Graphical Method for Gravity-Assist Trajectory Design," *AIAA Journal of Spacecraft and Rockets*, Vol. 39, 2002, pp. 9–16.

[40] A. D. Stroock, S. K. Dertinger, A. Ajdari, I. Mezic, H. A. Stone, and G. M. Whitesides, "Chaotic mixer for microchannels," *Science*, Vol. 295, 2002, pp. 647–651.

[41] M. Stremler, F. Haselton, and H. Aref, "Designing for Chaos: Applications of Chaotic Advection at the Microscale," *Philosophical Transactions: Mathematical, Physical and Engineering Sciences*, Vol. 362, 2004, pp. 1019–1036.

[42] A. Beigie, A. Leonard, and S. Wiggins, "Invariant manifold templates for chaotic advection," *Chaos, Solitons and Fractals*, Vol. 4, 1994, pp. 749–868.

[43] I. Mezic, "Chaotic advection in bounded Navier-Stokes flows," *Journal of Fluid Mechanics*, Vol. 431, 2001, pp. 347–370.

[44] V. Rom-Kedar and A. Poje, "Universal properties of chaotic transport in the presence of diffusion," *Physics of Fluids*, Vol. 11, 1999, pp. 2044–2057.

[45] P. Holmes and J. Marsden, "Melnikov's method and Arnold diffusion for perturbation of integrable Hamiltonian systems," *Journal of Mathematical Physics*, Vol. 23, 1982, pp. 669–675.

[46] W. Thomson, *Mathematical and Physical Papers*. Cambridge University Press, 1910.

[47] J. Thomson, *A treatise on the Motion of Vortex Rings*. Cambridge University Press, 1883.

[48] P. Holmes and J. Marsden, "Topological ideas and fluid mechanics," *Physics Today*, Vol. 49(12), 1996, pp. 28–34.

[49] P. Boyland, M. Stremler, and H. Aref, "Topological fluid mechanics of point vortex motions," *Physica D*, Vol. 175, 2003, pp. 69–95.

[50] T. Gouillart, J. Thiffeault, and M. Finn, "Topological mixing with ghost rods," *Physical Review E*, Vol. 73, 2006, pp. 03611:1–8.

[51] M. Stremler and J. Chen, "Generating topological chaos in lid-driven cavity flow," *Physics of Fluids*, Vol. 19(10), 2007.

[52] J. Chen and M. Stremler, "Topological chaos and mixing in a three-dimensional channel flow," *Physics of Fluids*, Vol. 21, 2009.

[53] J. Chen, *Topological Chaos and Mixing in Lid-Driven Cavities and Rectangular Channels*. PhD thesis, Virginia Polytechnic Institute and State University, 2008.

[54] J. Thiffeault, "Braids of entangled particle trajectories," *Chaos*, Vol. 20(1), 2010.

[55] J. Moussafir, "On the entropy of braids," *Func. Anal. Other. Math*, Vol. 37(1), 2006.

[56] G. Froyland, K. Padberg, M. England, and A. Treguier, "Detecting coherent oceanic structures via transfer operators," *Physical Review Letters*, Vol. 98:224503, 2007.

[57] C. Moore, "Braids in classical dynamics," *Physical Review Letters*, Vol. 70, 1993.

[58] R. Montgomery, "The N-body problem, the braid group, and action-minimizing periodic solutions," *Nonlinearity*, Vol. 11(363), 1998.

[59] G. Arioli, "Periodic Orbits, Symbolic Dynamics And Topological Entropy For The Restricted 3-Body Problem," *Communications in Mathematical Physics*, Vol. 231, 2002.

Appendix

We give braid words for two pulses (i.e., one complete flow period) in each case. Here, σ_R refers to first half of the time period and σ_L refers to second half. The complete braid word for each braid is formed by composing the two words, i.e., $\sigma_L\sigma_R$.

- Braid on 3 strands.

  $\sigma_L = \sigma_{-1}$

  $\sigma_R = \sigma_2$

- Braid on 16 strands.

  $\sigma_L = \sigma_{12}\sigma_{13}\sigma_{12}\sigma_{14}\sigma_{13}\sigma_{12}\sigma_{15}\sigma_{14}\sigma_{13}\sigma_{12}\sigma_{-5}\sigma_{-6}\sigma_{-4}\sigma_{-7}\sigma_{-5}\sigma_{-3}\sigma_{-8}\sigma_{-6}\sigma_{-4}\sigma_{-2}$
  $\sigma_{-9}\sigma_{-7}\sigma_{-5}\sigma_{-3}\sigma_{-1}\sigma_{-8}\sigma_{-6}\sigma_{-4}\sigma_{-2}\sigma_{-7}\sigma_{-5}\sigma_{-3}\sigma_{-6}\sigma_{-4}\sigma_{-5}$

  $\sigma_R = \sigma_{-4}\sigma_{-3}\sigma_{-4}\sigma_{-2}\sigma_{-3}\sigma_{-4}\sigma_{-1}\sigma_{-2}\sigma_{-3}\sigma_{-4}\sigma_{11}\sigma_{10}\sigma_{12}\sigma_9\sigma_{11}\sigma_{13}\sigma_8\sigma_{10}\sigma_{12}\sigma_{14}$
  $\sigma_7\sigma_9\sigma_{11}\sigma_{13}\sigma_{15}\sigma_8\sigma_{10}\sigma_{12}\sigma_{14}\sigma_9\sigma_{11}\sigma_{13}\sigma_{10}\sigma_{12}\sigma_{11}$

- Braid on 13 strands.

  $\sigma_L = \sigma_{10}\sigma_{11}\sigma_{10}\sigma_{12}\sigma_{11}\sigma_{10}\sigma_{-4}\sigma_{-5}\sigma_{-3}\sigma_{-6}\sigma_{-4}\sigma_{-2}\sigma_{-7}\sigma_{-5}\sigma_{-3}\sigma_{-1}\sigma_{-6}\sigma_{-4}\sigma_{-2}\sigma_{-5}\sigma_{-3}\sigma_{-4}$

  $\sigma_R = \sigma_{-3}\sigma_{-2}\sigma_{-3}\sigma_{-1}\sigma_{-2}\sigma_{-3}\sigma_9\sigma_8\sigma_{10}\sigma_7\sigma_9\sigma_{11}\sigma_6\sigma_8\sigma_{10}\sigma_{12}\sigma_7\sigma_9\sigma_{11}\sigma_8\sigma_{10}\sigma_9$

- Braid on 10 strands.

  $\sigma_L = \sigma_{-3}\sigma_{-4}\sigma_{-2}\sigma_{-5}\sigma_{-3}\sigma_{-1}\sigma_{-4}\sigma_{-2}\sigma_{-3}\sigma_{-1}\sigma_{-2}\sigma_{-1}$

  $\sigma_R = \sigma_9\sigma_8\sigma_9\sigma_7\sigma_8\sigma_6\sigma_9\sigma_7\sigma_5\sigma_8\sigma_6\sigma_7$

- Braid on 8 strands.

  $\sigma_L = \sigma_{-1}\sigma_{-3}\sigma_{-4}\sigma_{-2}\sigma_{-3}\sigma_{-1}\sigma_{-2}$

  $\sigma_R = \sigma_6\sigma_7\sigma_5\sigma_6\sigma_4\sigma_5\sigma_7$